

https://dspace.org/

Computational investigation into the properties of potentially ultra hard boride materials

Letsoalo, Thabo Ezekiel

2011-02-25
http://hdl.handle.net/10539/9090

Downloaded from a DSpace repository. https://dspace.org/

Computational Investigation Into The Properties Of Potentially Ultra Hard Boride Materials

Thabo Ezekiel Letsoalo

A thesis submitted to the Faculty of Science,

University of the Witwatersrand,

in fulfillment of the requirement for the degree of

Doctor of Philosophy.

School of Physics,

University of the Witwatersrand,

Johannesburg,

South Africa.

August 25, 2010

Declaration

I declare that this thesis is my own, unaided work. It is being submitted for the degree of Doctor of Philosophy in the University of the Witwatersrand, Johannesburg. It has not been submitted before for any degree or examination in any other University.

_____

Thabo Ezekiel Letsoalo

_____day of_____2010

Abstract

Boron exists in many different structures with an important similarity that they all contain connected boron icosahedron formed from twelve B atoms. Many have the potential to be important hard materials. The icosahedra are arranged in planes and are bonded to each other by three centered bonds within a plane and by two centered bonds to icosahedra in adjacent planes. It is likely that the two center bonds are stronger than any other bonds in the crystals and may contribute significantly to the strength of these materials. Various structures that hold potential for super hard material properties are examined in the present work using *ab-initio* computational techniques. Systematic trends are established. The charge density between B-B bonds in each structure are examined and it is suggested that hardness of the material, in part, relate to the average charge density contained on these bonds. Atoms connecting the B_{12} icosahedra can donate charge that enhance the strength of the B-B bonds.

The structural and thermodynamics properties of boron icosahedral materials are also studied using molecular dynamics (MD)simulation with the use of bond order Tersoff potentials and are compared with *ab-initio* computational results and exper-

iments. Various physical quantities including the elastic constants of boron carbide (B_4C), thermal expansion coefficient, specific heat are predicted at high temperatures. The linear thermal expansion coefficient for the a and c axis are examined. Predicted specific heats for B_4C and boron suboxide (B_6O) structures obey the classical Dulong-Petit result which is obtained at high temperatures for all solids. Moreover, thermodynamic properties obtained in this work are used to estimate Grüneisen parameters for these potentially ultra-hard boride materials.

Finally we examined the elastic constants of an ultra hard boride B_6O and some defects in the crystal structure using the first principle calculations. The single crystal elastic constants calculated were used to estimated polycrystalline properties and thermodynamic properties such as the melting and Debye temperatures as well as sound wave velocities and melting temperatures of B_6O and defect structures. Single crystal elastic constants are found to be comparable with that estimated previously from theoretical calculations and polycrystalline elastic moduli were also calculated and analyzed systematically in comparison with available theoretical and experimental data. We also estimated the formation energies of the various structures using chemical potentials. Analysis of the computed results shows that the formation energies of substitutional defect, nitrogen to oxygen are smaller that those of carbon and vacancies and the low values of nitrogen substitutional defect suggest a possible great solubility of nitrogen in B_6O.

Dedication

I dedicate this thesis to Lehlogonolo, Putla and Matome.

Acknowledgments

Firstly I would like to thank my supervisor Professor J. E. Lowther for his exceptional mentorship and courageous support.

I would also like to thank Jacqueline Dérens for the support she gave me throughout my academic life. I thank mother Tenoi for everything in my life. I appreciate the contribution of my friends and relatives, cousins, uncles and aunts towards my studies. "Ke leboga go menagane banareng".

I would like to acknowledge Martin"Fiki Model" Mmethi, Uzodinma"Igwee" Okeke, Mahlaga "Malome" Molepo, Musa" Bra-Sifiso" Nkambule, Vovo and also all friends at Materials Modelling Center and University of Limpopo Physics Staff (Turfloop Campus).

The support of the DST/NRF Center of Excellence in Strong Materials (CoE-SM) towards this research is hereby acknowledged and University of the Witwatersrand for financial assistance.

Finaly I acknowledge Center for High Performance Computing (CHPC) South Africa for supercomputing facilities used to perform the last part of this work.

Contents

Declaration **i**

Abstract **ii**

Dedication **iv**

Acknowledgments **v**

List of Figures **xv**

List of Tables **xviii**

Publications **xix**

Presentations **xx**

1 Introduction **1**

2 Ultra-Hard Materials **6**

2.1 Hardness 7

3 Boron and Boride Materials **11**

3.1 Crystal Structures of Borides 12

3.1.1 Tetragonal Borides 13

3.1.2 Rhombohedral Borides 15

3.1.3 Orthorhombic-Borides 17

3.2 Experimental Studies 21

3.3 Computer Simulation Studies 22

3.4 Potential Applications of Borides as Hard Materials 24

4 Electronic Structure Methods **27**

4.1 Adiabatic Approximation 28

4.2 Hartree-Fock Approximation 31

4.3 Density Functional Theory 34

4.3.1 Constrained Search Formalism 35

4.3.2 Functionals for Exchange and Correlation 38

4.4 Plane waves and Pseudopotentials 46

4.4.1 Plane Waves Basis Sets 46

4.4.2 Pseudopotentials 49

4.4.3 The PAW method 54

4.5 VASP Code 55

5 *Ab-initio* Computational Results **57**

5.1 Convergence 57
5.1.1 k-points 58
5.2 Equilibrium Properties 60
5.2.1 Computational Procedure 60
5.2.2 Equilibrium Atomic Volume 61
5.2.3 Equation of State and Bulk Modulus 63
5.3 Electronic Properties 68
5.3.1 Density of States 69
5.3.2 Changes at the Boron Icosahedra 74
5.4 B_4N, B_6N and B_6C 86

6 Large Scale Computer Modelling Techniques 90

6.1 Statistical Mechanics 91
6.2 Molecular Dynamics Simulation 94
6.3 Calculation of Physical Properties from MD 99
6.4 Non Equilibrium Molecular Dynamics 102
6.5 Potentials 102
6.6 Introduction to Tersoff Potentials 105
6.7 Potentials used in this work 107

7 Structural and Thermodynamic Properties of Simulations 109

7.1 Simulation Details 109

7.2 Zero Temperature Properties 110
7.3 Thermodynamic Properties of Borides 115
7.3.1 Specific heat and thermal expansions 125

8 Elastic Properties and Some Defects in Ultra Hard Boron Suboxide (B_6O) 137

8.1 Calculation of Elastic Properties 138
8.2 Defect Structures 147
8.3 Computational Procedure 148
8.4 Results and discussion 150
8.4.1 Structural properties 150
8.4.2 Single crystal elastic parameters 154
8.4.3 Polycrystalline elastic moduli 157
8.4.4 Formation energies of point defects 161
8.5 Summary 167

9 Conclusion 169

List of Figures

2.1 Scattering of Vickers hardness for common set of hard materials when compared with bulk modulus (grey region) and shear (blue region). . 10

3.1 Boron icosahedron. 13

3.2 Connectivity of B_{12} icosahedra in tetragonal B_{50}. 14

3.3 Crystal structure of $\alpha-$boron. 15

3.4 Connectivity of B_{12} icosahedra in B_4C polar 16

3.5 Connectivity of B_{12} icosahedra in B_4C chain structure 17

3.6 Crystal structure of B_6O 18

3.7 Crystal structure of $MgAlB_{14}$. Mg atoms are large spheres(white) and Al (teal). 19

3.8 Crystal structure of MgC_2B_{14}. Large spheres are Mg. 19

4.1 Supercell geometry for an isolated molecule (icosahedron). The dashed lines encloses the periodic supercell. 50

4.2 Schematic illustration of all-electron (solid lines) and pseudoelectron (dashed lines) potentials and their corresponding wavefunctions. . . . 52

5.1 Total energy versus number of k-points for $MgAlB_{14}$ 59

5.2 Total energy versus number of k-point for $NaAlB_{14}$ 60

5.3 Trends in volume 61

5.4 Trends in bulk modulus 66

5.5 Energy vs volume for B_{50}, B_4C and B_6O 67

5.6 Energy vs volume of orthorhombic $NaAlB_{14}$ and $MgAlB_{14}$ 67

5.7 Visualization of k-space showing values of k as points. The number of allowed states is of these points contained in the shell of radius k and thickness dk. 70

5.8 The free elecron density of states ($\rho(E)\ \alpha\ E^{\frac{1}{2}}$) 71

5.9 Density of states for tetragonal boron B_{50} 72

5.10 Density of states for B_4C (polar). 72

5.11 Density of states for B_4C (chain). 73

5.12 Density of states for B_6O 74

5.13 Density of states for $MgAlB_{14}$ 75

5.14 Density of states for $NaAlB_{14}$ 75

5.15 Calculated charge density of tetragonal boron. (a) Density at the isosurface value of 200 and (b) the density slice offset of 0.44. 76

5.16 The charge density of $MgAlB_{14}$.Density (left) is at the iso surface value of 200 and the slice offset(right) of 0.44. Mg atoms are red while Al atoms are green. 77

5.17 Charge density of B_4C polar. The density at iso surface value 200 (left) and the corresponding slice (right) at azimuthal angle of 342, polar angle of 97.2 and offset of 0. 79

5.18 Charge density of B_4C chain. 80

5.19 Charge density of B_6O 81

5.20 Charge density contour plot in super-hard B_6O. Bonding of O to the B icosahedra is visible as is the B-B bond between the B icosahedra. There is no covalent bonding between the O atoms. 81

5.21 Distribution of B-B bond lengths in (a) tetragonal boron, (b) $MgAlB_{14}$, (c) MgC_2B_{14},(d) B_4C and B_6O. The smaller bonds lengths are usually associated with intericasahehral bonding 82

5.22 Charge density (LDA, top: GGA, bottom) across B-B bonds in (a) tetragonal boron, (b) $MgAlB_{14}$, (c) MgC_2B_{14}, (d) B_4C and (e) B_6O . 84

5.23 Trend in B-B average bond charge. 85

5.24 Energy vs volume of B_4N, B_6N and B_6C 87

5.25 Bulk modulus vs c/a ratio 88

6.1 Schematic representation of radial distribution function. 101

7.1 V/V_0 vs pressure for B_{12}, B_{50} and B_4C polar. 113

7.2 V/V_0 vs pressure for B_4C chain and B_6O. 114

7.3 Bulk Modulus vs system size 115

7.4 RDFs pairs of B-B in B_{12}. 116

7.5 RDF pairs of B-B in B_{50}. 117

7.6 RDF pairs B-B, B-C and C-C in B_4C polar. 117

7.7 RDF pairs B-B, B-C and C-C in B_4C chain. 118

7.8 RDF pairs B-B, B-O and O-O in B_6O. 118

7.9 Bulk crystal of $\alpha-B_{12}$ at 300K. 119

7.10 Bulk crystal of $\alpha-B_{12}$ at 3000K. 120

7.11 Bulk crystal of B_4C chain at 300K. 120

7.12 Bulk crystal of B_4C chain at 3000K. 121

7.13 Bulk crystal of B_6O at 300K. 121

7.14 Bulk crystal of B_6O at 3000K. 122

7.15 RDFs of Boron at 3000K 122

7.16 RDF pairs B-B, B-C and C-C in B_4C polar. 123

7.17 RDF pairs for B_4C chain at 3000K. 123

7.18 RDF pairs for B_6O at 3000K. 124

7.19 Variation of pressure against temperature for the borides. 125

7.20 Variation between diffusion coefficient and temperature of boron atoms in icosahedral systems. 126

7.21 Energy as a function of temperature for B_{12}. 127

7.22 E vs T in B_{50}. 127

7.23 E vs T in B_4C polar. 128

7.24 E vs T in B_4C chain. 128

7.25 E vs T in B_6O. 129

7.26 Lattice variation along a axis in B_{12}. 131

7.27 Lattice variation along c axis in B_{12}. 131

7.28 Lattice variation along a axis in B_{50}. 132

7.29 Lattice variation along c axis in B_{50}. 132

7.30 Lattice variation along a axis in B_4C polar. 133

7.31 Lattice variation along c axis in B_4C polar. 133

7.32 Lattice variation along a axis in B_4C chain. 134

7.33 Lattice variation along c axis in B_4C chain. 134

7.34 Lattice variation along a axis in B_6O. 135

7.35 Lattice variation along c axis in B_6O. 135

8.1 Crystal structure of B_6O and point defects created. 149

8.2 Transverse sound wave velocity vs $K\rho^{-1}$. 161

8.3 Longitudinal sound wave velocity vs $K\rho^{-1}$. 162

8.4 Formation energies of vacancies and substitutional carbon and nitrogen 166

9.1 Crystal structure of B_6O with one vacancy at O site 190

9.2 Crystal structure of B_6O with two vacancies at O sites. 191

9.3 Crystal structure of B_6O with one N substituting O atom. 191

9.4 Crystal structure of B_6O with substitutional defect of 2 N at 2 O sites. 192

List of Tables

2.1 Summary of mechanical properties of ultra-hard solids. 7

3.1 Physicomechanical poperties of B_6O, B_4C and B_4Si 22

5.1 The number of k-points and total energy of LDA convergence test . . 58

5.2 Structural properties of various Boron related compounds together with available experimental and theoretical calculations. Calculated GGA values in brackets 62

5.3 Bulk Moduli B, pressure derivatives B' of various Boron compounds and some experimental and theoretical values. GGA values in brackets. 66

5.4 Number of B-B bonds and average bond length(Å) and charges . . . 83

5.5 No atoms and calculated lattice parameters 87

5.6 Equilibrium properties. Calculated GGA values in brackets 88

6.1 Tersoff potential parameters used in this study. Parameters for B, C and O were taken from Matsunaga and Munetoh. 108

7.1 Calculated elastic properties in (GPa) using GULP. Other calculation and experimental values are listed. 111

7.2 Number of atoms in the supercell and lattice parameters of various Boron related compounds together with available experimental and theoretical calculations. Calculated GGA values in brackets. 112

7.3 Bulk Moduli B, pressure derivatives B' of various Boron compounds and some experimental values. 114

7.4 Thermodynamic properties of boron, boron carbide and boron suboxide. 130

8.1 Independent cij in the crystal structures. 141

8.2 Theoretically determined lattice parameter of B_6O and the ratio c/a with some experimental values. Equilibrium volume, Bulk modulus and pressure derivative are presented with experimental results using equation of state. 151

8.3 Number of atoms in the unit cell, equilibrium atomic volume and lattice parameters of various Boron suboxide defects together with total energies. Bulk of the moduli and pressure derivatives were calculated using EOS 152

8.4 Single crystal elastic constants of B_6O, B_6N, B_6C and some defects at zero pressure c_{ij} are in GPa. T_m is estimated melting temperature. . 154

8.5 Elastic anisotropy factors and Poisson ratio of B_6O and some defects B_6O. 156

8.6 Elastic properties of B_6O and some defects. Hill's average bulk Modulus(B), shear modulus(G), Young modulus(K) and Poisson ratio are derived from single crystal elastic constants. 157

8.7 Percentage anisotropy of bulk (A_B), shear (A_G) . The longitudinal, transverse , mean sound velocity (v_L, v_T, v_M) and Debye temperature (Θ_D) are also presented. 160

8.8 Total energies and chemical potentials calculated using B_{12}. 164

8.9 Formation energies from chemical potentials. 165

Publications

T. E. Letsoalo and J. E. Lowther "Systematic Trends in Boron Icosahedral Structured Materials" Physica B 403 (2008) 2760-2767

T. E. Letsoalo and J. E. Lowther "Computational Investigation into Elastic Properties of bulk and defective Ultra Hard B_6O" to be Published in Journal of Superhard Materials (2010)

T. E. Letsoalo and J. E. Lowther "Elastic and Thermodynamic Properties of Potentially Super Hard Boride Carbon Materials" Submitted to Elsevier (2010)

Presentations

T. E. Letsoalo and J. E. Lowther "Systematic Trends in Icosahedral Structured Materials" CCP5 Summer School, July 2008, University of Sheffield, UK(Poster)

T. E. Letsoalo and J. E. Lowther "Computational Investigation Into The Properties of Potentially Ultra Hard Boride Materials" DST/NRF Center of Excellence in Strong Materials Workshop, April 2008, University of the Witwatersrand, Johannesburg(Poster)

T. E. Letsoalo and J. E. Lowther "Computational Investigation Into The Properties of Potentially Ultra Hard Boride Materials" South African Institute of Physics 52nd Annual Conference, July 2007, University of the Witwatersrand, Johannesburg(Oral)

T. E. Letsoalo and J. E. Lowther "Computational Investigation Into The Properties of Potentially Ultra Hard Boride Materials" DST/NRF Center of Excellence in Strong Materials Workshop, April 2007, University of the Witwatersrand, Johannesburg(Oral)

Chapter 1

Introduction

Ultra-hard materials are widely used as tools for industrial applications such as cutting; grinding, chopping, drilling and milling, as well as sawing and wear parts. Materials of this nature come in different forms such as ceramics, hard metals, strong alloys. They have a high hardness, they resist corrosion, and they have high stiffness, high mechanical strength and most are radiation resistant. Most researchers define"ultra-hard" materials as those empirically probably having hardness greater than 4000 Kg.mm^{-2} on the Knoop scale and Vickers hardness or about 10 on Mohs hardness scale [1]-[4]. Diamond is the naturally occurring hardest material known to mankind with a Vickers hardness ranging between 70 and 100 GPa, followed by expensive cubic boron nitride (cBN). cBN is not found naturally and therefore requires harsh conditions to be synthesized and this material has a single crystal hardness between 45-50 GPa on Vickers hardness. Synthetic materials such as polycrystalline

diamond (pcD) and polycrystalline cubic boron nitride (pcBN) are also produced at economical cost with varying properties in engineering and manufacturing industries as drill and cutting inserts [4].

New ultra-hard materials with comparable or even superior properties to diamond are continuously being predicted [5]and potentially new ultra-materials are presently being designed and examined fundamentally not only for scientific interest, but also for commercial usage. Different techniques both theoretically and experimentally are employed in attempt to replace expensive diamond for applications where abrasive wear resistance is of great importance. Understanding the fundamental properties of existing ultra-hard materials or what makes them special is of utmost importance in rediscovering and synthesizing the new ones. Diamond has a bulk modulus of 440 GPa whereas cBN a bulk modulus of 360 GPa [6]. A number of researchers [7] have focused upon the bulk modulus in their search for new superhard materials because hardness often correlates well with bulk modulus for groups IV [1], III–V [8], and II–VI [9] materials.

The strongest materials always contain boron, carbon, nitrogen or oxygen [10]; and frequently only these lightweight elements are found in super-hard structures or compounds [11]. Looking at the periodic table these are the first elements in the second period. In their atomic structure there are no inner p-electrons in the core to push the valence electrons outward from these elements; then the absence of p-orbital in the electron core and small atomic volumes results in high bonding strength. For

example, diamond is the hardest because of localized electrons in covalent bonding. Synthetic cBN, boron carbide (B_4C) and boron suboxides (B_6O) are the hardest materials after diamond. There is also an intense investigations in hard materials beyond B-C-N-O system consisting of metals including transition-metals from borides to oxides [12][13].

Recently work has focused on alloying of diamond with cBN to identify superhard materials with B-C-N structure [14][15]. It is hoped that the synthesis of dense ternary B-C-N compounds could exhibit novel properties between diamond and cBN, and the dense phases may be considered as potential ultra-hard materials. Dense B-C-N phases are expected to be harder that cBN, but still retaining thermal and chemical stability of cBN and this would be an excellent material for high speed cutting and polishing of ferrous alloys where diamond fails [16].

Boron based materials have offered many potential applications [17]. Many boron based structures are the boron icosahedron [18]-[21]formed from twelve B atoms. Lightweight atoms C, N, and O are found in such materials with the C, N, or O connecting the B icosahedra [22]and recently other elements like Mg and Al have also been used and found to be very important [23]-[26]. Some of these materials have advantages over diamond and cBN in that they are easier to synthesize [27] and therefore offer great excitement in new applications.

The search for new ultra-hard materials has been aided by much theoretical and computational effort [28]. The theoretical predictions and appropriate synthesis have

now demonstrated the potential of new ultra-hard materials. Computational procedures have advanced to a degree of reliability where predictions of a variety of properties of materials can now be studied with great confidence [29]. In the present work we investigate properties of different phases of the borides using computational modelling techniques.

An *ab-initio* pseudopotential approach and molecular dynamic simulation have been employed to study the properties of potentially ultra-hard boride materials. Computer simulation gives information at a microscopic atomic level [30][31]from which experimental properties are derived or predicted. *Ab-initio* approaches can now quite accurately predict many properties but have computational limitations with relatively low numbers of atoms. The emphasis is to examine trends occurring over the series, how the boron icosahedra are held together and to investigate changes at the boron icosahedra.

For *ab-initio* pseudopotential calculations we employed Density Functional Theory (DFT) to study the electronic structural properties of the solids in their ground state. In the theoretical analysis we used two forms of DFT, namely local density approximations (LDA) and a generalized gradient approximation(GGA), as a way of treating the electron and correlation. A more detailed description of this particular method is given in Chapter 3. For large numbers of atoms in simulations, we used the Tersoff bond-order potentials to examine structural and thermodynamic properties of some borides.

The thesis is arranged as follows. In Chapter 2, we review some properties of ultra-hard materials. Chapter 3 is a literature review of boron and boron rich solids and their potential application. In Chapter 4, we give a theoretical background technique used, in particular DFT approaches including LDA and GGA functional. The *ab-initio* results are presented and discussed in Chapter 5. In Chapter 6, we outline the computational modelling techniques used specifically for simulations of large numbers of atoms and the results of structural and thermodynamic predictions are presented in Chapter 7. Chapter 8 we studied the defects in ultra-hard boride, (B_6O). Chapter 9 is the summary of all results by making some conclusions.

Chapter 2

Ultra-Hard Materials

Generally ultra-hard materials are considered to be solids with high hardness [4]. They are usually hard ceramics materials that are crystalline in nature and their common chemical bonds are covalent with brittleness in character. Depending on the hardness test method, the most frequently used scratch method for unknown samples hardness is the Mohs scale [32]. The surface sample or mineral which can scratch the surface of diamond or cubic boron nitride (cBN) may be then considered to be an ultra-hard material. Whilst hardness is difficult to precisely quantify, all materials can be conveniently grouped into various hierarchies with ultra-soft, soft, normal, hard, and ultra-hard materials as those on Knoop hardness scale [33] are less than 32, equal or greater than 32-256, 256-1024,1024-4000 and above 4000 Kg.mm^{-2} (in the SI units of GPa) respectively [1]. Materials with such high hardness or satisfying the above definitions are found as single phase like diamond and cBN. Boron rich

Table 2.1: Summary of mechanical properties of ultra-hard solids.

Materials	Formula	[a]Mohs	[a]Knoop (GPa)	[a]Vickers (GPa)	[b]Fracture toughness(MPa.m$^{1/2}$)
Diamond	C	10	75-100	115	5.3
heterodiamond	BC_2N			76	4.5
Boron carbon phase	BC_3			71	9.5
cubic boron nitride	cBN	9	45	62	6.8
Boron suboxide	B_6O	9	30-59	[c](45)	[d](4.5)
Boron carbide	B_4C	9	30	38	3.5

[a]Ref [2],
[b] Ref [34]
[c]Ref [35]
[d] Ref [36]

solids such as boron carbide (B_4C) and boron suboxide (B_6O) crystals also occupy definite place in this realm. Table 2.1 lists some properties of ultra-hard materials.

The search for new compounds or solids in these hardness ranges of ultra-hard structures are expected to be found in the quaternary B-C-N-O system and combination of these elements with some other metals or transition-metals may also produce ultra-hard compounds [10].

2.1 Hardness

By definition, the hardness of a material is the resistance to plastic deformation usually by indentation and it also involves the irreversible motion of atoms in the crystal with respect to each other, often by creation and movements of dislocation. It may be written as [37]:

$$H = H_{int} + H_{ext} \tag{2.1}$$

where H_{int} and H_{ext} are intrinsic and extrinsic contributions to the hardness respectively. The measurements of this concept can be defined as macro-, micro- or nano-scale depending on the test method and the load applied with respect to the value obtained by such measurement. Macrohardness, microhardness and nanohardness are loosely defined for loads of larger than 1 kg, less than 200 g and less than 1 g respectively. Macro-hardness method is simple and is used to obtain mechanical property data for the bulk material from a small sample. Vickers hardness tests are frequently used to determine the micro-hardness of materials, usually by forcing an indenter. In nano-indentation measurements, the depth of the indentation, progressive levels of forcing are measured. The difference between indentation methods which have been developed is in the geometry and the definition of the contact area for a specific indenter. The common methods used in today's technology to determine hardness of a material can be done by scratching, indentation, erosion and rebounds methods [38]. Most frequent hardness tests are measured on Rockwell, Brinell, Vickers, Knoop, Shore, Mohs and Barcol hardness tests. The Rockwell hardness tests is based on the net increase in depth of the impression as load is applied and is more commonly used in industry because the hardness is read directly off machine. The Brinell hardness is determined by indenting a material with a hard steel or carbide sphere of a specified diameter under a specified load into the surface of a material.

Such measurement is determined from the radius of the indent left behind. The Vickers hardness (H_v) and Knoop hardness (H_k) both use diamond pyramid indenters. The difference between them is in the shape of the indenter. They are also derived from the load P as [38][33]:

$$\begin{aligned} H_v &= \frac{1854P}{d^2}, \\ H_k &= \frac{14229P}{l^2} \end{aligned} \tag{2.2}$$

where d is the diagonal of the square-based of the Vickers indenter and l is the long diagonal of the rhombus-based Knoop indenter. They can also be expressed in terms of Mohs hardness M, as [39]:

$$H_v = 3.2M^3 \tag{2.3}$$

Theoretically, the determination hardness of a material for ideal systems may be estimated through its bulk modulus or shear modulus [40]. Although shear modulus is more pertinent to hardness than bulk modulus, bulk modulus is often used as the guide in search for new ultra-hard materials. Bulk modulus is the simple measure of elastic stiffness and it measures the resistance of a solid to volume change, while shear modulus measures the resistance to shape and therefore it is complex to measure because it depends on both the plane and the direction of shear. Figure 2.1 shows the

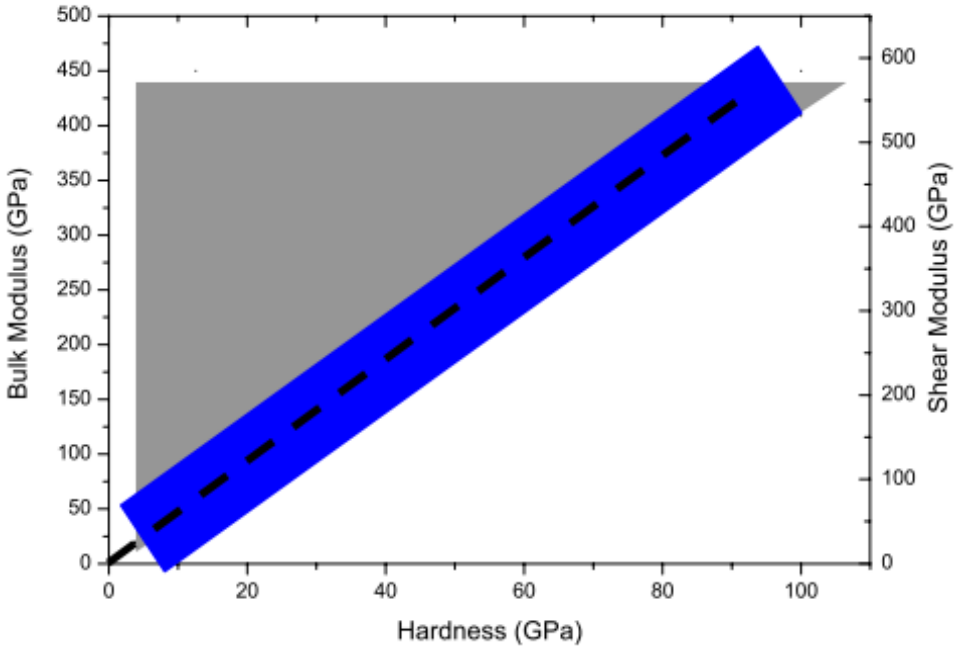


Figure 2.1: Scattering of Vickers hardness for common set of hard materials when compared with bulk modulus (grey region) and shear (blue region).

correlation between bulk and shear modulus and H_v of materials measured by Teter [41]. For the highest hardness, both elastic bulk modulus and the shear modulus must be as large as possible, $B > 250$ GPa and $G > 500$ GPa.

Chapter 3

Boron and Boride Materials

Borides are binary compounds of boron with a more electropositive element or radical. The preferred boride types are: Me_2B, MeB, MeB_4, MeB_6, MeB_{12} (where Me is a metal) and more than 200 compounds have been identified [42]. They are high temperatures compounds produced by reaction mixtures of metals with boron and bonding schemes vary depending on the composition ratio of metal/boron. The more electropositive metal, including the alkali and alkaline earth metals, transition group III, lanthanides and actinides, tend to form borides with higher boron contents, while the remaining, less electropositive metals tend to form borides with high metal content. The higher metal borides that have more than six boron atoms per metal atom, have rigid structures based on icosahedra [42][43]. Metal atoms are embedded in the centers of the cubes with B-B distances around 1.7 Å and because boron is rigid, the lattice constants of the borides are approximately equal regardless of the metal

diameter [44]. At the same time very lightweight materials are formed from boron with structures B_4C and B_6O being especially important and they also have good mechanical properties. These borides have fundamental building blocks based upon boron icosahedra with the C or O connecting the boron icosahedra [45].

Borides have much in common with the metals. Many metal borides are used as components of ceramic metals compositions [46]. These compounds also have small coefficients of expansion.

Boron and boron rich solids also exhibit a close relationship in view of their crystal structures. They are characterized by B_{12} icosahedra, which are common structural elements arranged differently in the various structures. These solids have similar properties such as high electrical conductivity, high melting points, low density, high resistance to chemical attack, hence low corrosives and extreme hardness [27] and find an extensive use in many applications.

3.1 Crystal Structures of Borides

There are many crystal structures of borides. Overall crystal structures based on the B_{12} icosahedron compounds have now been classified into structure types of rhombohedral boron (such as $B_{13}C_2$), β-rhombohedral boron (MeB_x, x>23), α-tetragonal boron ($B_{48}B_2C_2$), β-tetragonal boron (β-AlB_{12}), AlB_{10} or AlC_4B_{24}, YB_{66}, NaB_{15} or $MgAlB_{14}$, and γ-AlB_{12}. The basic unit in all these structures is an icosahedron with the 12 boron atoms at the vertices of regular icosahedron as shown in Figure 3.1.

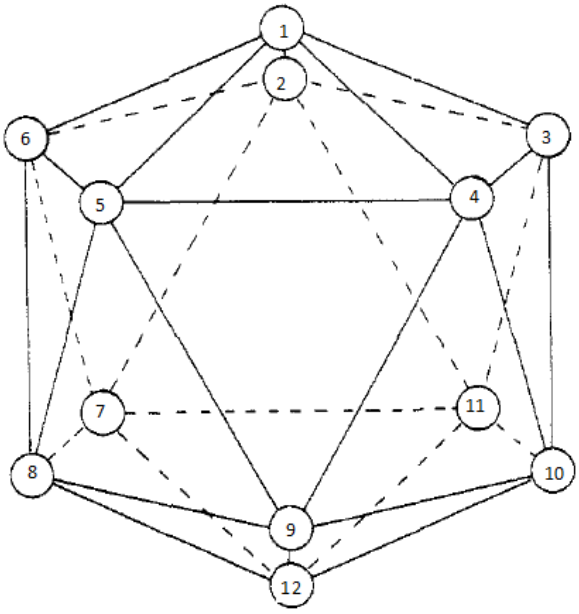


Figure 3.1: Boron icosahedron.

The icosahedra are often arranged in planes in the borides and are bonded to each other by three-centered bonds within the plane and by two centered bonds to icosahedra in adjacent planes. It is likely that the two center bonds between the icosahedra are stronger than other bonds in the material and may contribute significantly to the strength in these materials. In this work the focus has been on tetragonal, rhombohedral and orthorhombic structure types of boride materials.

3.1.1 Tetragonal Borides

There are few boron crystals synthesized to date with tetragonal symmetry since the discovery of boron in 1808 by Guy-Lussac and Day. The tetragonal form [47] of boron

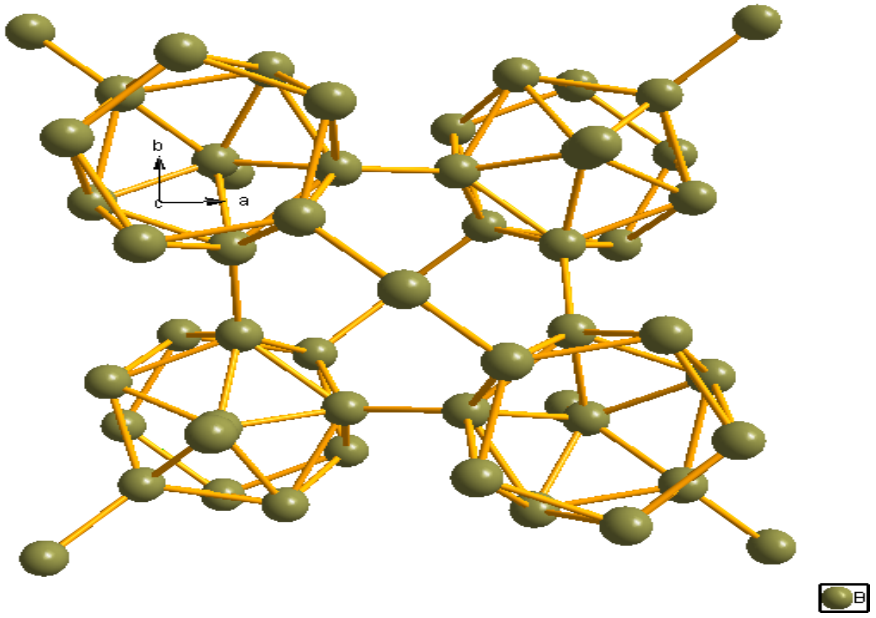


Figure 3.2: Connectivity of B_{12} icosahedra in tetragonal B_{50}.

B_{50} was proposed as pure boron but subsequently discredited [48]. In $B_{50} = (B_{12})_4B_2$ structure there are four B_{12} icosahedra centered at $(\frac{1}{4}, \frac{1}{4}, \frac{1}{4})$, $(\frac{3}{4}, \frac{3}{4}, \frac{1}{4})$, $(\frac{1}{4}, \frac{3}{4}, \frac{3}{4})$, $(\frac{3}{4}, \frac{1}{4}, \frac{3}{4})$ and two boron atoms occupy the positions (0,0,0), $(\frac{1}{2}, \frac{1}{2}, \frac{1}{2})$ with space group $P4_2/nnm$ resulting in 50 atoms in a unit cell. Recently single crystals of $Mg_2B_{24}C$ have also been synthesized [49] with a tetragonal structure closely related to that of B_{50}. The crystal structure of tetragonal B_{50} structure is shown in Figure 3.2 and B_{12} icosahedra are arranged in a near tetrahedral coordination-reminiscent of the coordination in diamond. It has been speculated that tetragonal borides could also have superhard properties [50].

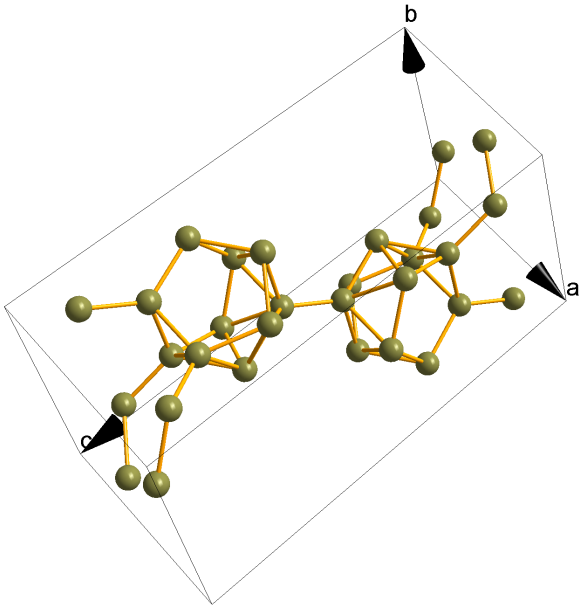


Figure 3.3: Crystal structure of $\alpha-$boron.

3.1.2 Rhombohedral Borides

Alpha boron shown in Figure 3.3 has a simple crystal structure of all polymorphs. Its structure is rhombohedral Bravais lattice with the cell parameter a $\approx$ 5Å and the space group $R\bar{3}m$. The B_{12} units are centred at the vertices of the rhombohedral cell and the angle is approximately 60°. The boron atoms are bonded to adjacent icosahedra with bonds which can be regarded as weak bonds.

Rhombohedral borides also form useful refractory materials as is well established by the properties of boron carbide (B_4C) and related materials. B_4C consists of icosahedral B_{12} building blocks with additional chains of three atoms inserted between the B_{12} units as shown in Figure 3.4 and Figure 3.5 . As with other borides this

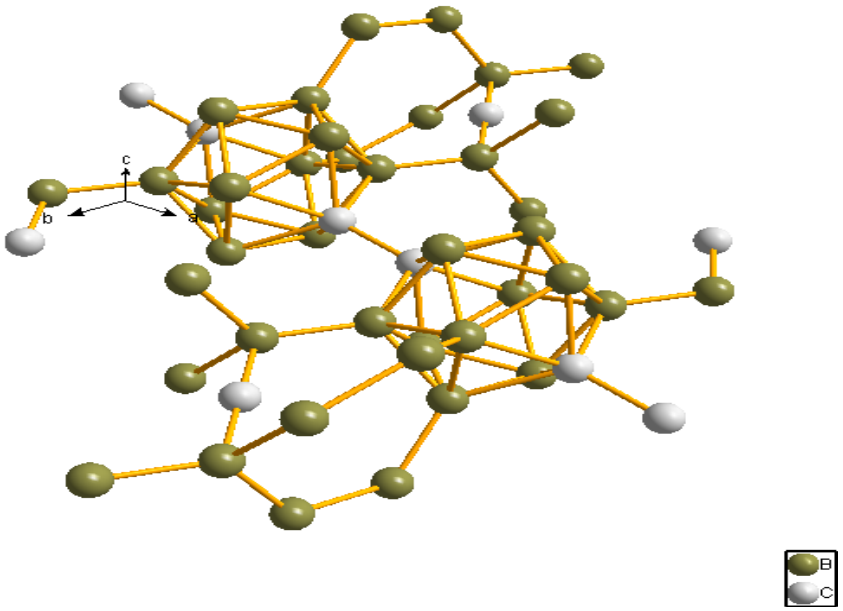


Figure 3.4: Connectivity of B_{12} icosahedra in B_4C polar

material also has possible different bonding structures. In B_4C, a three atoms of carbon (C) chains has been a tentative point in the structure determination of this material with recent suggestions that the B atoms enters the icosahedra producing the so called polar structure [51]. However more recently it has been shown that the polar structure is more likely associated with a $B_{13}C_2$ stoichiometry [52] than the chain structure with B_4C [53]. Two possible crystal structures are shown in Figure 3.4 and Figure 3.5.

Another important rhombohedral hard boride is B_6O [25] with space group $R\bar{3}m$, the same space group of B_4C. Two oxygen atoms connect the boron icosahedra along the [111] direction. The study of the properties of this interesting material have been

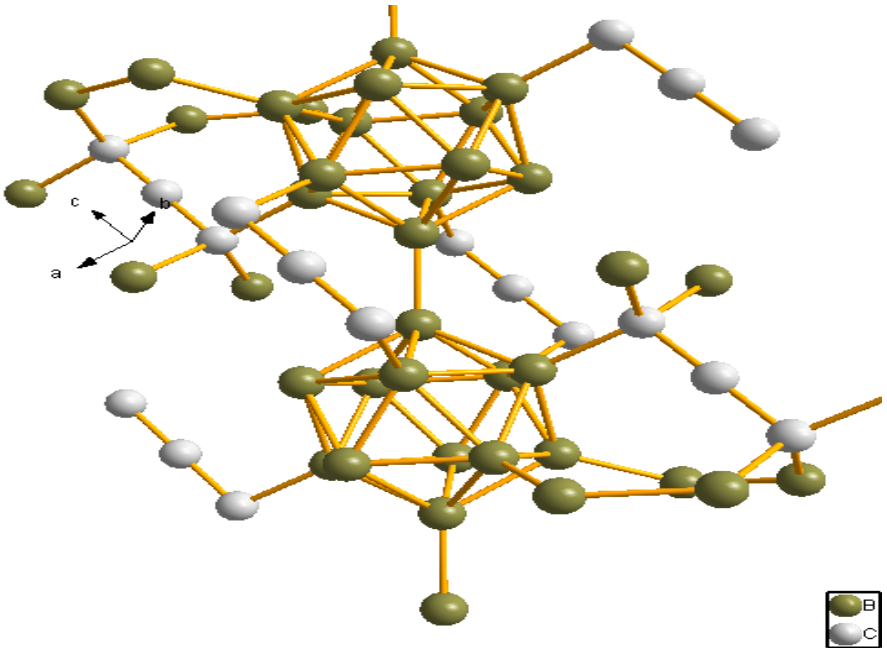


Figure 3.5: Connectivity of B_{12} icosahedra in B_4C chain structure

impeded by the fact that pure and large crystals are difficult to grow. The crystal structure of B_6O is shown in Figure 3.6.

3.1.3 Orthorhombic-Borides

The orthorhombic series of borides also exhibit some of the essential characteristic properties of boron rich borides with an icosahedral basic structure [54]. The general structural formula of the orthorhombic borides is $(B_{12})_4Me(1)_4Me(2)_4(B)_8$ and as with rhombohedral structural borides there are B_{12} icosahedra in the structure. The orthorhombic structures are quite complex; low symmetry and with a very large number of atoms per unit cell. Some of these materials are hard [24] and as with other

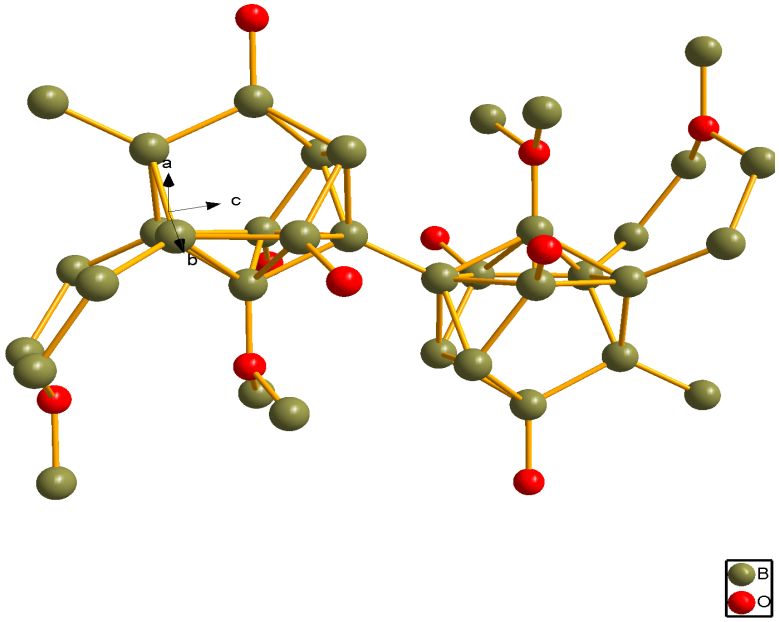


Figure 3.6: Crystal structure of B_6O

hard boride materials adding additional elements or compounds to these structures typically influences their hardness.

$MgAlB_{14}$ has been a very important boride that has been recently examined for its potential as a superhard material [23][55][24]. This material is unexpectedly hard. Like any other orthorhombic structures, the unit cell in this material has four B_{12} icosahedra units at (0,0,0),(0,$\frac{1}{2}$, $\frac{1}{2}$), ($\frac{1}{2}$, 0, 0), ($\frac{1}{2}$, $\frac{1}{2}$, $\frac{1}{2}$). The remaining eight B atoms lie outside the icosahedra, bonding to the icosahedral B atoms and to the Al and Mg which appear not to enter at all to the bonding network [56]. Al atoms occupy a four-fold position at ($\frac{1}{4}$, $\frac{3}{4}$, $\frac{1}{4}$) and Mg atoms occupy a four-fold position at ($\frac{1}{4}$, 0.359, 0) as shown in Figure 3.7 with the icosahedra arranged in distorted, close-packed layers.

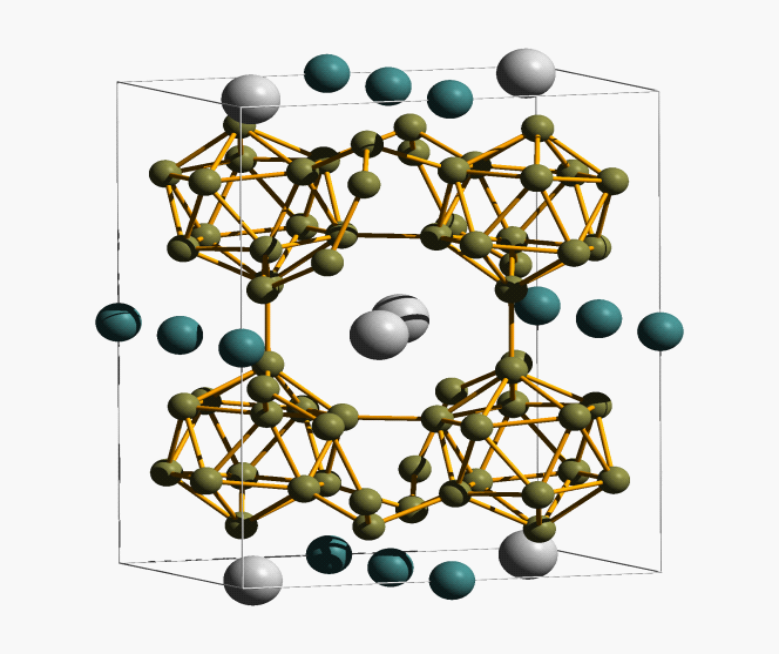


Figure 3.7: Crystal structure of $MgAlB_{14}$. Mg atoms are large spheres(white) and Al (teal).

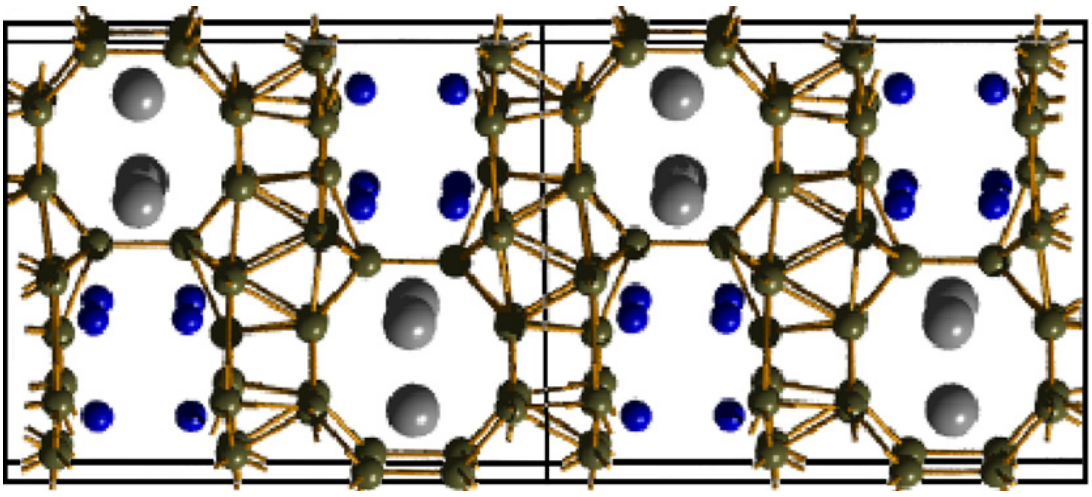


Figure 3.8: Crystal structure of MgC_2B_{14}. Large spheres are Mg.

$NaAlB_{14}$ structure [57] is very similar to $MgAlB_{14}$ and its unit cell parameters are close to the reported $LiAlB_{14}$ [58], $NaBB_{14}$, and $MgAlB_{14}$. The growth and refinement of this orthorhombic type structure was first reported by Okada [59].The crystal structure is orthorhombic, as with the $MgAlB_{14}$ structure type discussed above space group $Imma$. The Vickers microhardness of this material has been found to lie between 23-28 GPa for {100} and {010} faces respectively [59].

Recently another important boride hard material has been synthesized based on Mg and C that connect the B icosahedra [26]. In this material the B_{12} icosahedra is connected with Mg atoms and C units lying in trigonal voids. Carbon is then near tetrahedrally coordinated by three boron atoms and B_{12} icosahedra with long C–C bonds of length of 1.727Å similar to the chain model for B_4C. Moreover the tetrahedral linkage of the B atoms has similarity to the near tetrahedral linkage displayed in tetragonal boron that was illustrated in Figure 3.2

Some properties of boron rich solids based resulting from above structural features are:

· high melting points (above 2000 °C); e.g. boron about 2300 °C

· great hardness, 2000-4500 GPa. β-rhombohedral boron is the hardest elementary crystal after diamond.

· low density; e.g. 2.52 g.cm^{-3} B_4C

· low thermal expansion coefficient; e.g. 5.5 *10 $^{-6}$K^{-1} for B_6O

· high resistance to chemical attack, hence low corrosity

· high wear resistance

· high chemical inertness

· high and low neutron absorption cross section, caused by the ^{10}B or ^{11}B isotope

· semiconducting behavior

· good electrical resistivity; 50 Ωm for $MgAlB_{14}$

3.2 Experimental Studies

There have been considerable experimental and theoretical investigations of the structures and properties in boron and boron rich compounds because of their unusual bonding . In this and the following section we look at the previous work that have been done on boron icosahedral structures, using experimental studies and computer simulation studies. There are several polytypes of boron although three $\alpha-, \beta-$and tetragonal are important. Experimentally, it is known that at high temperatures β-boron is synthesized, while α-boron is metastable at ambient conditions, not thermodynamically stable and synthesized only at low temperatures. Experimental investigations of phonons in α-boron have been restricted to optical techniques. Tetragonal phases are intermediate between α-and β-boron [60, 61]. Of all known hard borides, boron carbides are among the best studied. Technical applications of such boron-carbon structures are limited with a variable homogeneity range but over a specific stoichiometry like B_4C. However detailed investigation of fundamental properties of such boron compounds has been impeded by the fact that is very difficult to grow

Table 3.1: Physicomechanical poperties of B_6O, B_4C and B_4Si

Samples	Density g.cm^{-3}	σ_{comp} (GPa)	Hardness (GPa)	Young Modulus (GPa)	Linear thermal expansion Coeffiecient (x10^{-6}K^{-1})
B_6O	2.4	63	32	440	5.5
B_4C	2.4	79	35	480	4.5
B_4Si	2.4	50.2	27	280	6.0

large crystals and they easily oxidizes at air atmosphere. Minghe Cao *et al* [62] prepared B_6O fibers by solid state reaction method using boron powders, CaO and Fe_3O_4 as starting materials. Hubert *et al* [63] studied B_6O properties by high pressure and high temperatures synthesis experiment using Walker-type multi anvil apparatus. Bairamashvili [64]investigated the physicomechanical properties including σ_{comp} (compressive strength) of B_6O, B_4C and B_4Si and fabricated them by a hot pressing technique in a compacting press in vacuum and at high temperatures. Table 3.1 lists physicomechanical properties of boride materials obtained in [64].

3.3 Computer Simulation Studies

Computer modelling techniques have also been used to study boron and boron rich compounds. Li and Ching [65] studied the structure and properties of four B_{12} based crystals using the self consistent orthorgonalized linear combination with the local density approximation (LDA) of density functional theory (DFT) to calculate the band structures and ground state properties. Their results were in good agreement with other existing first principle calculations using the pseudopotential plane-wave

method. Masago *et al* [60] studied the ground state and finite temperature properties of $\alpha-$ and $\beta-$boron using *ab initio* pseudopotentials method with LDA along with an iterative energy-minimization scheme. They clarified the features of $\beta-$boron by comparing them to to those of well studied $\alpha-$boron phase. There have been several speculations concerning the structure of B_4C, however recently it has been shown that the polar structure (where C enters the icosahedra) is more likely associated with a $B_{13}C_2$ stoichiometry [52] than the conventional chain structure (where C does not enter the icosahedra) with B_4C [53]. The electronic structures of various borides that hold potential for superhard material properties were investigated using Vienna *ab initio* simulation package (VASP) code that uses projector augmented pseudopotentials within LDA and generalized gradient approximation (GGA) [66]. Classical molecular dynamics have also been used to study elastic modulus of amorphous boron suboxide thin films on MOLDY code with Buckingham-like interaction potentials [67]. Lee estimated elastic properties of $MgAlB_{14}$ using first principle calculations [68]. Recently Kulikovsky *et al* [69] have investigated the mechanical properties and structure of amorphous and crystalline B_4C and suggested that carbon could segregate into clusters.

3.4 Potential Applications of Borides as Hard Materials

Ultra-hard materials are applied to tool surfaces for industrial operations such as cutting, grinding, chopping , drilling and milling. Boron based hard materials of the binary or ternary systems, B-C, B-N, B-O, or Mg-Al-B (e.g. B_4C, B_4N or $MgAlB_{14}$) might improve the technological applications of commercially available hard materials due to their combined high hardness and good oxidation resistance at elevated temperatures. Boron carbide (B_4C) is one of the hardest man made materials. B_4C is simple icosahedra which is an intrinsic superhard material and the most stable compound in the boron-carbon system. Technical application of boron-rich materials are largely limited on boron carbide, and even in the case of chemical composition, B_4C is the carbon-rich limit of the homogeneity range. B_4C materials are the most widely used in boron rich solids because of its high hardness. Industrially boron carbide powder is used as an abrasive in polishing and lapping applications, and also as a loose abrasive in cutting applications such as water jet cutting. It can also be used for dressing diamond tools. The extreme hardness of boron carbide gives it excellent wear and abrasion resistance and as a consequence it finds application as nozzles for slurry pumping, grit blasting and in water jet cutters.

Crystalline boron rich nitrides (B_xN) of the compositions $B_{25}N$ up to $B_{53}N$ as well as amorphous phases of the composition B_3N and B_5N have also been synthesized by

chemical vapor deposition (CVD) methods [70]. B_4N phase with analogous structure to B_4C has been described and the crystal structure consists of an icosahedra as in B_4C linked by N-B-N chains and with this structural feature the phase can be expected to exhibit interesting hardness properties [70]-[72]. The highly oxidation resistance boron based materials which have not yet resulted in the market due to low fracture toughness are the icosahedral boron suboxide (B_6O) materials. B-O materials are highly refractory and therefore they are suitable for the use on surfaces subject to abrasion, e.g. grinding wheels, drill bits, machine tools and in structures employed in extreme conditions. Aluminum infiltrated B_6O drag cutters and drill bits were successfully made and their stability were higher than 1800 °C (under vacuum), which exceeded that of polycrystalline diamond cutters [73].

$MgAlB_{14}$ films serves as an excellence protective coating for lithographite-galvanoformung-abf-ormung microdevices and silicon based microelectromechanical systems components because of its extreme hardness, exceptionally low coefficient of friction and strong adhesion to wide range of substrate materials [74]. Boron aluminum magnesium (BAM) materials project cost is cheaper to manufacture compared to diamond and cBN; and they have been successfully used as coating materials on WC/Co cutting tool inserts. BAM materials with small additions of TiB_2 increases the hardness of the materials and show lower wear rates and thus wear performance improves [75]. It is well accepted that the development of boride-based materials has been driven by the fact that they have a better oxidation resistance than diamond-based materials.

Therefore, boride materials are expected to have a great potential for new ultra-hard materials with industrial applications.

Chapter 4

Electronic Structure Methods

Electronic structure calculations obtain properties of a system from only the knowledge of the constituent atoms. The quantities which one would like to obtain by solving Hamiltonian, and which are useful for the interpretation of experimental results, are related to both the ground state and the excited states of the many electron system. For example, calculation of the cohesive energy will require knowledge of the ground state total energy, while the interpretation of a spectroscopic measurement will also require knowledge of excited state energies. In this calculations the ground state geometry of many electron system is found from considering the change in the energy of the system with regard to the change in the positions of the atomic nuclei. It is equivalent with studying the motions of the electrons and nuclei separately.

4.1 Adiabatic Approximation

The starting point in describing the properties of matter from theoretical method is the Hamiltonian for the system of electrons and nuclei. The ultimate goal of most quantum approaches is the approximate solution of the time independent, non relativistic Schrödinger equation

$$\hat{H}\Psi_i(\mathbf{x}_1, \mathbf{x}_2, ..., \mathbf{x}_N, \mathbf{R}_1, \mathbf{R}_2, ..., \mathbf{R}_M) = E_i\Psi_i(\mathbf{x}_1, \mathbf{x}_2, ..., \mathbf{x}_N, \mathbf{R}_1, \mathbf{R}_2, ..., \mathbf{R}_M) \quad (4.1)$$

where $\hat{H}$ is the Hamiltonian operator for the system consisting of M nuclei and N electrons in the absence of magnetic or electric field. The total Hamiltonian of a system containing atomic nuclei (ions) and electrons can be written as,

$$H = -\frac{\hbar^2}{2}\sum_n \frac{\nabla_n^2}{M_n} - \frac{\hbar^2}{2m_e}\sum_i \nabla_i^2 + V_{ion,ion} + V_{e,e} + V_{ion,e}. \quad (4.2)$$

The first two terms describe the kinetic energy of the nuclei and electrons respectively, where the Laplacian operator ∇_q^2 is defined as the sum of differential operators in Cartesian coordinates

$$\nabla_q^2 = \frac{\partial^2}{\partial x_q^2} + \frac{\partial^2}{\partial y_q^2} + \frac{\partial^2}{\partial z_q^2} \quad (4.3)$$

and

$$V_{ion,ion}(\{\mathbf{R}_n\}) = \frac{1}{2}\sum_{m,n\neq m}\frac{Z_n Z_m e^2}{|\mathbf{R}_n - \mathbf{R}_m|} \tag{4.4}$$

is the ion-ion interaction,

$$V_{e,e}(\{\mathbf{r}_i\}) = \frac{1}{2}\sum_{j,i\neq j}\frac{e^2}{|\mathbf{r}_i - \mathbf{r}_j|} \tag{4.5}$$

is the electron-electron interaction, and

$$V_{ion,e}(\{\mathbf{r}_i\},\{\mathbf{R}_n\}) = -\sum_n\sum_i\frac{Z_n e^2}{|\mathbf{R}_n - \mathbf{r}_i|} \tag{4.6}$$

is the electron-ion interaction. $\{\mathbf{r}_i\} \equiv (\mathbf{r}_1, \mathbf{r}_2, ..., \mathbf{r}_N)$ are the coordinates of the N electrons while $\{\mathbf{R}_n\} \equiv \mathbf{R}_1, \mathbf{R}_2, ..., \mathbf{R}_N$ are the coordinates of the N ions, with charge Z_n and mass M_n. $\Psi_i(\mathbf{x}_1, \mathbf{x}_2, ..., \mathbf{x}_N, \mathbf{R}_1, \mathbf{R}_2, ..., \mathbf{R}_M)$ stands for the wave function of the i'th state of the system and it contains all the information that can possibly be known about the quantum system. E_i is the numerical value of the energy of the state described by Ψ_i.

The Schrödinger equation can be further simplified if we take advantage of the significant differences between the masses of nuclei and electrons. The electron mass is much smaller than the nucleus mass. Hence the time scale for the electronic motion is much faster than for the nucleus movement and for practical consequences we can at least to a good approximation take the extreme point of view and consider the electrons as moving in the field of fixed nuclei. This is the adiabatic approximation of

Born and Oppenheimer [76], which is an excellent approximation for many purposes. For example the calculation of nuclear vibration modes in most solids. Thus the complete Hamiltonian given in equation (4.1) reduces to electronic Hamiltonian

$$H = -\frac{\hbar^2}{2m_e}\sum_i \nabla_i^2 + V_{e,e} + V_{ion,e}. \tag{4.7}$$

In this chapter we adopt Hartree atomic units $\hbar = m_e = e = 4\pi/\epsilon_0 = 1$ where e is the electronic charge, $\hbar$ is Plank's constant and m_e is the electronic mass. 1 Hartree = 2 Rydberg = 27.2 eV and the unit of length is the first Bohr radius so that 1 au = 0.529 Å. Then the terms may be written in the simpler form so that from equation (4.7), the Hamiltonian operator becomes

$$\begin{aligned} \hat{H} &= -\frac{1}{2}\sum_i \nabla_i^2 + \frac{1}{2}\sum_{j,i\neq j}\frac{1}{|\mathbf{r}_i - \mathbf{r}_j|} - \sum_n\sum_i \frac{Z_n}{|\mathbf{R}_n - \mathbf{r}_i|} & (4.8)\\ &= \hat{T} + \hat{V}_{int} + \hat{V}_{ext}. & (4.9) \end{aligned}$$

By solving this equation for a given ionic configuration, one obtains the electronic contribution to the total energy. The electronic equation must be treated within quantum theory, for example in Density Functional Theory, Quantum Monte Carlo technique, and mean field theory approximations like Hartree, Hartree-Fock, etc..

4.2 Hartree-Fock Approximation

All of the approximations [77] to the N-particle Hamiltonian have been aimed at constructing an accurate Hamiltonian for a single electron. In Hartree's suggestion, which is now called the Hartree approximation [78], is that an effective potential energy for the electron is determined by average motion of the other electrons:

$$V_H(\mathbf{r}) = e^2 \int \frac{d^3r' \rho(\mathbf{r}')}{|\mathbf{r} - \mathbf{r}'|}. \tag{4.10}$$

The quantity $\rho(\mathbf{r}')$ is the density of electrons in the system and it includes the contribution of the electron whose wavefunction is being calculated. It is related with number of electrons N by

$$N = \int \rho(\mathbf{r}) d\mathbf{r}. \tag{4.11}$$

Choosing this quantity represents problems because one is including a particle interacting with itself. An electron in a filled p-shell sees the Coulomb potential of five other electrons in the same shell, not six. Including self interaction makes an error and also for electrons in the conduction band of a solid. Trying to remove the self interaction from the electron density was successful by defining the density of other electrons, but it only introduces another problem of nonorthogonality. The Hartree approximation has conceptual problems regardless of how one formulates the potential.

Hartree-Fock (H-F) [79][80]approximation is the extension of Hartree approximation which is a standard method of many particle theory that was applied to atoms by Fock. He pointed out that Hartree approximation did not respect the principle of antisymmetric of the wavefunction by treating electrons as distinguishable particles. He then treated electrons as indistinguishable particles by proposing an antisymmetrized many electron wavefunction in the form of Slater determinant [81]:

$$\begin{aligned}
\Psi_{HF} &= \frac{1}{\sqrt{N!}} \begin{vmatrix} \psi_1(\mathbf{x}_1) & \psi_2(\mathbf{x}_1) & . & . & . & \psi_N(\mathbf{x}_1) \\ \psi_1(\mathbf{x}_2) & \psi_2(\mathbf{x}_2) & . & . & . & \psi_N(\mathbf{x}_2) \\ . & . & & & & . \\ . & . & & & & . \\ . & . & & & & . \\ \psi_1(\mathbf{x}_N) & \psi_2(\mathbf{x}_1) & . & . & . & \psi_N(\mathbf{x}_N) \end{vmatrix} \qquad (4.12) \\
&= \frac{1}{\sqrt{N!}} \det[\psi_1 \psi_2 ... \psi_N]. \qquad (4.13)
\end{aligned}$$

The Hartree Fock approximation is a method whereby the orthonormal orbitals ψ_i are found and minimize

$$E[\Psi] = \frac{\left\langle \Psi \left| \hat{H} \right| \Psi \right\rangle}{\langle \Psi | \Psi \rangle} \qquad (4.14)$$

where

$$\left\langle \Psi \left| \hat{H} \right| \Psi \right\rangle = \int \Psi^* \hat{H} \Psi d\mathbf{x} \tag{4.15}$$

for the determinant of Ψ. The normalization integral $\langle \Psi_{HF} | \Psi_{HF} \rangle$ is equal to 1 and the expectation value of the total energy is given by:

$$E_{HF} = \left\langle \Psi \left| \hat{H} \right| \Psi \right\rangle = \sum_{i=1}^{N} H_i + \frac{1}{2} \sum_{i,j=1}^{N} (J_{ij} - K_{ij}) \tag{4.16}$$

where

$$H_i = \int \psi_i^*(\mathbf{x}) [-\frac{1}{2} \nabla^2 + V_{ion,e}(\mathbf{x})] \psi_i(\mathbf{x}) d\mathbf{x} \tag{4.17}$$

defines the contribution due to the kinetic energy and the electron-nucleus attraction and

$$J_{ij} = \iint \psi_i(\mathbf{x}_1) \psi_i^*(\mathbf{x}_1) \frac{1}{r_{12}} \psi_j^*(\mathbf{x}_2) \psi_j(\mathbf{x}_2) d\mathbf{x}_1 d\mathbf{x}_2 \tag{4.18}$$

$$K_{ij} = \iint \psi_i^*(\mathbf{x}_1) \psi_j(\mathbf{x}_1) \frac{1}{r_{12}} \psi_i(\mathbf{x}_2) \psi_j^*(\mathbf{x}_2) d\mathbf{x}_1 d\mathbf{x}_2 \tag{4.19}$$

are the so called Coulomb and exchange integrals respectively which represents the interaction between two electrons. They are all real with $J_{ij} \geq K_{ij} \geq 0$ and equality $J_{ii} = K_{ii}$. The inclusion of exchange term is due to Pauli exclusion principle which is accounted in the Slater determinant wavefunction. The functions ψ_i and ψ_j

have been exchanged in the integrals so that electrons i and j have to be of the same spin for exchange to be nonzero.

Hartree-Fock equations can be solved in special cases and the basis must be introduced in such a way that the energy in equation (4.16) can be written in terms of the expansion coefficients of the orbitals and the integrals involving the basis. In the actual implementation, this transforms the mathematical problem into one or more matrix eigenvalue problem of high dimension, in which the matrix elements are calculated from arrays of integrals evaluated for the basis functions. The calculations are computationally demanding and shortcomings can be overcome by configuration interaction (CI) method or Møller-Plesset [82] perturbation theory. An alternative of H-F calculations is the density functional theory (DFT) in which certain elements in the Hamiltonian are evaluated at fixed points directly from the electron densities at those points. This can circumvent the need for calculating the enormous numbers of electron-electron repulsion integrals encountered in the H-F calculations. DFT has been the choice of electronic structure calculations in condensed matter physics and also used much in quantum chemistry because of its advantages over H-F methods.

4.3 Density Functional Theory

Density functional Theory (DFT) [81][83][84][85] is a primary theory of the electronic structure of atoms, molecules and solids in their ground states. It has became a tool for calculations of electronic structure in condensed matter and important for

qualitative studies and other finite systems using Hohenberg-Kohn-Sham [86][87] formalism. In this theory the electron density distribution $\rho(\mathbf{r})$ plays a central role for the interacting electron system in the presence of an external potential. This density of electrons is used as a physical variable in derivation of DFT functionals. DFT is based upon two mathematical theorems proved by Hohenberg-Kohn [86].

4.3.1 Constrained Search Formalism

The extension to degenerate states is due to the approach using improved derivations from Levy and Lieb called constrained search [88][89][90] formulations of density functional theory. It is very instructive because it extend the range of definition of a functional in a way that is formally is more tractable and clarifies its physical meaning. It also provides an in principle way to determine the exact functional which leads to the same ground state density and energy at the minimum as in Hohenberg-Kohn analysis.

We consider the Schrödinger equation for the ground state wave function Ψ_0 and energy E:

$$(\hat{T} + \hat{V}_{int} + \hat{V}_{ext})\Psi_0 = E\Psi_0 \tag{4.20}$$

where $\hat{T}$ is the kinetic energy operator, $\hat{V}_{int}$ is the electron-electron repulsion operator and external potential operator $\hat{V}_{ext}$. The ground state energy can be found by minimizing the energy with respect to all variables in Ψ

$$E = \min_{\Psi \to N} \left\langle \Psi \left| \hat{T} + \hat{V}_{int} + \hat{V}_{ext} \right| \Psi \right\rangle \tag{4.21}$$

which can be written as

$$\begin{aligned}
E &= \min_{\underline{\rho}(\mathbf{r}) \to N} \left\{ \min_{\Psi \to \underline{\rho}(\mathbf{r})} \left\langle \Psi \left| \hat{T} + \hat{V}_{int} + \hat{V}_{ext} \right| \Psi \right\rangle \right\} && (4.22)\\
&= \min_{\underline{\rho}(\mathbf{r}) \to N} \left\{ \min_{\Psi \to \underline{\rho}(\mathbf{r})} \left\langle \Psi \left| \hat{T} + \hat{V}_{int} \right| \Psi \right\rangle + \int d\mathbf{r} Tr \underline{\rho}(\mathbf{r}) \underline{V}_{ext}(\mathbf{r}) \right\} && (4.23)\\
&= \min_{\underline{\rho}(\mathbf{r}) \to N} \left\{ F[\underline{\rho}] + \int d\mathbf{r} Tr \underline{\rho}(\mathbf{r}) \underline{V}_{ext}(\mathbf{r}) \right\} && (4.24)\\
&= \min_{\underline{\rho}(\mathbf{r}) \to N} \left\{ F[\underline{\rho}] + \int d\mathbf{r} Tr \underline{\rho}(\mathbf{r}) \underline{V}^{\dagger}_{ext}(\mathbf{r}) \right\} && (4.25)
\end{aligned}$$

with

$$F[\underline{\rho}] = \min_{\Psi \to \underline{\rho}(\mathbf{r})} \left\langle \Psi \left| \hat{T} + \hat{V}_{int} \right| \Psi \right\rangle \tag{4.26}$$

$\underline{\rho}(\mathbf{r})$ and $\underline{V}_{ext}(\mathbf{r})$ are in spin space and $\underline{\rho}(\mathbf{r})$ is denoted as spin density defined by

$$\underline{\rho}(\mathbf{r}) = \begin{bmatrix} \rho^{\alpha}(\mathbf{r}) & \frac{1}{\sqrt{2}}\rho^{\gamma}(\mathbf{r}) + \frac{i}{\sqrt{2}}\rho^{\delta}(\mathbf{r}) \\ \frac{1}{\sqrt{2}}\rho^{\gamma}(\mathbf{r}) - \frac{i}{\sqrt{2}}\rho^{\delta}(\mathbf{r}) & \rho^{\beta}(\mathbf{r}) \end{bmatrix} \tag{4.27}$$

and

$$\underline{V}_{ext}(\mathbf{r}) = \begin{bmatrix} V^{\alpha}_{ext}(\mathbf{r}) & \frac{1}{\sqrt{2}}V^{\gamma}_{ext}(\mathbf{r}) + \frac{i}{\sqrt{2}}V^{\delta}_{ext}(\mathbf{r}) \\ \frac{1}{\sqrt{2}}V^{\gamma}_{ext}(\mathbf{r}) - \frac{i}{\sqrt{2}}V^{\delta}_{ext}(\mathbf{r}) & V^{\beta}_{ext}(\mathbf{r}) \end{bmatrix}. \tag{4.28}$$

Equations (4.24) and (4.25) are identical because of $\underline{V}_{ext}(\mathbf{r})$ is Hermitian $\underline{V}^{\dagger}_{ext}(\mathbf{r}) = \underline{V}_{ext}(\mathbf{r})$. Application of $\underline{V}^{\dagger}_{ext}(\mathbf{r})$ facilitates group theoretical analyses in the symmetry situation. The inner minimization in equation (4.25) defines the universal functional $F[\underline{\rho}]$ and runs over all antisymmetric wave functions Ψ yielding the spin density $\underline{\rho}(\mathbf{r})$ and the outer minimization runs over all densities integrating to N electrons. In this process the space of all antisymmetric wave functions with N electrons was divided into disjoint subspaces by the equivalence relation of having the same spin density. Then in each subspace the wave function with the lowest energy was determined and by comparing the minimizing wave functions of all subspaces the wave function Ψ_0 was obtained. The additional restriction that the density has to be associated with an external potential does not surface in this information. If the input density belongs to the class of $\underline{V}_{ext}$-representable densities, as is obviously the case for the ground state density which belongs to the corresponding $\underline{V}_{ext}$ in the Hamiltonian, the two functionals become identical,$F_{HK}[\rho] = F[\underline{\rho}]$. If the ground state density is selected, only one of the wave functions out of a set of functions connected with the same ground state energy is found in the constrained search.

Equation (4.26) defines the constrained search for the density functional $F[\underline{\rho}]$. It does not only provide a new proof for the first theorem of Hohenberg-Kohn, but also eliminates the original limitation that there be no degeneracy in the ground state. The variational search in equation (4.26) is constrained because the space of trial wave functions comprises only those that give the density, in construct to the search for

the minimum energy which is unconstrained because the space of trial wave functions is the whole N-particle Hilbert space.

4.3.2 Functionals for Exchange and Correlation

The exchange-correlation potential is crucial for the success of the DFT approach. The exchange correlation potential is a functional derivative of the exchange correlation energy, that is, exchange correlation functional, with respect to the local density. For homogeneous electron gas, this will depend on the value of the electron density. For nonhomogeneous system, the value of the exchange correlation potential at the point $\mathbf{r}$ depends on not only on the value of the density at $\mathbf{r}$ but also on its variation close to $\mathbf{r}$, and it can therefore be written as an expansion over the gradients to arbitrary order of the density:

$$V_{xc}[\rho(\mathbf{r})] = V_{xc}[\rho(\mathbf{r}), \nabla\rho(\mathbf{r}), \nabla(\nabla\rho(\mathbf{r})), ...]. \tag{4.29}$$

Apart from the fact that the exact form of the energy functional is unknown, including of density gradients makes the solution of the DFT equations rather difficult.

Local Density Approximation

The simplest way to obtain this contribution is to assume that the exchange correlation energy leads to an exchange correlation potential depending on the value of the density in $\mathbf{r}$ only and not on its gradients. We call this the local density approximation

(LDA):

$$E_{xc}^{LDA}\left[\rho(\mathbf{r})\right] = \int \rho(\mathbf{r})\varepsilon_{xc}[\rho(\mathbf{r})]d\mathbf{r} \tag{4.30}$$

where $\varepsilon_{xc}[\rho(\mathbf{r})]$ is the exchange correlation energy per particle of an homogeneous electron gas at density $\rho(\mathbf{r})$. The exchange-correlation potential is given by

$$\begin{aligned} V_{xc}^{LDA}(\rho\mathbf{r}) &= \frac{\delta E_{xc}^{LDA}}{\delta\rho(\mathbf{r})} && (4.31) \\ &= \varepsilon_{xc}[\rho(\mathbf{r})] + \rho(\mathbf{r})\frac{\partial\varepsilon_{xc}(\rho)}{\partial\rho}. && (4.32) \end{aligned}$$

The functional $\varepsilon_{xc}(\rho)$ be further be divided into the exchange and correlation energy contributions,

$$\varepsilon_{xc}(\rho) = \varepsilon_x(\rho) + \varepsilon_c(\rho). \tag{4.33}$$

From Dirac exchange functional, the exchange part is

$$\varepsilon_x(\rho) = A_x\rho(\mathbf{r})^{\frac{1}{3}} \tag{4.34}$$

with

$$A_x = -\frac{3}{4}\left(\frac{3}{\pi}\right)^{\frac{1}{3}} \tag{4.35}$$

in atomic units. The exchange is due to Pauling exclusion principle.

The correlation energy is known only for extreme limits of low and high densities. For low density limit which also known as a strong coupling limit, the energy is

$$\varepsilon_c(\rho) = \frac{d_0}{r_s} + \frac{d_1}{r_s^{\frac{3}{2}}} + ... \tag{4.36}$$

The constants d_0 and d_1 can be estimated from the Madelung electrostatic and zero-point vibrational energies of the Wigner crystal, respectively. The high density ($r_s \to 0$) limit is called the weak coupling limit, and the correlation energy is

$$\varepsilon_c(\rho) = c_0 \ln r_s - c_1 + c_2 r_s \ln r_s - c_3 r_s + ... \tag{4.37}$$

and is from many body-perturbation theory. The constants $c_0 = 0.031091$ and $c_2 = 0.046644$ are known [91].

The LDA is generally very successful in predicting structures and ground state properties of materials but some shortcomings are well documented [92]. These concern in particular:

(i) the energies of excited states, in particular the band gaps in semiconductors and insulators are systematically underestimated. This is not surprising since DFT is based on a theorem referring to the ground state only.

(ii) Generally LDA tends to significantly overestimate cohesive energies and underestimate lattice parameters by up to 3%. In solids, the former is thought to occur

because the LDA does a poor calculation of the total energy in isolated atoms [93].

(iii) The incorrect ground state is predicted for some magnetic systems (the most notable example is Fe which is predicted to be hexagonal close packed and non-magnetic instead of body centered cubic and ferromagnetic) and for strongly correlated systems.

(iv) Van der Waals interactions are not appropriately described in the LDA, although there are some suggestions for overcoming this problem [94][95].

Generalized Gradient Approximation

In the LDA one exploits knowledge of the density at point $\mathbf{r}$. Any real system is spatially inhomogeneous, that is, it has a spatially varying density and it would be clearly useful to also include the information on the rate of this variation in the functional.

The functional of the general form

$$E_{xc}^{GGA} = \int \rho(\mathbf{r})\varepsilon_{xc}[\rho(\mathbf{r})]d\mathbf{r} + \int F_{xc}[\rho(\mathbf{r}), \nabla\rho(\mathbf{r})]d\mathbf{r}$$

have become known as the generalized gradient approximation (GGA) and the functional F_{xc} satisfy a number of formal conditions for the exchange-correlation hole. Different GGAs differ in the choice of the function. In particular, GGAs used in quantum chemistry typically proceed by fitting parameters to test sets of selected molecules. On the other hand, GGAs used in physics tend to emphasize exact con-

straints. The most popular (and most reliable) GGAs are PBE [96][97] in physics and BLYP [98][99] in chemistry. Many other GGA-type functionals are also available, and new ones continue to appear.

In this thesis we used the PBE form of GGA not only that is a simpler form and is simple to derive, but also that the functional hold correct features of LSDA and combines them with the most features of gradient corrected nonlocality. The correlation energy for this GGA is written in the form:

$$E_c^{GGA-PBE}[\rho_\uparrow, \rho_\downarrow] = \int \rho(\mathbf{r})[\varepsilon_c^{LDA}(r_s, \zeta) + H(r_s, \zeta, t)]d\mathbf{r} \tag{4.38}$$

where r_s is the local Seitz radius. Radius of a sphere on average contains one electron and is related to electron density by:

$$\rho = \frac{3}{4\pi r_s^3} \tag{4.39}$$

$$= \frac{k_F^3}{3\pi^2}, \tag{4.40}$$

and

$$\zeta = \frac{\rho_\uparrow - \rho_\downarrow}{\rho} \tag{4.41}$$

is the relative spin polarization and reduced density gradient given by:

$$t = \frac{|\nabla\rho|}{2\phi k_s \rho} \tag{4.42}$$

$$= \sqrt{\frac{\pi}{4}}\left(\frac{9\pi}{4}\right)^{\frac{1}{6}} \frac{s}{\phi\sqrt{r_s}}. \tag{4.43}$$

Here

$$\phi(\zeta) = \frac{1}{2}[(1+\zeta)^{\frac{2}{3}} + (1-\zeta)^{\frac{2}{3}}] \tag{4.44}$$

is a spin-scaling factor and

$$k_s = \sqrt{\frac{4k_F}{\pi a_0}} \tag{4.45}$$

is the Thomas-Fermi screening wave number with

$$a_0 = \frac{\hbar}{2me^2}, \tag{4.46}$$

where k_F is the Fermi wave vector.

$$H(r_s, \zeta, t) = \frac{e^2}{a_0}\gamma\phi^3 \ln\left\{1 + \frac{\beta}{\gamma}t^2\frac{1+At^2}{1+At^2+A^2t^4}\right\} \tag{4.47}$$

where the factor $\frac{e^2}{a_0}$ with a_0 the Bohr radius, is the unity in atomic units. The quantity $\beta \cong 0.066725$ and $\gamma \cong 0.031091$. The correlation term satisfy the following

conditions:

(i) it tends to correct second-order gradient expansion in the slowly varying limit ($t \longrightarrow 0$) in the high density ($r_s \longrightarrow 0$) limit,

(ii) it tends to minus uniform electron gas correlation energy -ε_c^{LDA} for rapidly varying densities ($t \longrightarrow \infty$), making correlation energy vanish, and

(iii) under uniform scaling to the high-density limit, the correlation energy scale to a constant, thus it cancels the logarithm singularity of ε_c^{LDA} in this limit.

The function A has the following form:

$$A = \frac{\beta}{\gamma}\left[\exp\left(\frac{\varepsilon_c^{LDA}}{\gamma\phi^3} - 1\right)\right]^{-1}. \tag{4.48}$$

The exchange energy is given by:

$$E_x^{GGA-PBE}[\rho_\uparrow, \rho_\downarrow] = \int \rho(\mathbf{r})\boldsymbol{\varepsilon}_x^{LDA}(\rho)F_x(s)]d\mathbf{r} \tag{4.49}$$

where F_x is an explicit enhancement factor

$$F_x = 1 + \frac{10}{81}s_1 + \frac{146}{2025}s_2^2 + ... \tag{4.50}$$

and s is another dimensionless density gradient given by:

$$s = \frac{|\nabla\rho|}{2k_F\rho} \tag{4.51}$$

$$= \sqrt{\frac{r_s}{a_0}}\frac{\phi t}{c} \tag{4.52}$$

for

$$c = \left(\frac{3\pi^2}{16}\right)^{\frac{1}{3}} \tag{4.53}$$

$$\cong 1.2277. \tag{4.54}$$

The simple form for the enhancement factor is chosen with $F_x(0) = 1$, so that the local approximation is recovered and $F_x \longrightarrow constant$ at large s,

$$F_x(s) = 1 + k - \frac{k}{\left(\frac{1+\mu s^2}{k}\right)} \tag{4.55}$$

where $k = 0.804$, $\mu = \beta\left(\frac{\pi^2}{3}\right) \cong 0.21951$. Becke [100] proposed this form with empirical coefficients $k = 0.967$, $\mu = 0.235$. This form is chosen because it obeys the spin-scaling relationship, it recovers the LDSA linear response limit as $s \longrightarrow 0$, for we have $F_x(s) = 1 + \mu s^2$(that is, it is chosen to cancel the term from the correlation), and it satisfies the Lieb-Oxford bound, with s to a maximum value less than or equal to 2.273, that is $F_x(s) \leq 1.804$.

4.4 Plane waves and Pseudopotentials

This section is organized to give the methods of solving the electronic structure calculation using density functionals which aims to compute the properties of interest. The pseudopotential method [101] forms the fundamental basis for the analysis of the properties of materials. The two methods used to solve Kohn-Sham equations are plane wave basis set and the all electron (AE) or the pseudopotential approximation for the electronic state expansion and treatment of the core states and they are referred as *ab-initio* methods. The AE approach treats the core and valence states while the pseudopotential approximation eliminates the core states. In using approximate methods for calculating energies and properties, the accuracy of the answer will depend upon the particular choice of the pseudopotential. We will end this chapter with a short discussion of the software package VASP that implements these methods.

4.4.1 Plane Waves Basis Sets

A single electron wavefunction is given by:

$$\Psi_i(\mathbf{r}) = \sum_{j=1}^{\infty} c_j \psi_j(\mathbf{r}) \tag{4.56}$$

where ψ_j are members of complete set of functions. Using Bloch's theorem [102], which starts with the periodicity of the crystal and also gives the boundary condition for a single particle wavefunction, we have:

$$\Psi_i(\mathbf{r}) = e^{i\mathbf{k}.\mathbf{r}} f_i(\mathbf{r}) \tag{4.57}$$

where the first term is like the wavelike part and the second term is the cell periodic part of the wavefunction. The periodic part can be expanded in terms of discrete finite sets of plane waves whose wave vectors are the reciprocal lattice vectors of the crystal,

$$f_i(\mathbf{r}) = \sum_{\mathbf{G}} c_{i,\mathbf{G}} e^{i\mathbf{G}.\mathbf{r}} \tag{4.58}$$

where G is the reciprocal lattice vectors which are defined by

$$\mathbf{G}.\mathbf{l} = 2\pi m \tag{4.59}$$

for all $\mathbf{l}$ where $\mathbf{l}$ is the lattice vector of the crystal and m is an integer. Thus the electronic wavefunction can be written as the sum of the plane waves

$$\Psi_i(\mathbf{r}) = \sum_{\mathbf{G}} c_{i,\mathbf{k}+\mathbf{G}} e^{i(\mathbf{k}+\mathbf{G}).\mathbf{r}}. \tag{4.60}$$

Large number of plane waves [103] are needed because the real wavefunctions vary rapidly near the nuclei and so a large number of Fourier components are needed to properly expand the eigenstates. The number of wavefunctions used is controlled by the largest wave vector in the expansion in equation (4.58). However, the coefficients

of for the plane waves $c_{i,\mathbf{k}+\mathbf{G}}$, each have a kinetic energy $(\hbar^2/2m)\,|\mathbf{k}+\mathbf{G}|^2$. The plane waves with smaller kinetic energy are typically more important than those with larger kinetic energy. The introduction of plane wave energy energy cutoff reduces the basis set to a finite size. A finite kinetic energy cutoff will lead to an error in the computed total energy of the system. It is possible to make the error arbitrary small by increasing the size of basis set by allowing larger cutoff. In principle, the cutoff energy should be increased until the calculated energy converges within the required tolerance and this depends on the system under investigation. This cutoff is implemented in chapter 5 for crystal of structures of boron and boride materials.

When plane waves are used as basis set for electronic wavefunctions, the Kohn-Sham equations assume simple form [104]. Substitution of equation (4.60) into Kohn-Sham equations, we have

$$\sum_{\mathbf{G}'} \left\{ \frac{\hbar^2}{2m} \left|\mathbf{k}+\mathbf{G}\right| \delta_{\mathbf{G}\mathbf{G}'} + V_{eff}(\mathbf{G}-\mathbf{G}') \right\} c_{i,\mathbf{k}+\mathbf{G}'} = \varepsilon_i c_{i,\mathbf{k}+\mathbf{G}}. \tag{4.61}$$

The reciprocal space representation of the kinetic energy is diagonal with the various potential contributions being described in terms of their Fourier components. The usual methods of solving the plane wave expansion of the Kohn-Sham equations is by diagonalization of the Hamiltonian matrix whose elements $H_{\mathbf{k}+\mathbf{G},\mathbf{k}+\mathbf{G}'}$ are given by the curly brackets. It follows that the size of the matrix is determined by the energy cutoff

$$E_c = \frac{\hbar^2}{2m} |\mathbf{k} + \mathbf{G}|^2 . \tag{4.62}$$

Calculations using plane waves basis sets can also be applied to non-periodic systems such as molecules or clusters. To accomplish this, the molecule is placed at the center of a periodic supercell. If the supercell is large enough the interactions between the molecules in neighboring cells becomes negligible. This is illustrated in Figure 4.1.

Supercells are used to study infinite solids and a periodic systems within a conventional unit cell. In the case of solids, the total energy and many other properties depend on the integration of some well defined mathematical quantity over Brillouin zone. The k-points for this integration are typically chosen according to the scheme of Monkhorst and Pack [105]. For a periodic system, like molecules and defects in solids, larger and larger unit cells are used until finite size effects are eliminated.

Even with pseudopotentials, the plane wave approach is in general very expensive for large unit cells especially if there is much vacuum because the plane waves exist everywhere in space, all overlap with each other, while the localized orbitals exist only near the nuclei and so overlap only with neighbors.

4.4.2 Pseudopotentials

Pseudopotentials were originally introduced to simplify electronic structure calculations by eliminating the need to include atomic core states and strong potentials

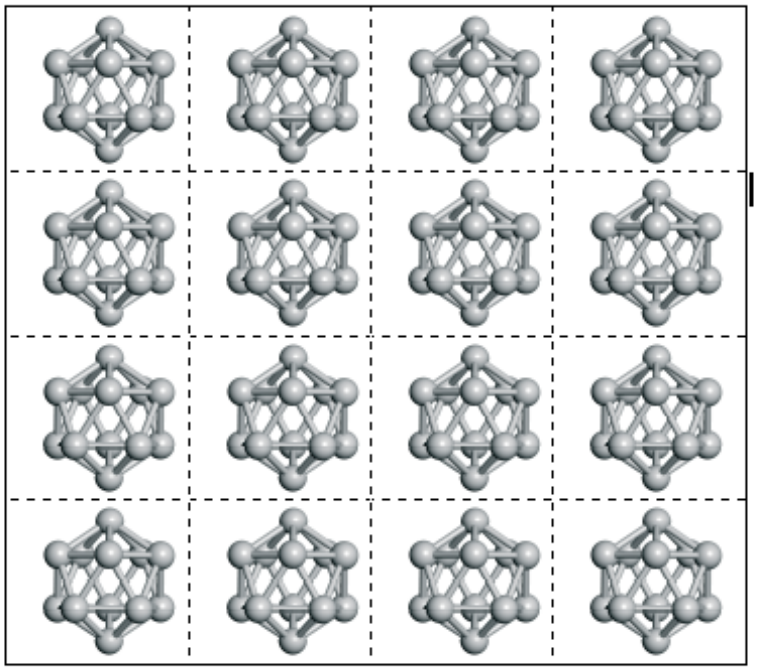


Figure 4.1: Supercell geometry for an isolated molecule (icosahedron). The dashed lines encloses the periodic supercell.

responsible for binding them [106]. The pseudopotential approximation [107] allows electronic wavefunctions to be expanded using a much smaller number of plane wave basis set. Most physical solids are dependent on the valence electrons to much greater extend than on the core electrons. Then pseudopotential exploits this by removing the core electrons and replacing them and the strong ionic potential is replaced by weaker pseudopotential that acts on a set of pseudo wavefunctions rather than the true valence wavefunctions. An ionic potential, valence wavefunction and the corresponding pseudopotential and pseudo wavefunction are illustrated schematically in Figure 4.2. The radius at which all-electron and pseudopotential values match is designated r_c [104].

For an *ab initio* pseudopotential calculation to be performed on a solid, there must be a pseudopotential for each element [103]. A pseudopotential is constructed by solving the Kohn-Sham equation for that element in the atomic environment. The hope is that the pseudopotential is transferable to other environments. Although there are distinct pseudopotential implementations, they are always constructed with the following atomic properties:

1. Core states are completely removed. The valence states are orthogonal to these frozen core states

2. The eigenvalue for the valence state pseudo wavefunction are equal to their all-electron values.

3. The all-electron wavefunctions for the valence states are replaced by smoother

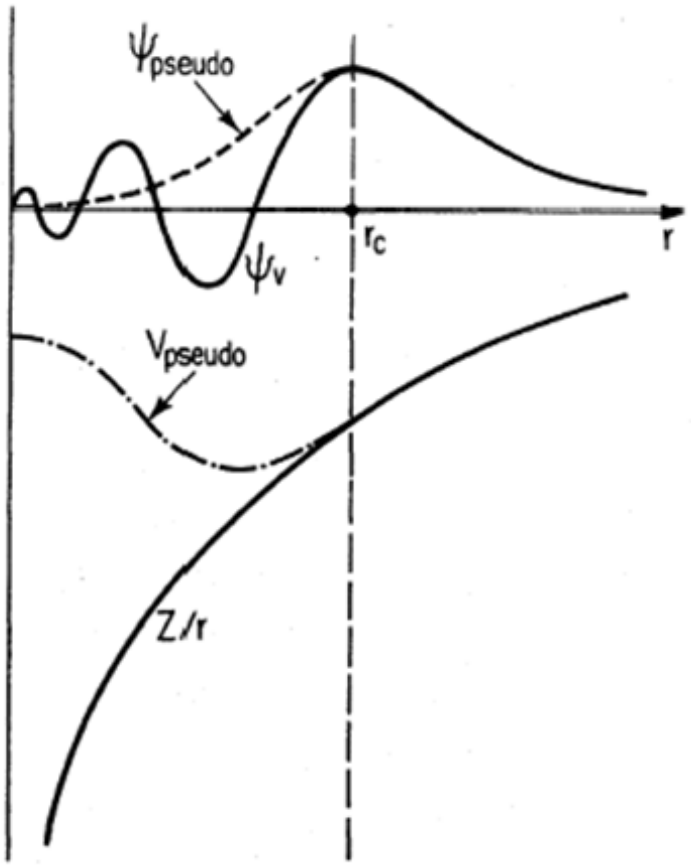


Figure 4.2: Schematic illustration of all-electron (solid lines) and pseudoelectron (dashed lines) potentials and their corresponding wavefunctions.

pseudo wavefunctions which match beyond a cutoff radius r_c.

The most general form for a pseudopotential is

$$\hat{V}^{ps} = \sum_{l=0}^{l_{\max}} \sum_{m=-l}^{l} |Y_{lm}\rangle \, V_l^{ps}(r) \, \langle Y_{lm}| \tag{4.63}$$

or in the real space representation,

$$\begin{aligned} V^{ps}(\mathbf{r}, \mathbf{r}') &= \left\langle \mathbf{r} \left| \hat{V}^{ps} \right| \mathbf{r}' \right\rangle & (4.64) \\ &= \sum_{l=0}^{l_{\max}} \sum_{m=-l}^{l} Y_{lm}(\theta, \phi) V_l^{ps}(r) \delta(r - r') Y_{lm}(\theta', \phi') & (4.65) \end{aligned}$$

which shows that it is non local in the angular variable but local in the radial variables. For the potential to be useful in other environments, the contributions from the Hartree and exchange-correlation potential must be from it. The unscreened pseudopotential is then given by

$$V_l^{ps}(r) = V_l^{ps,scr}(r) - V_{Hartree}[\rho^{ps}(\mathbf{r})] - V_{xc}[\rho^{ps}(\mathbf{r})] \tag{4.66}$$

where $\rho^{ps}(\mathbf{r})$ is the pseudo charge density constructed from the valence state of the atomic pseudo wavefunctions $\Psi_{lm}^{ps}(r)$.

The use of plane wave basis set with pseudopotential [108] originally arose for the study of crystalline systems, it has been applied to non-periodic systems such as

molecules [109][110] and polymers [111]. The pseudopotential plane wave method is also commonly used in *ab initio* molecular dynamics simulation schemes such as the Car-Parrinelo method [112].

4.4.3 The PAW method

The projector augmented wave (PAW) method [113] is a general approach developed by Peter Bloch [114] of an augmented wave method and the pseudopotential approach. It extends and combines the traditions of existing augmented wave methods and the pseudopotential approach into unified electronic structure method and is probably the optimal tradeoff between accuracy and computational efficiency. Like the "ultrasoft" pseudopotential method, PAW method introduces projectors and auxiliary localized functions. The PAW approach also defines a functional for the total energy that involves auxiliary functions and it uses advances in algorithms for efficient solution of the generalized eigenvalue problem. The formal relationship that exist between the ultrasoft pseudopotential and the PAW method has been derived by Kresse and Joubert [115] and both methods are implemented in the VASP code [116] which is valuable to predict properties that depend on the full wave functions.

4.5 VASP Code

Vienna *ab initio* Simulation Package (VASP) code [117][116][118][119] is a density functional code which solves the Kohn-Sham equations of local density or spin density functional theory, iteratively within a plane wave basis set. The electronic ground state is determined either by conjugate gradient algorithm as optimized by Teter [120], or by blocked Davidson [121] scheme or via an unconstrained band-by-band matrix-diagnolization scheme based on the residual minimization method [118][122].

VASP perform *ab-initio* quantum-mechanical molecular dynamics (MD) simulations using pseudopotentials or the projector-augmented wave method and a plane wave basis set. The approach implemented in VASP is based on the (finite-temperature) local-density approximation with the free energy as variational quantity and an exact evaluation of the instantaneous electronic ground state at each MD time step. VASP uses efficient matrix diagonalization schemes and an efficient Pulay/Broyden charge density mixing. These techniques avoid all problems possibly occurring in the original Car-Parrinello method, which is based on the simultaneous integration of electronic and ionic equations of motion. The interaction between ions and electrons is described by ultra-soft Vanderbilt pseudopotentials (US-PP) [123]or by the projector-augmented wave (PAW) method [114]. US-PP (and the PAW method) allow for a considerable reduction of the number of plane-waves per atom for transition metals and first row elements. Forces and the full stress tensor can be calculated with VASP and used to relax atoms into their instantaneous ground-state.

Besides the local density approximation (LDA) for the exchange and correlation functional, the gradient corrected functionals are also implemented in VASP to account the non locality in the exchange and correlation.

Chapter 5

Ab-initio Computational Results

In this chapter we present the results obtained by electronic structure method implemented on VASP code.

5.1 Convergence

Obtaining converged total energies with respect to the energy cutoff is vital before attempting any structural predictions. Borides investigated here consist of large units cells of at least 36 atoms per unit cell and so for convergence tests this will require more computer memory and time. Hence we used the automated kinetic energy cutoff of 398,45.eV, 398.5 $eV$and 500 eV for tetragonal, orthorhombic and rhombohedral structures respectively. In all calculations each atom in the system was allowed to fully relax with a convergence criterion of at least 10^{-4} eV/atom placed on self consistent convergence of the total energy. For these tests we used the local density

Table 5.1: The number of k-points and total energy of LDA convergence test

Material	**Total Energy** (eV)	**Number of k-points**	**Monkhorst-Pack set**
$MgAlB_{14}$	-449.0449	4	2x2x2
	-448.9085	8	4x4x4
	-448.9184	27	6x6x6
	-448.9147	64	8x8x8
$NaAlB_{14}$	-451.3606	4	2x2x2
	-451.3909	8	4x4x4
	-451.3884	27	6x6x6
	-451.38837	64	8x8x8

approximations (LDA).

5.1.1 k-points

Since we are comparing the energies of different structures with different unit cell volumes and Brillouin shapes, sizes and k-point sampling, we need a good convergence of the energy. An appropriate choice of k-point set is important for achieving balance between accuracy and efficiency. The Brillouin zone sampling was carried out using the number of k-points as indicated in Table 5.1, within the irreducible part of the zone.

This corresponds to the Monkhost-Pack set [105] of points given in the last column in Table 5.1. In this part, we show the convergence of the total energies with respect to the k-points for $MgAlB_{14}$ and $NaAlB_{14}$ shown in Figure 5.1 and Figure 5.2 respectively. We performed the convergence tests on the orthorhombic structures because they are complex and contain large number of atoms in the unit cell than all

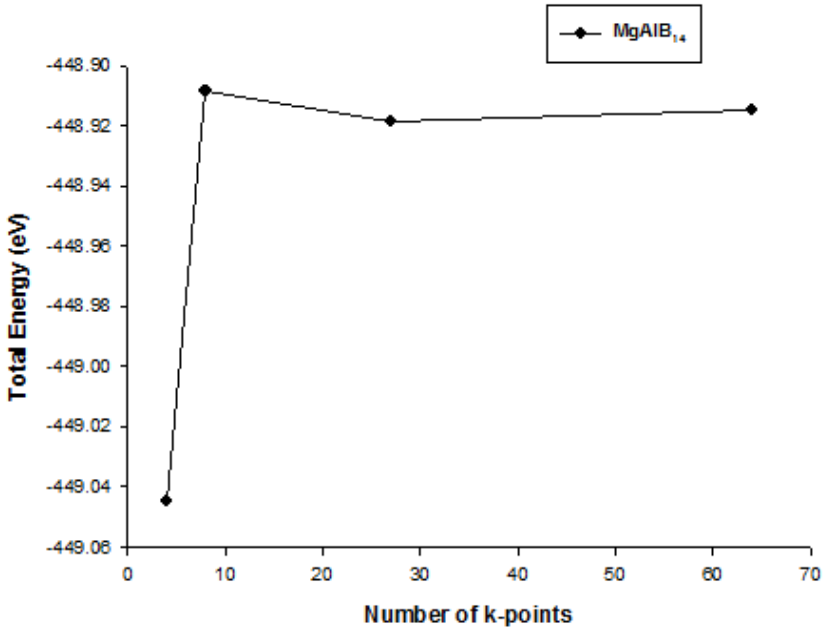


Figure 5.1: Total energy versus number of k-points for $MgAlB_{14}$

other structures, that is, they have 64 atoms per unit cell.

The total energy was considered converged when the change was within 1 meV. From this, k-points set were chosen 6×6×6 Monkhort-Pack [105] grid for all structures investigated in this work, since further increase of the k-point set density had no significant effect on calculated properties. An increased k-point set reduces the finite basis set correction and makes cell relaxation more accurate at a fixed energy cutoff.

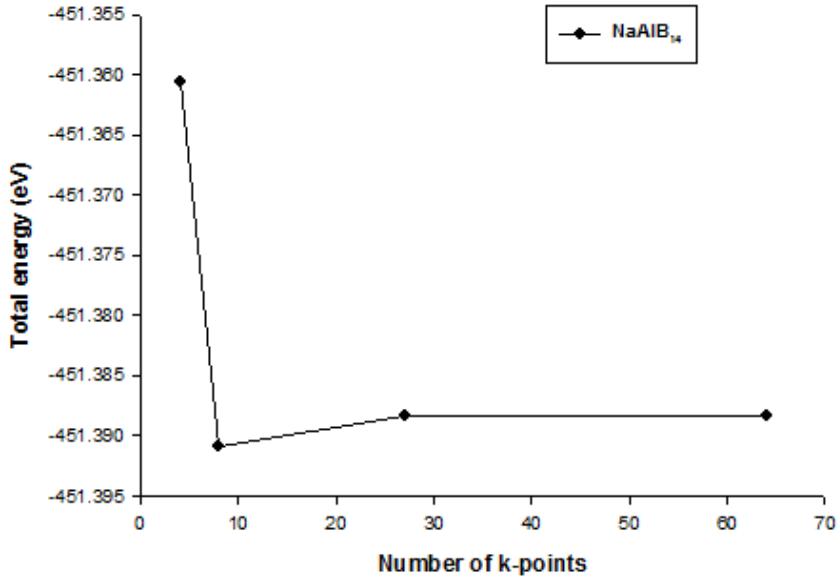


Figure 5.2: Total energy versus number of k-point for $NaAlB_{14}$

5.2 Equilibrium Properties

5.2.1 Computational Procedure

To study the electronic structure of the various borides Vienna *ab initio* Simulation Package (VASP) [117] code was used for relaxation of structure and the calculation of bulk moduli using equation of state. We also employed a computational technique that uses projector augmented wave (PAW) [114][115] pseudopotentials within local density approximation (LDA) functional of Ceperly and Alder [91], as parametrized by Perdew and Zunger [124] and generalized gradient approximation (GGA) [96] employing a plane wave basis calculated on a 6×6×6 **k** points Monkhorst-Pack grid

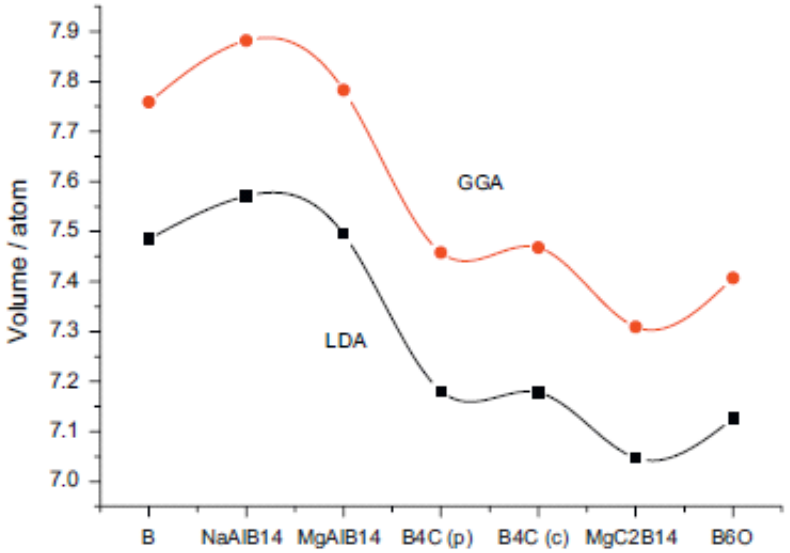


Figure 5.3: Trends in volume

[105]. In all calculations each atom in the system was allowed to fully relax with a convergence criteria of at least 10^{-4} eV/atom placed on self consistent convergence of the total energy.

5.2.2 Equilibrium Atomic Volume

Our calculated equilibrium atomic volumes and equilibrium lattice parameters of the boride materials of the crystal structures shown earlier in Figures 3.2 to Figure 3.8 are tabulated in Table 5.2, with experimental values for comparison purpose.

Agreement between *ab initio* calculation and experiment generally is quite good. It clear that there is some trend occurring especially between B_{50}, B_4C and B_6O. The equilibrium atomic volumes trend is shown in Figure 5.3.

Table 5.2: Structural properties of various Boron related compounds together with available experimental and theoretical calculations. Calculated GGA values in brackets

Material	No	V_0	Lattice (Å)	
			This work	Experiment
B_{50}	50	7.474	a = 8.734	a = 8.75[47]
		(7.447)	(8.840)	
($P4_2/nnm$)			c = 4.903	c = 5.06[47]
			(4.961)	
B_4C polar	45	7.170	a = 5.697	a = 5.61[125], 5.60[126]
		(7.447)	(5.764)	
($R\bar{3}m$)			c = 11.604	c = 12.14[125], 12.0-12.10[126]
			(11.758)	
B_4C chain	45	7.167	a = 5.577	
		(7.457)	(5.643)	
($R\bar{3}m$)			c = 11.969	
			(12.139)	
B_6O	42	7.115	a = 5.392	a = 5.382[127], 5.367[128]
		(7.793)	(5.393)	
($R\bar{3}m$)			a = 12.151	c = 12.323[127], 12.328[128]
			(12.314)	
$NaAlB_{14}$	64	7.560	a = 5.911	a = 5.844[59]
		(7.871)	(5.848)	
*(*Im*am)*			b = 10.355	b = 10.465
			(10.460)	
			c = 8.110	c = 8.231
			(8.226)	
$MgAlB_{14}$	64	7.772	a = 5.844	a = 5.848[129]
		(7.484)	(5.911)	
(Im am)			b = 10.218	b = 10.313
			(10.355)	
			c = 8.017	c = 8.115
			(8.118)	
MgC_2B_{14}	60	7.036	a = 5.547	a = 5.613[26]
(Im am)		(7.298)	(5.616)	b = 9.828
			b = 9.695	c = 7.933
			(9.821)	
			c = 7.846	
			(7.935)	

5.2.3 Equation of State and Bulk Modulus

The equilibrium properties of solids can be derived from the thermodynamic Helmholtz free energy

$$E(T,V) = E_0(V) + E_{vib}(T,V) \tag{5.1}$$

where E_0 is the minimum energy without vibrational contributions E_{vib}. The equation of state (EOS) of a solid which is associated with pressure, volume and temperature relation is fundamentally important in basic and applied science. It depends on the nature of the interatomic interactions and thus provides a test of fundamental solid state theories. At the same time it can be used to determine thermodynamic properties. The EOS [130] is obtained by computing the pressure given by

$$P = \left(-\frac{\partial E}{\partial V}\right)_T \tag{5.2}$$

for different volumes and at minimum volume V_0 the isothermal bulk modulus is given by

$$B = -V_0\left(\frac{\partial P}{\partial V}\right)_T \tag{5.3}$$

$$= V_0\left(\frac{\partial^2 E}{\partial V^2}\right)_T \tag{5.4}$$

The isothermal $P - V$ relation can be described in several approximations, but in most common and the simplest approach, the equation of state is represented by Murnaghan [131], who assumed that near equilibrium, the bulk modulus varies linearly with pressure,

$$B(P) = B_0 + B_0' P \tag{5.5}$$

where B_0 is the isothermal bulk modulus. Upon integration one obtains the Murnaghan equation of state:

$$E(V) = \frac{B_0 V}{B_0'(B_0' - 1)} \left[B_0' \left[1 - \frac{V_0}{V} \right] + \left[\frac{V_0}{V} \right]^{B_0'} - 1 \right] + E(V_0) \tag{5.6}$$

where V_0 is the isothermal volume. The Birch equation of state [132] is a strain f expansion usually provides a better description of the compression of most solids:

$$P = 3B_0 f(1 + 2f)^{\frac{5}{2}} \left[1 + af + bf^2 \right] \tag{5.7}$$

here f is Eularian strain parameter

$$f = \left(\left[\frac{V_0}{V} \right]^{\frac{2}{3}} - 1 \right) /2, \tag{5.8}$$

and a and b are constants. The pressure derivative of the bulk modulus B_0' is related to the constant a by

$$B_0' = \frac{2a}{3} + 4 \tag{5.9}$$

and the term bf^2 is neglected. Then is possible to derive the bulk modulus B, its pressure derivative B', the minimum energy $E(V)$ and the equilibrium volume from the calculated energy-volume data through

$$E(V) = \frac{9}{16} B_0 V_0 \left\{ 6 - B_0' + \left(\frac{V_0}{V}\right)^{\frac{2}{3}} \left[\begin{array}{c} (B_0' - 4)\left(\frac{V_0}{V}\right)^{\frac{2}{3}} - \\ (3B_0' - 14)\left(\frac{V_0}{V}\right)^{\frac{2}{3}} + 3B_0' - 16 \end{array} \right] \right\} + E(V_0) \tag{5.10}$$

In these boride materials the bulk modulus B, calculations and its pressure derivatives, B' were achieved by decreasing and increasing the volume of the structure about its equilibrium geometry and fitting the energy-volume data to Birch [132] equation of state. The resulting $E - V$ curves for these materials are shown in Figures 5.5 and Figure 5.6 and the calculated bulk modulus modulus and equation of state parameters are shown in Table 5.3 with the trend in bulk modulus shown in Figure 5.4.

The low value of bulk modulus for $MgAlB_{14}$ is consistent with other calculations employing alternative approaches [56][133]. To attempt an understanding as to the origin of this trend we examine closer the electronic structure of these materials.

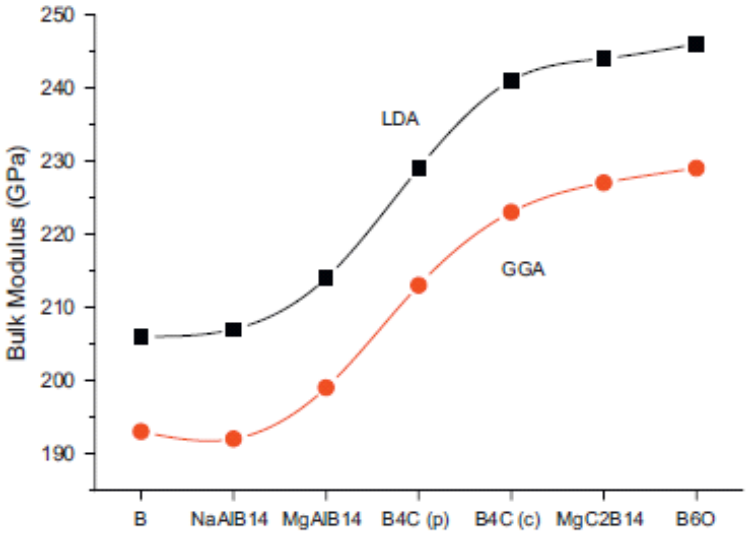


Figure 5.4: Trends in bulk modulus

Table 5.3: Bulk Moduli B, pressure derivatives B' of various Boron compounds and some experimental and theoretical values. GGA values in brackets.

Material			Bulk modulus B(GPa)	
	This Work	B'	Experiment,{B'}	Other Calculations
B_{50}	206	3.8		220[29]
	(193)	(3.9)		
B_4C polar	229	3.5	241[127]	217[134]
	(213)	(3.7)		227[135]
B_4C chain	241	3.7		250[56]
	(223)	(3.6)		
B_6O	246	3.3	270{1.8}[21]	237[135]
	(229)	(3.4)	213{4}[21]	268[65]
			181{6}[136]	
$MgAlB_{14}$	214	3.7		212[133]
	(199)	(3.7)		
$NaAlB_{14}$	207	3.7		
	(192)	(3.8)		
MgC_2B_{14}	244	3.8		
	(227)	3.9		

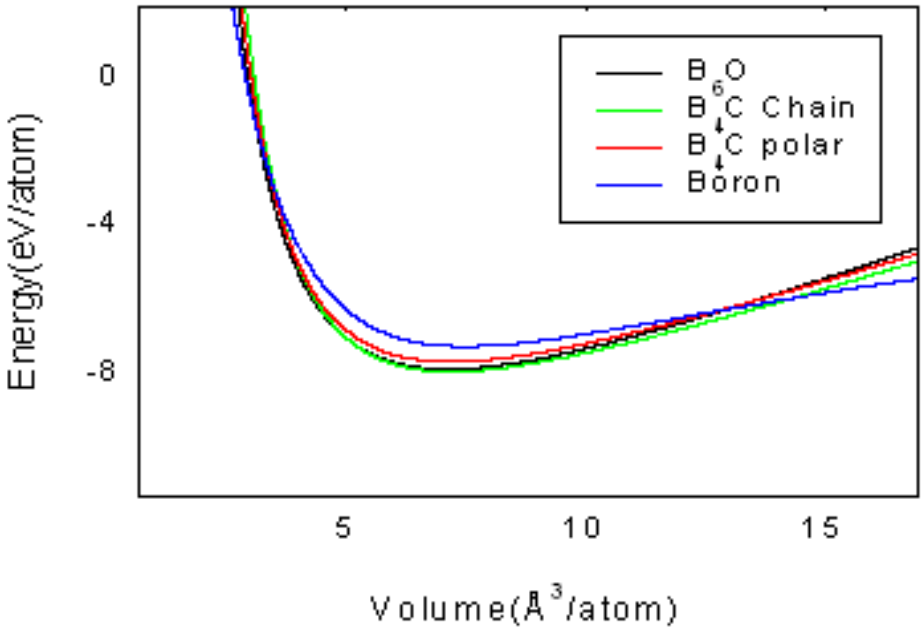


Figure 5.5: Energy vs volume for B_{50}, B_4C and B_6O

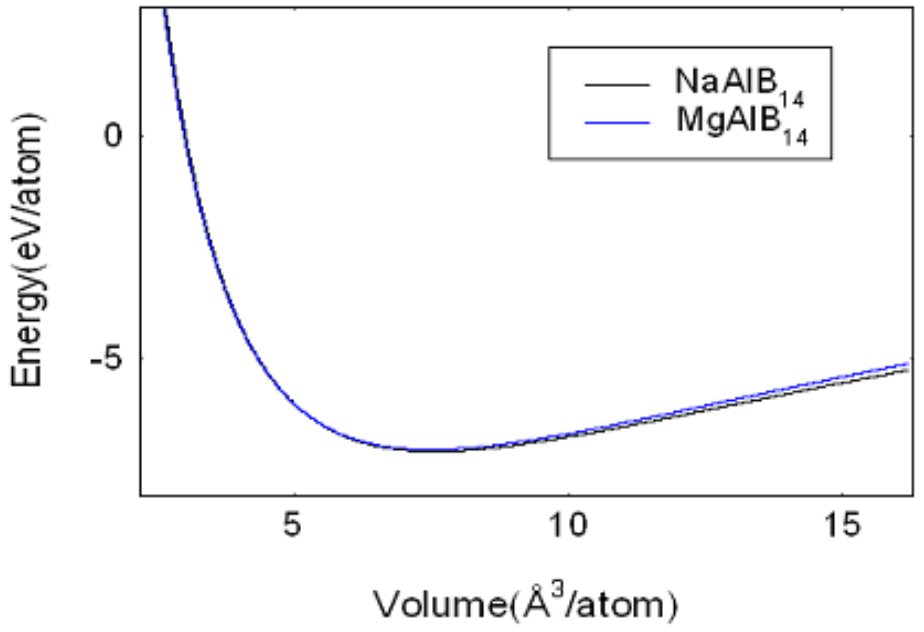


Figure 5.6: Energy vs volume of orthorhombic $NaAlB_{14}$ and $MgAlB_{14}$

5.3 Electronic Properties

In this section we want to investigate what is happening within the icosahedra and how other atoms affect the icosahedra by looking at the electron states and changes at the icosahedra. The icosahedron of boron atoms supply information needed to understand chemistry in crystal boron. In the icosahedron skeleton shown in Figure 3.1 each boron forms a covalent bond with each five nearest neighbors which occupy equivalent positions about a five fold axis. There are many other symmetry elements in addition to the six fivefold axes: ten three axes, fifteen twofold axes, fifteen mirror planes and a center of invention. It is not possible to interpret the structure in terms of the ordinary two electron-bond picture of covalency, but the stability of this unit when ideally connected into a three dimensional network of boron atoms does emerge quite clearly in a molecular orbital calculation.

With four valence orbitals: 2s, $2p_x$, $2p_y$, and $2p_z$ per boron atom this leads to forty-eight atomic orbitals which are divided into thirteen bonding, twenty-three anti-bonding and twelve orbitals perpendicular to the next icosahedra. The thirteen bonding orbitals require twenty-six electrons and the twelve orbitals pointing outward require twelve electrons. Thus each icosahedron requires a total of thirty-eight electrons for closed shell type structure, but the twelve icosahedral atoms can provide only thirty-six valence electrons. The missing two electrons have to be attracted from elsewhere, thus explaining the high affinity to carbon and stability and hardness of these boride materials. The occupied charge configuration of each atom is very close

to s^1p^2 in contrast to the free atoms s^2p^1 configuration for the calculated molecular orbitals.

5.3.1 Density of States

The electronic properties can be understood by considering the properties of a free electron gas, in which the eigenvalues E vary parabolically with the wave vector $\mathbf{k}$ as $E = (\hbar^2\mathbf{k}^2/2m)$. An important property that quantifies how closely packed energy levels are in a quantum-mechanical system is the density of states (DOS). It is a function of the internal energy E, such that the expression $\rho(E)dE$ represents the number of states with energies between E and $E + dE$ given by

$$\rho(E)dE = \frac{k^2 dk}{\pi^2} \tag{5.11}$$

$$= \frac{1}{2\pi^2}\left(\frac{2m}{\hbar^2}\right)^{\frac{3}{2}} E^{\frac{1}{2}} dE \tag{5.12}$$

DOS is used in condensed matter physics, where it refers to the electron, photon, or phonon energy levels in a crystalline solid. In a crystalline solids, there are often energy ranges where the density of electron states is zero, which means that the electrons cannot be excited to those energies. Filling up the states with electrons each following Pauli's exclusion principle, we arrive at the concept of the Fermi surface, which is spherical for a free electron gas illustrated in Figure 5.7 [137]. The corre-

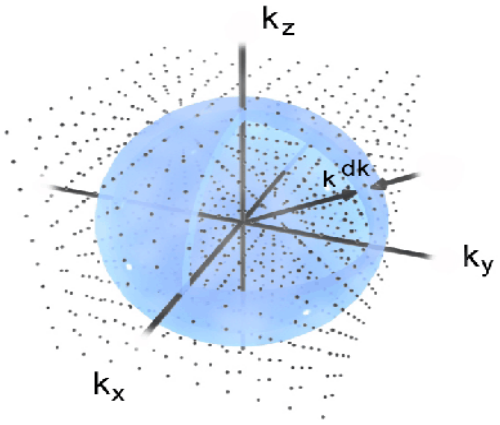


Figure 5.7: Visualization of k-space showing values of k as points. The number of allowed states is of these points contained in the shell of radius k and thickness dk.

sponding density of states of a free electron gas varies as the square root of the energy, as shown in Figure 5.8 [110].

The calculated density of states for the boride materials are shown in Figures (5.9-5.14) using VASP code within LDA. The Fermi level is taken as the zero energy. In the icosahedra boron rich solids, the basic structure can accommodate a variety of other constituents and depending on the minority constituents, these icosahedra boron rich solids range from conductive materials to insulators with wide energy gaps.

The calculated density of states of tetragonal boron B_{50} is shown in Figure 5.9. The material show that a forbidden gap occurs after the valence band has been filled with electrons in order to satisfy the internal bonding requirements within icosahedra, external bonds from the icosahedra and contribution to bonds from the isolated boron atoms in the interstitial positions. This result is metallic with the theoretical deficit

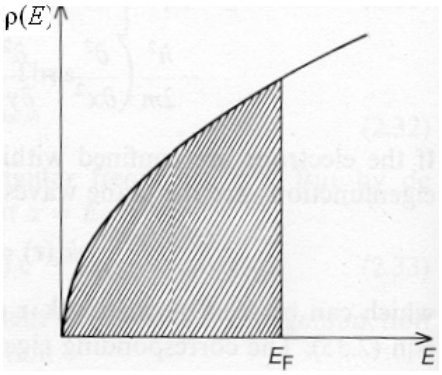


Figure 5.8: The free elecron density of states ($\rho(E)\ \alpha\ E^{\frac{1}{2}}$)

of ten electrons and the stability is usually achieved by addition of some electron rich elements such as carbon or nitrogen in the open interstitial regions as in the case of $B_{50}N_2$ or $B_{50}C_2$.

Figure(5.10) shows the DOS for B_4C polar. The material can be considered to be semiconductor with an intrinsic hole population at the top of the valence band. In this valence band there are band segments containing valence electrons from top to bottom. And hence large number of these valence electrons may be distributed in the top segment.

In the case of B_4C chain we also observe the semiconducting gap from DOS in Figure 5.11. It confirms the validity of a schematic assignment of two electrons to each bond external to the icosahedra; each of the terminal carbon atoms is tetrahedrally bonded, while the central twofold coordinated atoms of the carbon chain formally donates two electrons to the network of C-B bonds. The formal result is thus a closed shell of bonding orbitals.

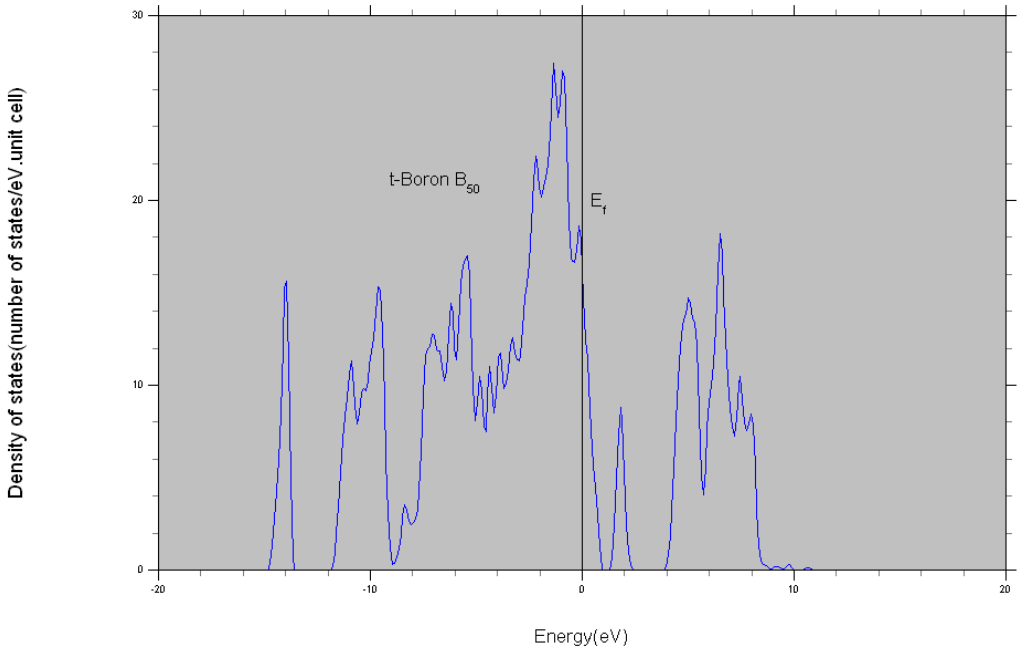


Figure 5.9: Density of states for tetragonal boron B_{50}

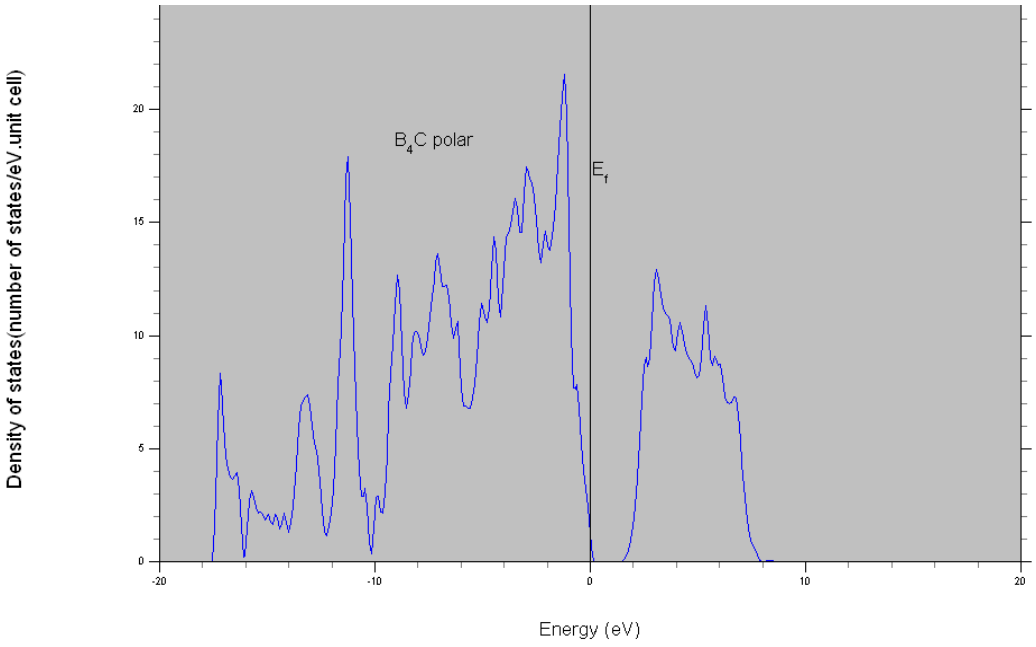


Figure 5.10: Density of states for B_4C (polar).

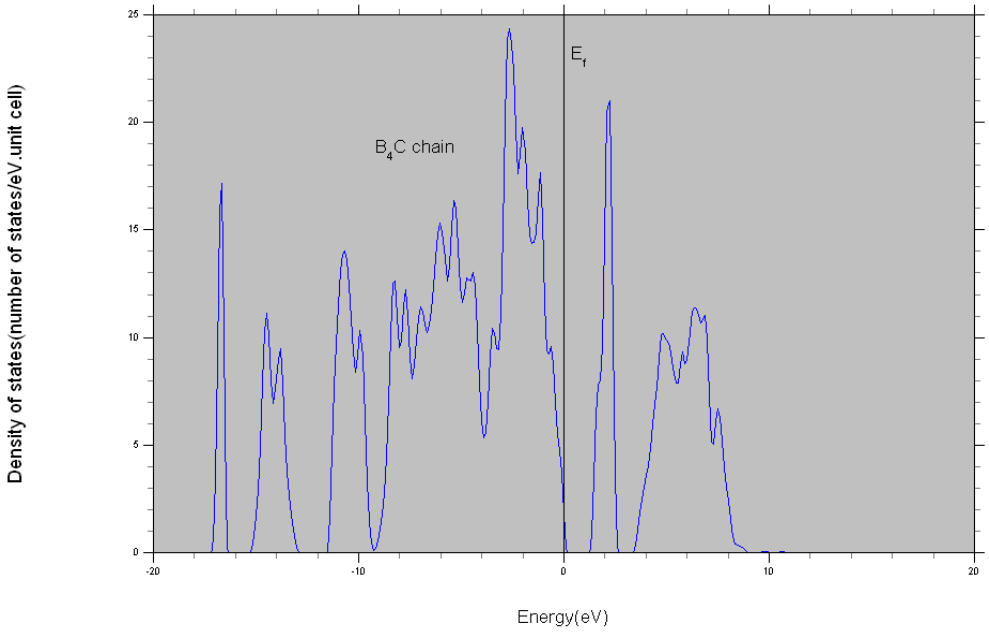


Figure 5.11: Density of states for B_4C (chain).

The calculated DOS for B_6O is shown in Figure 5.12. In B_6O we also observe a semiconducting behavior. Again there are band segments within the valence band containing the valence electrons. The peaks are somehow different to those of B_4C in Figure 5.10 and Figure 5.11 indicating different bonding which is affected by elements in the crystals. Actually the segment below the top of the valence band originates from the oxygen *sp* electrons interacting with *sp* boron electrons distributed over the other segments.

DOS for $MgAlB_{14}$ is shown in Figure 5.13. In $MgAlB_{14}$ which contains 64 atoms per unit cell and the structure show that the Fermi level lies in the states above the a band gap. Figure 5.14 shows $NaAlB_{14}$ DOS. The bands might have a predominant

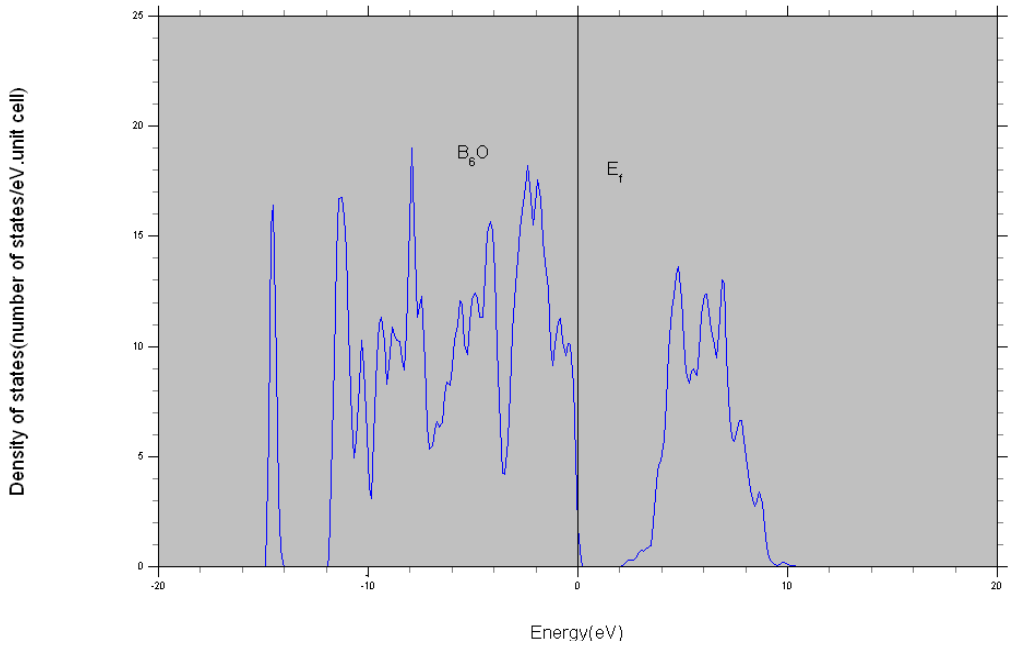


Figure 5.12: Density of states for B_6O

boron character affecting the crystals. $NaAlB_{14}$ could be a semiconductor material from this DOS calculation. It may be concluded that more than half of the valence electrons of the metal atoms are transferred to the electron deficient boron atoms framework to stabilize orthorhombic type structures.

5.3.2 Changes at the Boron Icosahedra

Charge density

It is clear from the above that the overall strength of the borides relates to extra atoms connecting to the boron icosahedra. There are several different B-B bond lengths in all systems discussed above-either connecting the B icosahedra, between B

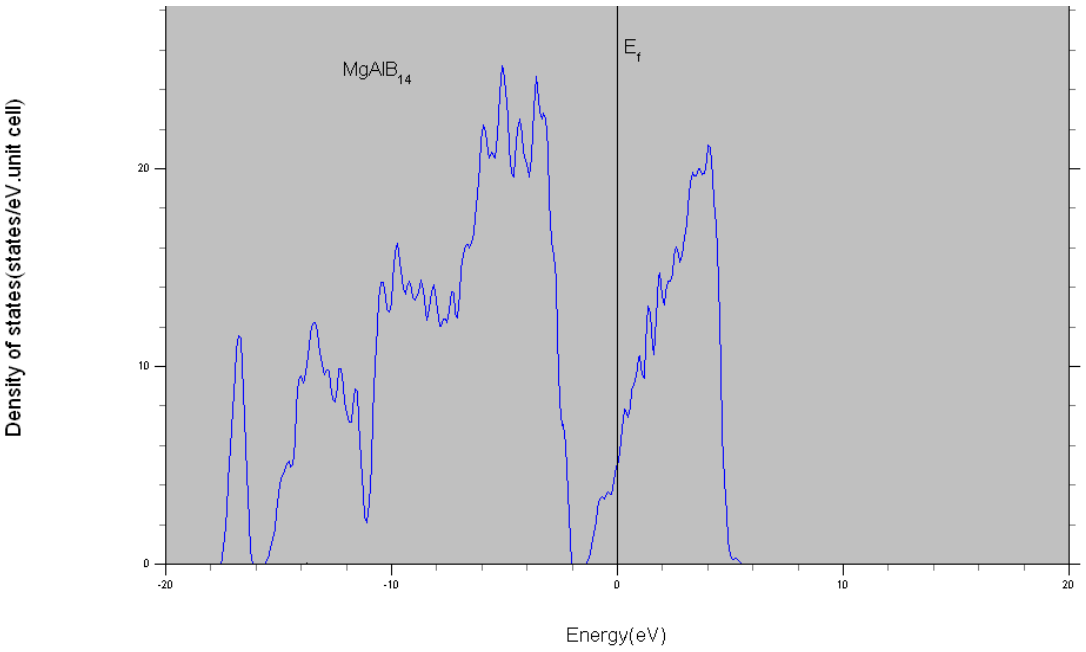


Figure 5.13: Density of states for $MgAlB_{14}$

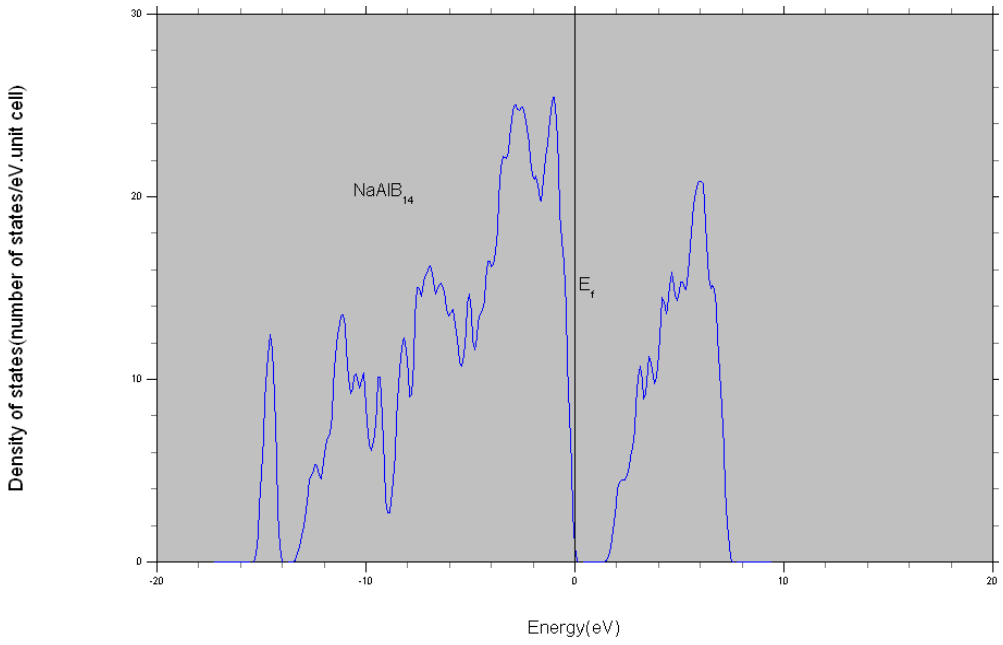


Figure 5.14: Density of states for $NaAlB_{14}$

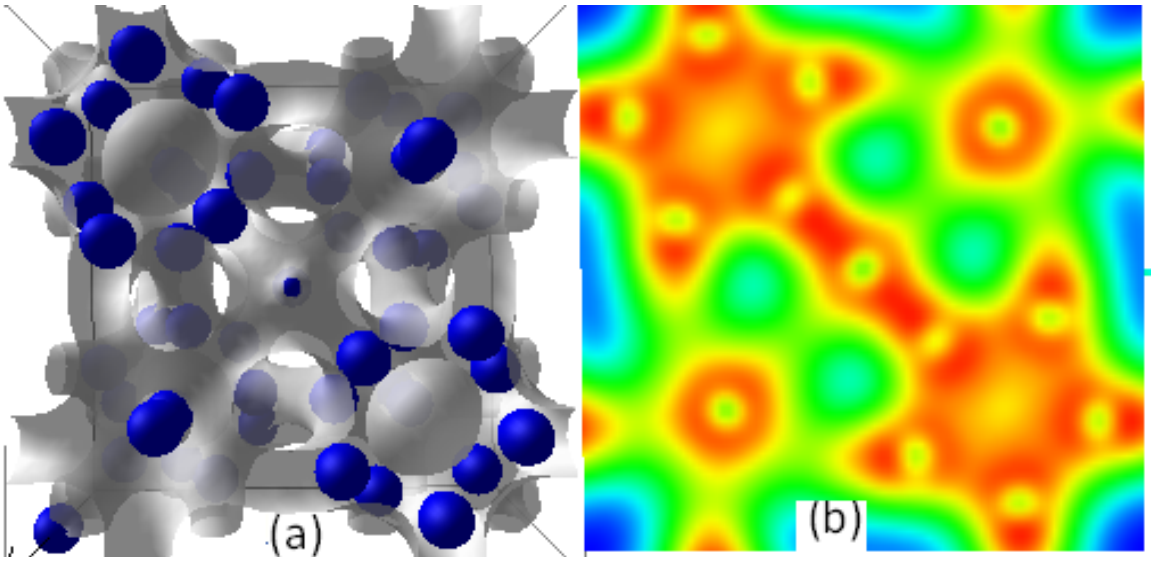


Figure 5.15: Calculated charge density of tetragonal boron. (a) Density at the iso-surface value of 200 and (b) the density slice offset of 0.44.

atoms in the icosahedra-including those B atoms connected to the other atoms such as C or O in B_4C or B_6O. The electronic charge density can give insight into the chemical bonding which is a likely prerequisite for the origin of hardness and thus possibly account for the symmetrical structures that are observed. The charge density of tetragonal boron B_{50} involving intericosahedra bonding is shown in Figure 5.15. From point of view of chemical bonding, Figure 5.15 show strong covalent bonding between intra-icosahedra boron atoms and also with isolated boron atoms. It becomes clear that the metallization of tetragonal boron is mainly due to the presence of low coordination isolated boron types atoms and also the low coordination number for intericosahedra bonding.

Figure 5.16 show the charge density for $MgAlB_{14}$ which is similar for $NaAlB_{14}$ and

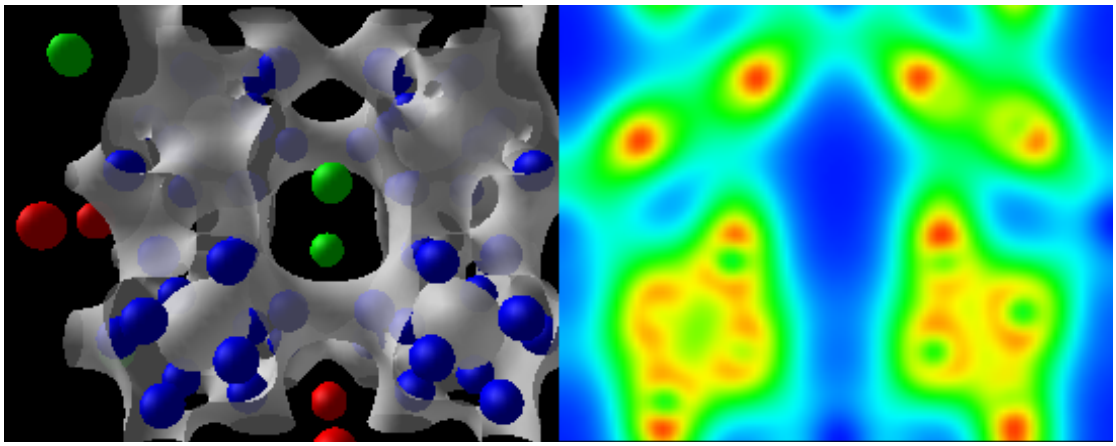


Figure 5.16: The charge density of $MgAlB_{14}$.Density (left) is at the iso surface value of 200 and the slice offset(right) of 0.44. Mg atoms are red while Al atoms are green.

related compounds. The little observation in this material is that covalent bonding is still observed in the boron icosahedra clusters while there is slight bonding between Al and boron atoms in the structure. Mg atoms seems to be not much involved in the bonding to icosahedra or Al atoms. Thus suggest that Al atoms is slightly responsible for the atomic bonding between the boron icosahedra which reveals that bonding within the icosahedra is still larger and hence the metal-boron interactions could be ionic. The icosahedra therefore contain the main component of atomic bonding. It is interesting to note that the shortest Mg-Mg distance is 3.8101Å which is a little larger than 3.21 Å that of metallic magnesium and the shortest between Al-Al atoms is 4.96Å which is far from 2.92Å of metallic aluminum.

We now look at the charge densities of rhombohedral structures for B_4C polar, B_4C chain and B_6O shown in Figures 5.17, 5.18 and 5.19. Boron itself exist in

rhombohedral lattice which maintains the $R\bar{3}m$ symmetry, B_{12} icosahedra(Figure 3.1) on each lattice site distort and lose their fivefold rotation axis. The bonds between can be divided into B_e-B_p bonds (B_{10}-B_4, B_{10}-B_3, B_5-B_4, ...) in six B_p-B_p-B_e types of triangle faces formed by one equatorial and two neighboring polar atoms. The next six B_e-B_e (B_6-B_5, B_6-B_2, B_9-B_{10}, ...) and six B_p-B_e (B_4-B_9, B_3-B_{11}, B_1-B_6, ...) bonds in 12 B_p-B_e-B_e types of triangle faces formed by one polar and two equatorial atoms. The last six B_p-B_p (B_4-B_3, B_3-B_1, B_1-B_4, ...) bonds in two polar B_p-B_p-B_p types of triangle faces formed by two top (or bottom) polar atoms. Generally compounds formed by boron with carbon,etc., that have the same space group and similar lattice constants and positional parameters, these atoms are inserted into the octahedral interstices and form chains.

From the Figures (5.17 and 5.18) we can observe that high density at the center of the icosahedra which is caused by the intracluster bonds, that is B_p-B_p-B_p, B_p-B_p-B_e and B_p-B_e-B_e bonds. It is considered that there is bending in the intercluster bond for rhombohedral $\alpha-$boron which arises from the difference between the directions of the bonds oriented outwards from p sites of the icosahedra of the B_{12} cluster and the lattice axis of the rhombohedron, which corresponds to the direction of the neighboring cluster. This difference arises because intercluster three center bonds are pulling the lattice axis. The insertion of the atomic chain along the diagonal expands the a and b axes of the hexagonal lattice. Conversely the c axes are shrunk by this insertion. On the basis of chemical bonding there are two electrons lacking in the B_{12}

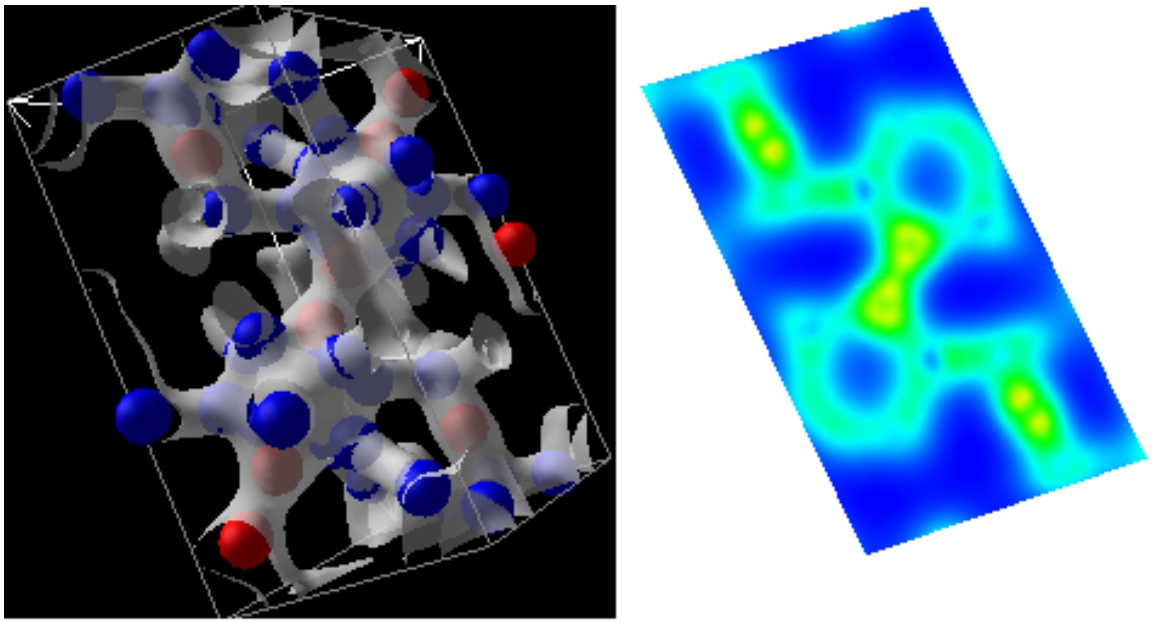


Figure 5.17: Charge density of B_4C polar. The density at iso surface value 200 (left) and the corresponding slice (right) at azimuthal angle of 342, polar angle of 97.2 and offset of 0.

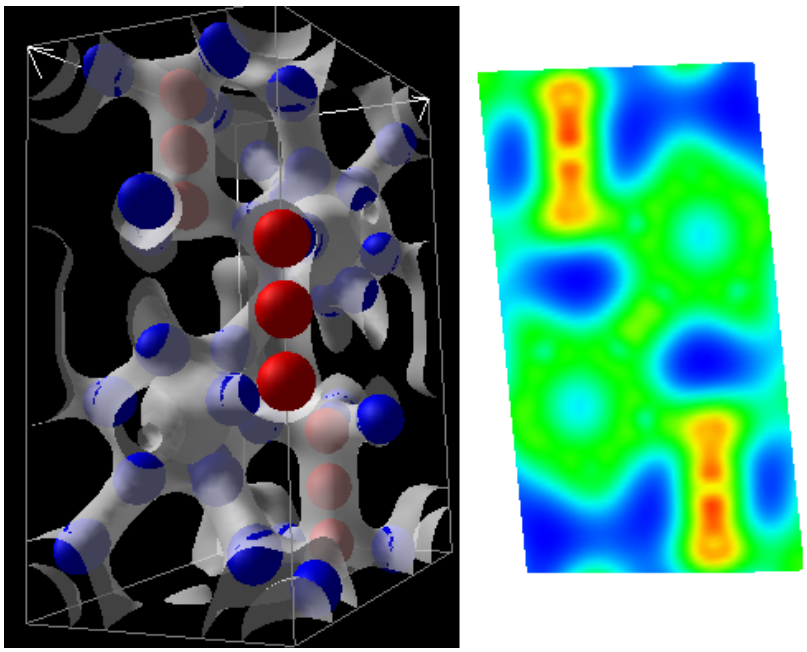


Figure 5.18: Charge density of B_4C chain.

cluster, hence the cluster can in B_4C compensate for them by replacing one of the boron atoms with a carbon atom and receiving one electron boron or carbon atom of the chain. In these materials the electronegativity does not suggest ionicity and hence we consider covalent bonds are predominant in this rigid frameworks of boron carbide which is one of the hardest boron rich solid.

Figure (5.19) shows the charge density of B_6O. In B_6O which is also the hardest of the borides established we also observe high density in the icosahedra. In Figure (5.20) we show a typical contour plot for B_6O; for this clearly shows that the bonding about the oxygen atoms is very localized with no covalent bonding between O atoms which is consistent with earlier calculations[65]. This feature is also quite with similar

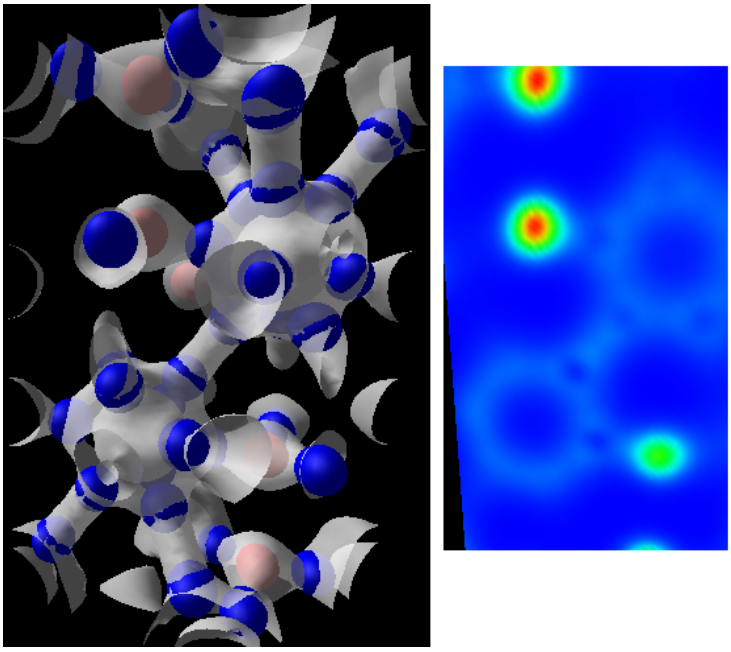


Figure 5.19: Charge density of B_6O

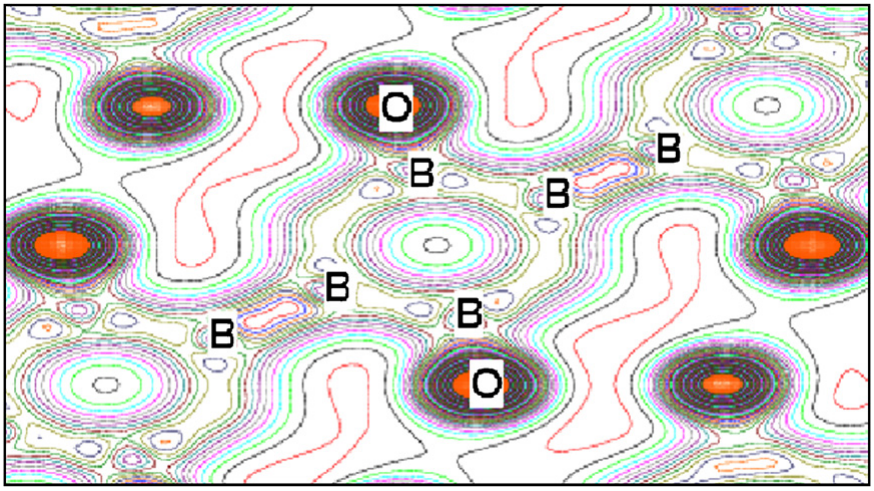


Figure 5.20: Charge density contour plot in super-hard B_6O. Bonding of O to the B icosahedra is visible as is the B-B bond between the B icosahedra. There is no covalent bonding between the O atoms.

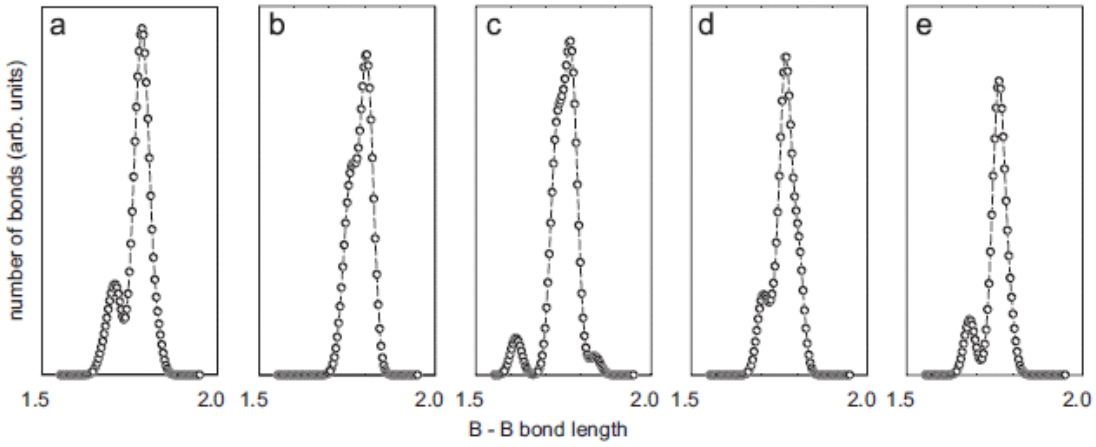


Figure 5.21: Distribution of B-B bond lengths in (a) tetragonal boron, (b) $MgAlB_{14}$, (c) MgC_2B_{14},(d) B_4C and B_6O. The smaller bonds lengths are usually associated with intericasahehral bonding

to the other structures as found from earlier work[56] where the additional atoms to the B enter into no direct covalent bonding with the boron icosahedra structures and often no bonding with each other.

Boron-boron bonds

There are many B-B bonds in a typical unit cell of the borides and so each bond will have its own distinct character. To illustrate this point in Figure (5.21) we show a (Gaussian) distribution of the B-B bond lengths of the structures considered above. The arithmetic average value of the calculated bond lengths is also given in Table 5.4. As seen from Table 5.4, for all the materials bond lengths lie between 1.75 to 1.80Å which is quite a small variation.

Some quantitative measurement is needed to understand the overall bonding in

Table 5.4: Number of B-B bonds and average bond length(Å) and charges

Material	**No Bonds**	**Average Bond length**	**Average Charge** $\times 10^{-2}$	**Knoop Hardness(GPa)**
Boron	106	1.770 (1.793)	5.832 (5.197)	
$NaAlB_{14}$	111	1.789 (1.809)	5.932 (5.342)	23-28[59]
$MgAlB_{14}$	134	1.792 (1.792)	6.088 (5.556)	30-46[24]
MgC_2B_{14}	75	1749 (1.770)	6.110 (5.480)	26-34 [26]
B_4C polar	56	1.751 (1.773)	5.981 (5.267)	41[35], 27-30[26]
B_4C chain	46	1.764 (1.786)	5.964 (5.347)	
B_6O	47	1.753 (1.776)	6.177 (5.485)	45[136]

these systems. One way to measure the extent of the bonding is from the charge distribution along a line connecting two adjacent B atoms. This can be obtained computationally by projecting the charge density along n points joining adjacent B atoms. An (arithmetic) average of the calculated charge density is then defined as

$$\overline{\rho} = \frac{\sum_{i=1,n} \rho(r_i)}{n}.$$

In the present calculation $n = 100$ points were used although larger values were also employed to test convergence in the value of $\overline{\rho}$.

Figure 5.22 show the bond charge density between adjacent B atoms for several structures considered here. There are substantial differences corresponding to the relaxation induced in B icosahedra due to the additional chemical atoms connecting

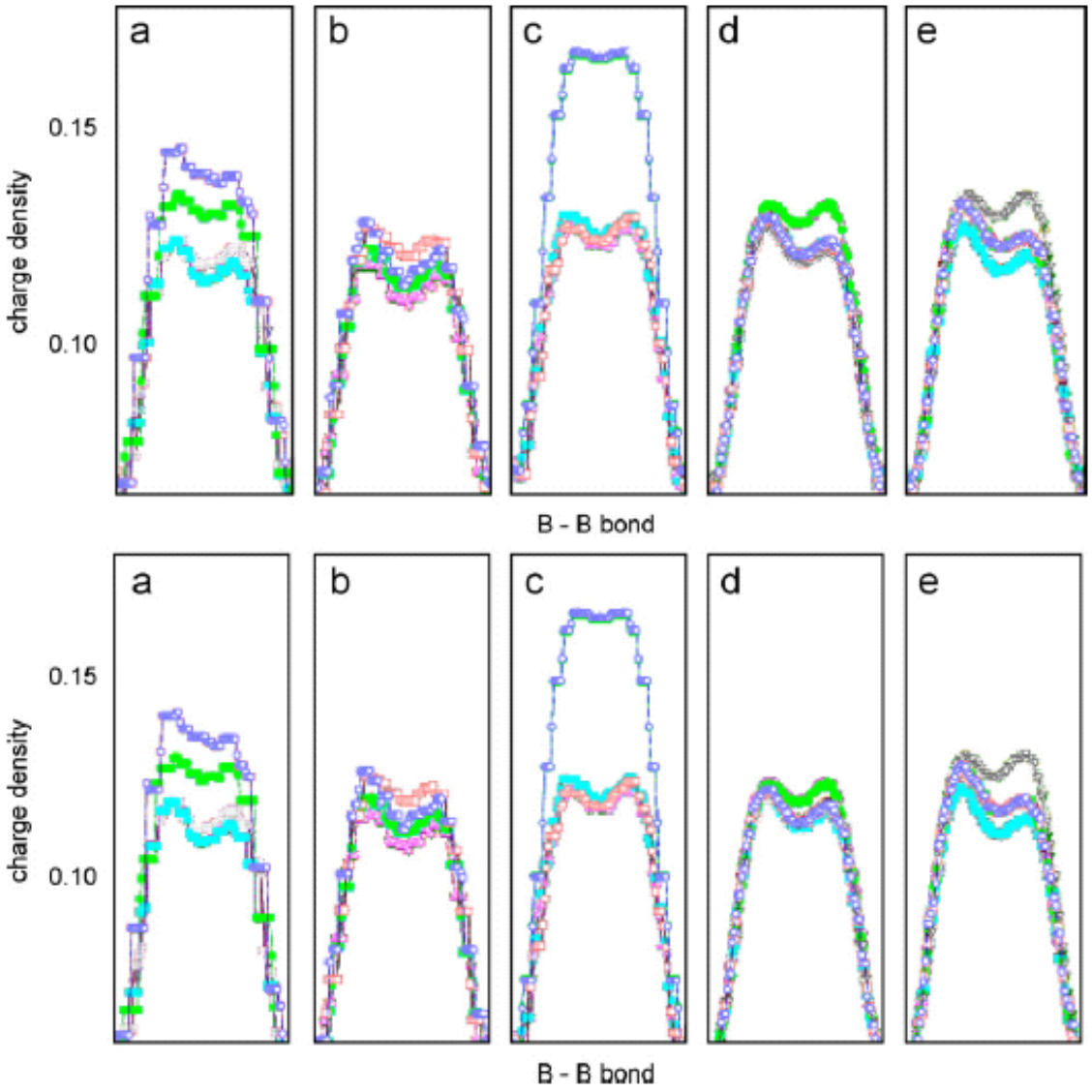


Figure 5.22: Charge density (LDA, top: GGA, bottom) across B-B bonds in (a) tetragonal boron, (b) $MgAlB_{14}$, (c) MgC_2B_{14}, (d) B_4C and (e) B_6O

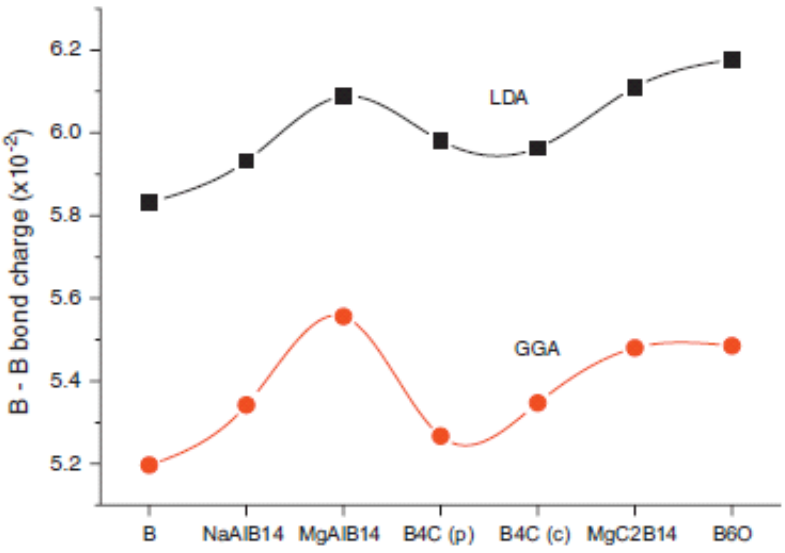


Figure 5.23: Trend in B-B average bond charge.

icosahedra. Obviously the shorter bond length will have larger densities-but as shown from Figure 5.22 there is usually a low number of these. The significant point is that the large differences in B-B bonding in each material is established. To quantify the differences we now give the values of the average charge density $\overline{\rho}$ in Table 5.4 and with variation displayed in Figure 5.23.

This variation follows a similar trend as the bulk modulus and equilibrium volume. However, an increase in $MgAlB_{14}$ is suggested that did not follow the trend in equilibrium volume and bulk modulus. This we attribute to the icosahedra relaxation induced by the additional metal ions. As noted in Figure 5.22b for this material the number of shorter bond lengths is larger than for other materials suggesting that here the intericosahedral charge density is being influenced more than with the other

materials. Simultaneously we also note that in B_6O the average charge distribution is the largest of all the structures considered here. There is no bonding between the O atoms, accordingly the change on the B-B bonds must be attributed to the additional electronic effect of the O.

5.4 B_4N, B_6N and B_6C

The purpose of this work is the search for new ultra-hard materials using computational method discussed in Chapter 4. We further predicted properties of new compounds which are likely to have the superhard property and this interesting materials with rhombohedral structures space group as that of boron carbide and boron suboxide are B_4N, B_6N and B_6C. Well the indications for existence of B_6N [138] were reported as early as 1976 with the composition similar to B_6O. Although they did not dwell on the material, Garvie [139] synthesized the material from high temperatures experiment and also found an extensive solution between B_4C and B_6O as well as nanorods with composition near B_6C.

We calculated properties of these interesting materials using same techniques as explained above and we found them to have high bulk modulus and possibly high hardness. Table 5.5 shows lattice parameters and they compares well with experiment. Figure 5.24 shows the energy vs volume while the equilibrium properties are presented in Table 5.6.

There is some trends in the lattice parameter ratio and the bulk modulus and

Table 5.5: No atoms and calculated lattice parameters

Material	**No Atoms**	**LDA (Å)**	**GGA** (Å)	[a]**Experiment** (Å)
B_4N	45	a = 5.412 c = 12.260	a = 5.482 c = 12.397	a = 5.682 c = 12.117
B_6N	42	a = 5.404 c =12.114	a = 5.444 [b](5.075) c = 12.234	a = 5.457 c = 12.241
B_6C	42	a = 5.497 c = 12.062	a = 5.558 c = 12.239	a = 5.582 c =12.135

[a]Ref **[140]**
[b]Ref [135]

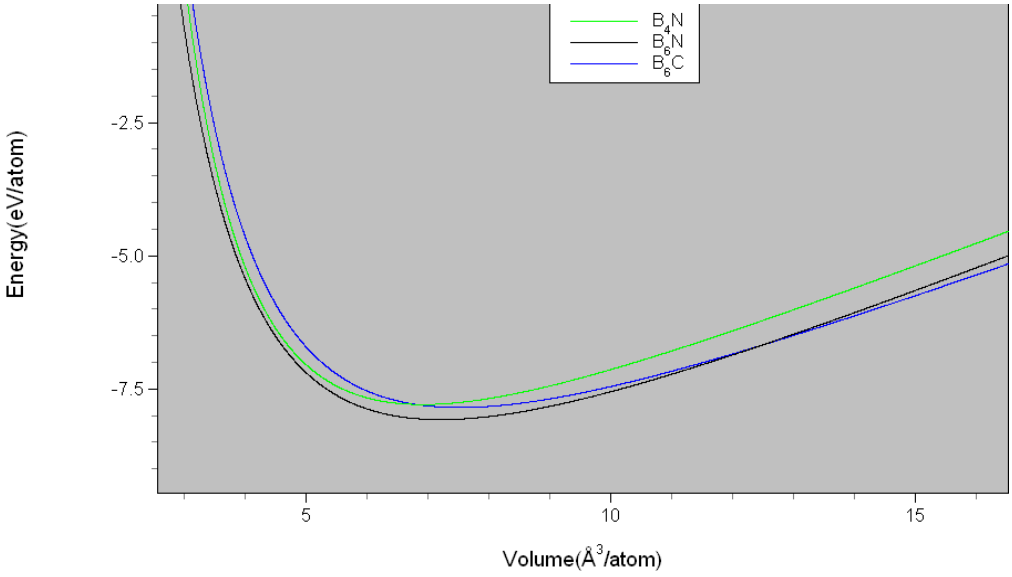


Figure 5.24: Energy vs volume of B_4N, B_6N and B_6C

Table 5.6: Equilibrium properties. Calculated GGA values in brackets

Material	**Energy (eV/atom)**	**Volume (Å/atom)**	**Bulk Modulus (GPa)**	B'
B_4N	-7.792	6.913	265{259[141]}	3.710
	(-6.934)	(7.179)	(242){(241)[141]}	(3.310)
B_6N	-8.075	7.205	243	3.265
	(-7.253)	(7.476)	(229){(236)[135]}	(3.320)
B_6C	-7.847	7.519	231	3.382
	(-7.061)	(7.799)	(216)	(3.430)

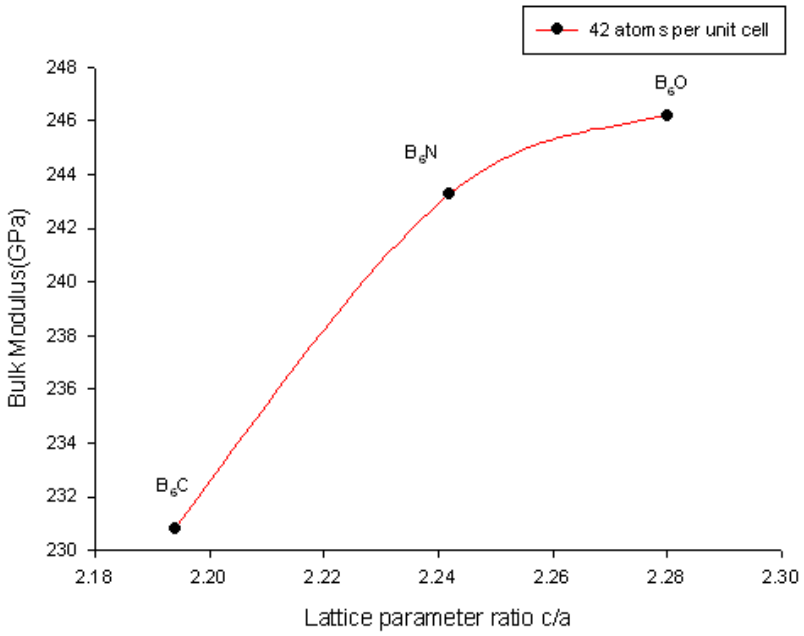


Figure 5.25: Bulk modulus vs c/a ratio

is shown in Figure 5.25. It is interesting to note that this trend is in line with atomic volume, electronegativity, of the additional elements in this composition of B_6X (X=C,N,O). Further investigations into elastic, electronic and even transport properties of these materials would be of utmost importance in understanding the behavior that these boron-rich solids might show under extreme conditions.

Chapter 6

Large Scale Computer Modelling Techniques

This chapter we concentrate on computer modelling techniques which have been used to simulate large numbers of atoms. The aim of computer simulation methods is to predict the properties of a system from the potential model. *Ab-initio* methods can quite accurately predict many properties but they have limitations of handling large number of atoms and therefore simulation techniques are of great importance if we are not interested in the electronic structure. They are used to model large number of atoms, up to more than 100 000 atoms. The methods are now an established tools in physical and biological sciences to topics ranging from liquid structure to protein conformation. One of the motivation for computer simulations of physical systems is that we also eliminates approximations. The computer simulation approach

allows one to study complex systems and gain insight into the behavior. Indeed, the complexity can go far beyond the reach of analytical methods.

6.1 Statistical Mechanics

Computer simulation generates the information at the microscopic level (atomic and molecular positions, velocities etc.) and the conversion of this very detailed information into macroscopic terms (pressure, internal energy etc.) is the province of statistical mechanics [142, 31, 143, 30]. Solving the trajectories of number of atoms (N) is of no use if use we cannot extract experimentally meaningful properties. Most useful properties are averages of some kind so statistical methods are natural tools. Individual events in a trajectory may not be significant, however interesting. Therefore we need statistical methods to determine their relevance. The questions that one can ask is how can we relate molecular properties to system properties and most of what's interesting assumes equilibrated (or steady state) systems then how can we tell we are in equilibrium?

The average properties of a system are obtained by observing the system at a given state point for a long time and averaging an observed property over time. In Boltzmann averaging configurations must be casually connected via equation of motion but if separated by a sufficient time interval they will become statistically independent. In Gibbs averaging configurations cannot be casually connected because they are independent, so they must be statistically independent. Boltzmann average

is given by

$$\overline{A} = \frac{1}{t \to \infty} \int_0^t A(t)dt \tag{6.1}$$

$$\approx \frac{1}{t_\infty} \sum_{n=1}^{N_t} A_n \triangle t \tag{6.2}$$

where

$$\triangle t = \frac{t_\infty}{N_t} \tag{6.3}$$

We note that this implies that instantaneous value of $A(t)$ fluctuate about the mean value. The mean square fluctuation is defined as

$$\overline{\delta} A^2 = \frac{1}{t \to \infty} \int_0^t (A(t) - \overline{A})^2 dt \tag{6.4}$$

$$= \frac{1}{t_\infty} \sum_{n=1}^{N_t} (A_n - \overline{A})^2 \triangle t$$

The observation from Gibbs averaging is that many replicas of the system all normally at the same state point and average the instantaneous values of the observed variables. Ensemble average is given by

$$\langle A \rangle = \frac{1}{N_\infty} \sum_{n=1}^{N_\infty} A_n \tag{6.5}$$

Fluctuation is necessarily a property of the Gibbs ensemble also:

$$\langle \delta A \rangle = \left\langle \left(A - \langle A \rangle^2 \right) \right\rangle \tag{6.6}$$

$$= \frac{1}{N_\infty} \sum_{n=1}^{N_\infty} \left(A_n - \langle A \rangle^2 \right) \tag{6.7}$$

The averages obtained by the Boltzmann and Gibbs averaging process will be the same on the condition that enough samples are taken. The simple properties of averages are constant of equilibrium systems. Statistical errors in simulations are averages computed by simulation and are expected deviations from the true ensemble averages. Simulation average:

$$\overline{A} = \frac{1}{N} \sum_{i=1}^{N} A_i \tag{6.8}$$

Ensemble average:

$$\left\langle \overline{A} \right\rangle = \frac{1}{N} \sum_{i=1}^{N} \langle A_i \rangle \tag{6.9}$$

Variance:

$$\delta^2 = \left\langle \overline{A}^2 \right\rangle - \left\langle \overline{A} \right\rangle^2 \tag{6.10}$$

Standard error of the mean:

$$\delta A = \pm\delta \tag{6.11}$$

In practice we calculate from finite sample of microstates obtained by one or two methods. Stochastic (Gibbs averaging) method is used in Monte Carlo and deterministic (Boltzmann averaging) method is used in molecular dynamics.

6.2 Molecular Dynamics Simulation

Molecular dynamics (MD) is the solution of classical equation of motion for atoms and molecules to obtain the time evolution of the system [144, 145, 146, 30, 142, 147]. It is applied to many particle systems where general analytical solution is not possible and one must resort to numerical methods and computers. The averaging process used for thermodynamic properties is usually the Maxwell-Boltzmann time averaging. In MD the most fundamental form for atomic systems is the Lagrangian equation of motion

$$\frac{d}{dt}\left(\frac{\partial \mathcal{L}}{\partial \dot{q}_k}\right) = \frac{\partial \mathcal{L}}{\partial q_k} \tag{6.12}$$

where the Lagrangian function $\mathcal{L}(q, \dot{q})$ is defined in terms of kinetic (K) and

potential energies (V) such that

$$\mathcal{L} = K + V \tag{6.13}$$

is considered to be function of the generalized coordinates q_k and their time derivatives $\dot{q}_k$. If we consider a system of atoms, with Cartesian coordinates $\mathbf{r}_i$ and the usual definitions of K and V then

$$m_i \ddot{\mathbf{r}}_i = \overrightarrow{F}_i \tag{6.14}$$

where m_i is the mass of atom i and

$$\overrightarrow{F} = \sum_{j \neq i}^{N} \overrightarrow{f}_{ij} \tag{6.15}$$

$$\begin{aligned} \overrightarrow{f}_{ij} &= \overrightarrow{\nabla}_i \mathcal{L} & (6.16) \\ &= -\nabla_i V(r_{ij}) & (6.17) \end{aligned}$$

is the force on that atom. These equations also apply to the center of mass of a molecule, with $\overrightarrow{f}_{ij}$ representing the total force on molecule i. In general, the system

will be described by the Hamiltonian

$$H = \frac{1}{2}\sum_i \frac{p_i^2}{m_i} + \sum_{i \neq j} u\left(r_{ij}\right) \tag{6.18}$$

Since we restrict ourself to properties of the bulk at a specific density we must introduce volume, the MD cell to retain constant density. If the system is in thermal equilibrium the shape is irrelevant . This is true for gases and liquids in the limit where the volume is large enough. For systems in a crystalline state the shape does make difference. The finiteness of the system size is felt through the presence of the boundary. The conversion adopted in the vast majority of molecular simulation is to use the periodic boundary condition as it is assume that for these boundary conditions the behavior of the system is most similar to that of a system of the same size embedded in an infinite system. In this way the number of particles within the base cell is always conserved. Computational implementation is that if a particle crosses a surface of a basic cell is automatically replaced by a particle entering well with unchanged velocity [148]. To compute the potential pair energy of the force between two particles i and j one arguments the periodic boundary condition by the so-called nearest image conversion. In practice this means simply that when calculating $u(r_{ij})$ or similar we use the quantity $\triangle r_{ij} - L$ in place of $\triangle r_{ij}$. An analogous rule holds for $\triangle r_{ij} \leq -L/2$ and for the other coordinates. From a numerical mathematics point of view the MD is an initial value problem. A host of algorithms have been developed

for this problem, which are, however not all applicable in the context of physical problems. Given the molecular positions, velocities and other dynamic information at time t, we attempt to obtain the positions, velocities, etc. at later time $t + \delta t$, to a sufficient degree of accuracy. The equation are solved on a step by step basis; the choice of the time interval will depend somewhat on the method of solution, but δt will be significantly smaller than the typical time taken for a molecule to travel its own length.

The algorithm of standard MD simulation for studying system in equilibrium is: initialize; start simulation and let the system reach equilibrium and finally continue with the simulation and store results. Verlet algorithm is the numerical algorithm which is simple reliable at the same time is widely used in MD. The standard form of the Verlet algorithm [143] for the integration of equation of motion of a particle subject to a force $\overrightarrow{F}$ depending only on the positions of the particle reads

$$\overrightarrow{r}(t + \delta t) = 2\overrightarrow{r}(t) - \overrightarrow{r}(t - \delta t) + \delta t^2 \overrightarrow{F}[\overrightarrow{r}(t)]/m. \tag{6.19}$$

The velocities are not needed to compute the trajectories, but they can be calculated as

$$\overrightarrow{v}(t) = \frac{\overrightarrow{r}(t + \delta t) - \overrightarrow{r}(t - \delta t)}{2\delta t}. \tag{6.20}$$

There exist two alternative formulation of the Verlet, which are exactly equivalent

to it in an exact arithmetic but which are less susceptible to errors resulting from finite numerical precision in the computer than the original. Leap-frog form introduces the velocities at time step precisely in between those at which the position are evaluated:

$$\overrightarrow{v}(t+\frac{1}{2}\delta t) = \overrightarrow{v}(t-\frac{1}{2}\delta t) + \delta t\overrightarrow{a}(t) \tag{6.21}$$

$$\overrightarrow{r}(t+\delta t) = \overrightarrow{r}(t) + \delta t\overrightarrow{v}(t+\frac{1}{2}\delta t) \tag{6.22}$$

where the first equation must be used before the second, as the latter uses the result $\overrightarrow{v}(t+\frac{1}{2}\delta t)$ obtained in the first equation. Another form is velocity-Verlet algorithm which is also more stable that the original Verlet and which via the definition evaluates velocities and positions at the same time instances:

$$\overrightarrow{r}(t+\delta t) = \overrightarrow{r}(t) + \delta t\overrightarrow{v}(t) + \frac{1}{2}\delta t^2\overrightarrow{a}(t) \tag{6.23}$$

$$\overrightarrow{v}(t+\delta t) = \overrightarrow{v}(t) + \frac{1}{2}\delta t[\overrightarrow{a}(t) + \overrightarrow{a}(t+\delta t)]. \tag{6.24}$$

This form is most convenient because it is very stable with respect to errors due to finite precision arithmetic and it does not require additional calculation in order to find velocities. It should be noted that all formulations have the same memory requirements.

Different ensembles are used when performing MD simulations. The microcanonical and canonical ensembles are used for testing the time step of the simulation in the calculation by measuring the conversation of energy. In the microcanonical or NVE ensemble, the number of particles, volume and total energy are kept constant. In the canonical ensemble or NVT quantities which are kept constant are number of particles, volume and temperature. The NPT or isobaric-isobaric ensemble, the number of particles, pressure and the temperature are constant. Simulations are real computer experiments and they interpret things the way we want to do them.

6.3 Calculation of Physical Properties from MD

The molecular dynamics studies provide structural and thermodynamic properties of systems such as radial distribution functions (RDFs), mean square displacement (MSD), diffusion coefficient, specific heat and thermal expansions by solving trajectories of atoms[149]. The quantities obtained from simulation are essential in interpreting the solid and liquid phases and about the melting phenomenon, meaning the temperatures of the solid-liquid transition. The interpreted temperatures are not the real melting temperatures of the systems, but rather the temperatures of the mechanical instability of the infinite single crystal [150].

The RDF is defined as the probability of finding an atom at a distance r from another atom compared to a homogeneous distribution [30] and is given by

$$g(r) = \frac{V}{N_1 N_2} \frac{1}{4\pi r^2 \delta r} \left\langle \sum_i \sum_{j>i} \delta(r - r_{ij} \right\rangle \tag{6.25}$$

where V is the volume, N_1 and N_2 are the atom types of the RDF. The delta function must give rise to a value of one for a range of r(δr). The RDF tends to 1 at long distances with sharp peaks indicating a regular lattice structure. For amorphous or liquid systems the RDF shows characteristically a small number of broad peaks at short distance, indicating short range order, superimposed on an oscillating trace to 1, which indicates a loss of long range order [30].

RDFs give the probability of finding the center of a particle or atom at a given distance from the center of another particle (Figure.6.1). The light atom at the center is the reference atom, and the circles around it represent the other atoms. A ring centered on the reference is drawn with radius r and thickness dr The radial distribution function can be an effective way of describing the structure of a system at different temperatures.

Differentiation between a solid and a liquid can be made using the RDFs by the number of peaks appearing in a particular RDF plot. In a crystal or solid, the radial distribution functions have a multiple number of sharp peaks and heights are characteristic of the lattice structure. The radial distribution function of a liquid has a small number of peaks at short distances and the height of the peaks decreases. For the crystalline solid, the peaks are sharp and thin and show long-range order. In case of a liquid phase, the peaks are broad and the radial distribution function rapidly

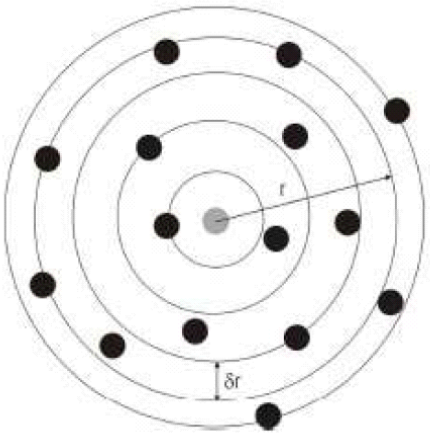


Figure 6.1: Schematic representation of radial distribution function.

converges to one.

The diffusion coefficient is another measure to estimate the relative nobilities of individual atoms. It is known that diffusion coefficient can be estimated from the slope of MSD plots using the Einstein relation as follows:

$$D = \frac{1}{6}\frac{d}{dt} < |r_i(t) - r_i(0)| > \tag{6.26}$$

or from the integral of the velocity autocorrelation function

$$D = \frac{1}{3}\int_0^\infty < v_i(t)v_i(0) > dt \tag{6.27}$$

The melting point of the simulated system can be located by increasing the temperature of a crystalline system until diffusion appears.

6.4 Non Equilibrium Molecular Dynamics

The large statistical uncertainties that are inherent in efforts to calculate the collective transport coefficients (shear viscosity, thermal conductivity, etc.) by conventional, equilibrium methods have led to search for computationally more efficient, non equilibrium schemes [151, 152, 144, 153]. There are, however, other reasons to attempt the simulation of system out of equilibrium. Non equilibrium simulations are of help in pining down the range of validity of the assumptions that underline most theoretical descriptions of transport phenomena. They can be used, in particular, to improve our understanding of the way in which a microscopic system approaches equilibrium, to confirm the microscopic validity of the linear laws that govern the diffusion of mass, momentum or energy and to determine the limits of linear regime and the corrections to the linear relations between the fluxes and thermodynamics forces from which the fluxes arise.

6.5 Potentials

We bother ourself with potentials because of we are interested in the generic problems of the evolution of class of systems and to establish trends in behaviors over a wide range of systems. We are also interested in long time scales and /or length scales and the problem does not critically depend on the changes in electronic structure. This means we use potentials because we are not interested in the electronic properties.

Potentials are algorithms to generate energy surfaces. In that sense it is always possible to tackle ground state (and many excited state) problems in terms of potentials. It may not always be sensible, the point is that they often contain (usually implicitly) a number of physical approximations. They are related to models of system behavior and they can be generic to class or specific for a material. The terms in the potential should reflect the physics of the system and be kept as simple as possible but complicated as it needs to be.

Computability, accuracy, precision and transferability are the basic questions to ask about the potential. That is, how expensive is it to calculate energies, forces, Hessians using the potential, how many decimal points ought to believe, how many decimal points one can reliably reproduce and is it possible to obtain sensible results over a range of systems, phases or configurations?

Potential may be given as

$$U = \sum_i V_i(\overrightarrow{r}_i) + \frac{1}{2!}\sum_{i<j} V_2(\overrightarrow{r}_i, \overrightarrow{r}_j) + \frac{1}{3!}\sum_{i<j<k} V_3(\overrightarrow{r}_i, \overrightarrow{r}_j, \overrightarrow{r}_k,) \tag{6.28}$$

Basic features of the potential is that there is no formal derivation but it gives a useful classification of terms such as *self energy terms* (hybridization; ion compression), *pair potentials terms* (Pauli repulsion, Coulomb, Van der Waals), *three body terms* (angle dependent forces), *four body terms* (torsional effects) and *many body terms* (metallic cohesion; directional (covalent) bonding) [154, 155, 110]. Most potentials come from literature, fitting to experimental data, fitting to quantum cal-

culations of structures or direct calculation of each term in the potential.

In covalent systems bond order can be used. There are still based on the moment approximation of tight- binding theory but include directional effects as well as coordination effects

$$V_{ij}(r) = f_C(r)(V_R(r_{ij})I_{ij}V_A(r_{ij})) \tag{6.29}$$

where $f_C(r)$ is a cutoff, V_R is the pair repulsive potential and V_A is the attractive term. I_{ij} contains the bond-order effects. This is highly complex function of local interatomic distances and angles. Potential cutoffs are part of the model and should always be quoted. Few potentials decay to zero at a convenient length scale. How they are ignored beyond a given distance (and what distance is) is important since it is part of the definition of the potential function. Simplest to ignore the potential beyond a set distance. This can give strange give strange behavior in the dynamics if forces at the step are large enough to contribute significantly. Many examples use smoothing function to take the potential to zero over a short distance. A simple one is

$$f_C(r_{ij}) = \begin{cases} 1 & r_{ij} < R - D \\ \frac{1}{2} \quad -\frac{1}{2}\sin\left[\frac{\pi}{2}\frac{r_{ij}-R}{D}\right] & R - D < r_{ij} < R + D \\ 0 & r > R + D \end{cases} \tag{6.30}$$

Most models reflect the physics and parameters make physical sense which also includes the chosen cutoff. Many potentials have been used by lot of people on variety

of systems. In general potentials needs to be checked and tested for the system before they can be used. Simulations behaviors show the anomalies that depend on potential are sometimes sensitive to particular details of potentials.

6.6 Introduction to Tersoff Potentials

The Tersoff potential [156, 157, 158, 159], which is one of the commonly used functional forms for modeling the interatomic interaction covalent systems, is used in the present work to simulate the properties of boron icosahedral structures. The functional form of Tersoff potential is given by

$$V = \sum_i v_i = \frac{1}{2} \sum_{i \neq j} v_{ij}, \tag{6.31}$$

$$v_{ij} = f_C(r_{ij})[f_R(r_{ij}) b_{ij} f_A(r_{ij})].$$

where V is the total potential energy of the system. f_A and f_R are repulsive and attractive pair potentials, respectively and f_C is a cutoff function given by

$$f_R(r_{ij}) = A_{ij}(r_{ij}) e^{(-\lambda_{ij} r_{ij})} \tag{6.32}$$

$$f_A(r_{ij}) = -B_{ij}(r_{ij}) e^{(-\lambda_{ij} r_{ij})}$$

$$f_C(r_{ij}) = \begin{cases} 1 & r_{ij} < R - D \\ \frac{1}{2} & -\frac{1}{2}\sin\left[\frac{\pi}{2}\frac{r_{ij}-R}{D}\right] \qquad R - D < r_{ij} < R + D \\ 0 & r > R + D \end{cases} \tag{6.33}$$

where r_{ij} is the bond distance between atoms i and j, D is the cutoff radius, R is the inner cutoff radius and $\lambda_{ij} = \lambda$ and $\mu_{ij} = \mu$ are potential parameters. The strength of each bond depends upon the local environment. It is lowered when the number of neighbors is relatively high. b_{ij} has the form

$$b_{ij} = \chi_{ij}(1 + \beta_i^{n_i}\zeta_{ij}^{n_j})^{-1/2} \tag{6.34}$$

$$\zeta_{ij} = \sum_{k \neq i,j} f_C(r_{ik})\omega_{ik}g(\theta_{ijk}) \tag{6.35}$$

$$g(\theta_{ijk}) = 1 + \frac{c_i^2}{d_i^2} - \frac{c_i^2}{d_i^2 + [h_i - \cos(\theta_{ijk})]^2} \tag{6.36}$$

$$\lambda_{ij} = \frac{\lambda_i + \lambda_j}{2}, \tag{6.37}$$

$$\mu_{ij} = \frac{\mu_i + \mu_j}{2} \tag{6.38}$$

$$A_{ij} = (A_i A_j)^{1/2} \tag{6.39}$$

$$B_{ij} = (B_i B_j)^{1/2} \tag{6.40}$$

which can diminish the attractive force relative to the repulsive force. ζ_{ij} is called the effective coordination number of atoms taking into account the relative distance between two neighbors (r_{ij}, r_{ik}) and bond angle θ_{ijk}. The parameter d determines sensitivity of the potential to the angle and c expresses the strength of the angular effects. The parameter χ_{ij} strengthens or weakens heteropolar bonds in multicomponent systems. $\chi_{ij} = \chi_{ji}, \chi_{ii} = 1$ and $\omega_{ii} = 1$.

6.7 Potentials used in this work

Tersoff proposed [158] potential model and many researchers that have applied them to a number of different systems. These parameters have been successfully used for fitting to structural properties of carbon, BN, BCN systems and SiO [158, 160, 161, 162, 163]. We used Tersoff potentials (Table 6.1) for boron, carbon and oxygen taken from Matsunaga [161] and Munetoh [163] in our B_4C polar, B_4C chain and B_6O systems. We adjusted the parameter D in B_{12} and B_{50} systems for simulating icosahedral borides and we also adjusted the parameter χ_{B-O} to produce properties of B_6O. Potential parameters used in this work are listed in Table 6.1.

Table 6.1: Tersoff potential parameters used in this study. Parameters for B, C and O were taken from Matsunaga and Munetoh.

	B	C	O
A(eV)	2.7702×10^{2}	1.3936×10^{3}	1.88255×10^{3}
B(eV)	1.8349×10^{2}	3.467×10^{2}	2.18787×10^{2}
$\lambda(\mathring{A}^{-1})$	1.992	3.4879	4.17108
$\mu(\mathring{A}^{-1})$	1.5856	2.2119	2.35692
β	1.6000×10^{-6}	1.5724×10^{-7}	1.1632×10^{-7}
n	3.9929	0.72751	1.04968
c	5.2629×10^{-1}	3.8049×10^{4}	6.46921×10^{4}
d	1.5870×10^{-3}	4.384	4.11127
h	0.500	-0.57058	-8.45922×10^{-1}
$R(\mathring{A})$	1.8	1.8	1.7
$D(\mathring{A})$	1.7-2.1	2.1	2.0
Interactions $(i-j)$	B-C	B-O	
χ_{ij}	1.0025	0.93250	
ω_{ij}	0.9810	0.99917	

Chapter 7

Structural and Thermodynamic Properties of Simulations

7.1 Simulation Details

Molecular dynamics simulation using empirical potentials is a powerful tool for the analysis of large systems. We performed the MD simulations in the constant pressure, volume and temperature N(P,V) T until the structures converged to zero temperature. We used the DL POLY code [164] to equilibrate and simulate structural and thermodynamic properties of all the supercell structures studied in this work. We used more that large number steps (equilibration steps taken as 10% of total number of steps) with the time step of 10^{-6}ps and both Verlet algorithms (velocity and leapfrog) to integrate Newtonian equations of motion. Specifically, for borides (B_{12}

and B_{50}) total number of steps of 30 000 (equilibration steps of 3000), boron carbides (polar and chain) 70 000 (7000) and boron suboxide (B_6O) 170 000 (17 000) were used throughout simulations. We calculated different average properties after iterations.

The elastic constants were calculated using the free energy minimization method. Elastic constants were computed using the GULP (General Utility Lattice Program) [165]. The structure is equilibrated to a given temperature by minimizing the energy. The assumption made is that the vibrational motions in the solid consists of quantized harmonic oscillators whose frequencies vary with cell volume.

7.2 Zero Temperature Properties

Table 7.1 lists values of the elastic constants of B_4C and B_6O. The experimental values and other calculations are also listed for comparison purposes. GULP calculates bulk modulus from the methods defined by Reuss and Voigt [166] while Hill method is the average of the two. The elastic constants for boron carbide in comparison with experimental and other calculations are in fair agreement. There are no reports of experimental elastic constants values for B_6O. The Young's modulus (E), shear modulus (G) and bulk modulus (B) at ambient conditions have been experimentally measured and they are also listed in (Table 7.1). This indicates that this Tersoff potentials can be used to determined mechanical properties and the molecular dynamics of boron icosahedral structures.

Table 7.1: Calculated elastic properties in (GPa) using GULP. Other calculation and experimental values are listed.

Material	C_{11}	C_{12}	C_{13}	C_{33}	C_{44}	E	G	B
B_4C								
Present	540.89	180.03	98.20	520.34	305.22	467	200	234
Other	561.80[a]	123.56[a]	69.59[a]	517.72[a]	-	-	-	234[a]
Exp	542.81[b]	130.59[b]	63.51[b]	534.54[b]	164.79[b]	457[c]	193[c]	241[c]
B_6O								
Present	481	50	-6.31	232	274	538	137	155
Other	614.99[d]	122.22[d]	46.51[d]	474.12[d]	192.29[d]	507.8[d]	223.1[d]	233.7[d]
Exp	-	-	-	-	-	437[e]	206[e]	230[e]

[a]Reference [134]
[b]Reference [167]
[c]Reference [168]
[d]Reference [169]
[e]Reference [170]

The structural and thermodynamic properties reported here were calculated on molecular dynamics code DL_POLY. Table 7.2 list the simulated lattice parameters of various boron icosahedral structures. The advantage of MD codes over *ab-initio* codes especially DL_POLY, is that they are capable of handling large supercell, over hundreds of thousands atoms. In order to examine system dependence size we then generated 2x2x2, 4x4x4 and 8x8x8 supercells consisting of at least 288, 2304 and 18432 atoms respectively in a simulation cell with periodic boundary conditions. The agreement between MD and *ab-initio* is fair and generally good between ab-initio and experiment. This also indicates that the Tersoff potentials used in this work are not really excellent but could be adjusted in a way that they can be used to determine other structural properties related to boron icosahedral materials.

Table 7.2: Number of atoms in the supercell and lattice parameters of various Boron related compounds together with available experimental and theoretical calculations. Calculated GGA values in brackets.

Material			DL_POLY	VASP	Experiment
	Supercell	No atoms	Lattice	parameter(Å)	
$\alpha-B_{12}$	[2x2x2]	288	a = 4.404	a = 4.844	a = 5.057[171]
			c = 12.286	(4.900)	
($R\bar{3}m$)	[4x4x4]	2304	a = 4.451		
			c = 12.258	c = 12.401	
	[8x8x8]	18432	a = 4.713	(12.551)	
			c = 11.675		
t-B_{50}	[2x2x2]	400	a = 7.758	a = 8.734	a = 8.75[47]
			c = 4.433	(8.840)	c = 5.06[47]
($P4_2/nnm$)	[4x4x4]	3200	a = 7.907		
			c = 4.381	c = 4.903	
	[8x8x8]	25600	a = 7.940	(4.961)	
			c = 4.718		
B_4C polar	[2x2x2]	360	a = 5.245	a = 5.697	a = 5.61[125]
			c = 10.501	(5.764)	c = 12.14[125]
($R\bar{3}m$)	[4x4x4]	2880	a = 5.396		a = 5.60[126]
			c = 10.653	c = 11.604	c = 12.0-12.10[126]
	[8x8x8]	23040	a = 5.4486.	(11.758)	
			c = 10.5836		
B_4C chain	[2x2x2]	360	a = 5.174	a = 5.577	
			c = 11.695	(5.643)	
($R\bar{3}m$)	[4x4x4]	2880	a = 5.193		
			c = 11.584	c = 11.969	
	[8x8x8]	23040	a = 5.190	(12.139)	
			c = 11.638		
B_6O	[2x2x2]	336	a = 5.073	a = 5.392	a = 5.382[127]
			c = 11.567	(5.393)	c = 12.323[127]
($R\bar{3}m$)	[4x4x4]	2688	a = 5.049		a = 5.367[128]
			c = 11.512	c = 12.151	c = 12.238[128]
	[8x8x8]	21504	a = 5.0640	(12.314)	
			c = 11.5465		

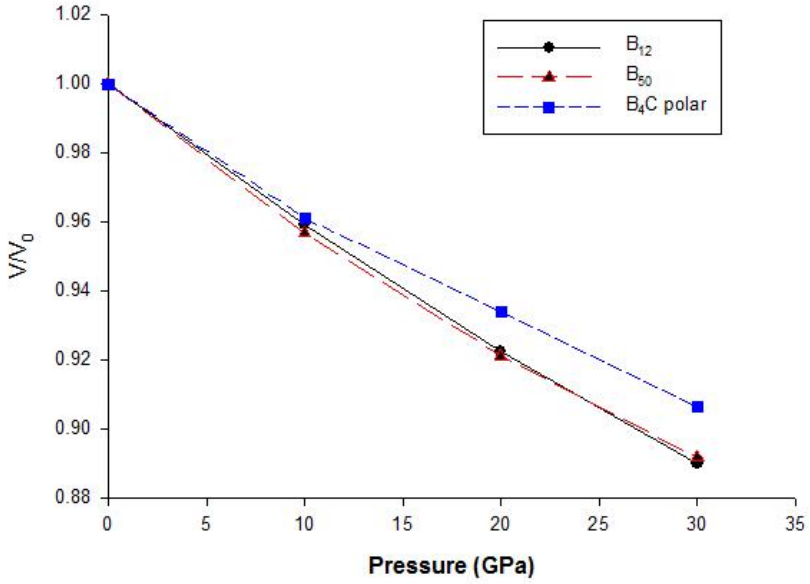


Figure 7.1: V/V_0 vs pressure for B_{12}, B_{50} and B_4C polar.

From MD calculation we determined the isothermal bulk modulus B and the pressure derivative at zero pressure for materials in Table 7.2 by analyzing simulated data at different pressures fitting it to Birch equation of state [132]. Figures 7.1 and 7.2 shows pressure dependence of V/V_0 of borides and Table 7.3 shows the calculated bulk modulus (B) and pressure derivative (B') together with experimental and first principle calculations. We also calculated B when B' is fixed to 4. Reason for the differences between GULP and DL_POLY cannot be understood but there is a good agreement with DL_POLY and VASP for the bulk modulus.

Figure 7.3 displays the bulk modulus versus system size. We see that the system size does affect bulk modulus, but not that much. Large supercell will obviously

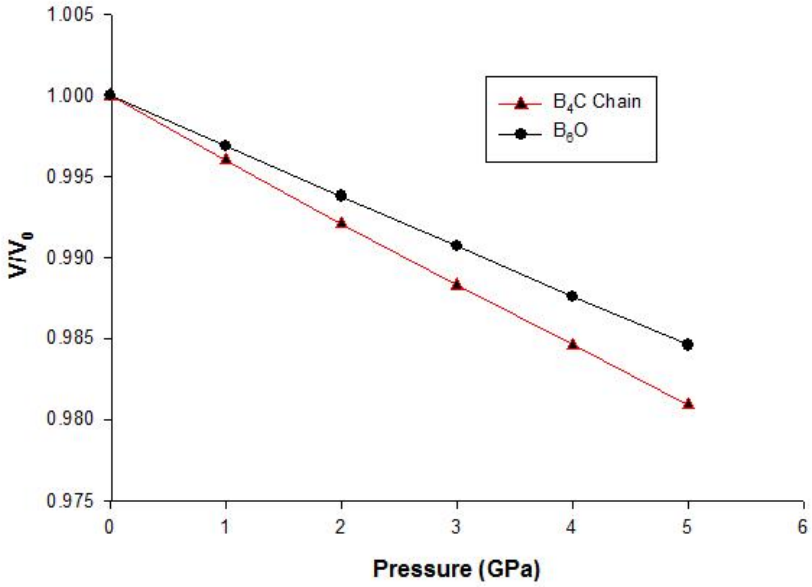


Figure 7.2: V/V_0 vs pressure for B_4C chain and B_6O.

Table 7.3: Bulk Moduli B, pressure derivatives B' of various Boron compounds and some experimental values.

Material	Bulk modulus DL_POLY,{B'}	B (GPa) [B'=4]	VASP{B'} (GGA)	Exp{B'}
B_{12}[2x2x2]	231{2.26}	[210]	226.1{3.8}	213-224{4.0}[172]
[4x4x4]	219{3.86}	[217]	(214),{10.1}	
[8x8x8]	241{2.10}	[217]		
B_{50}[2x2x2]	207{4.34}	[210]	206,{3.8}	
[4x4x4]	210{3.77}	[208]	(193),{3.9}	
[8x8x8]	208{1.84}	[181]		
B_4C polar[2x2x2]	241{5.17}	[254]	229,{3.5}	241[168]
[4x4x4]	222{6.16}	[244]	(213),{3.7}	
B_4C chain[2x2x2]	246{5.38}	[260]	241,{3.7}	
[4x4x4]	253{4.75}	[261]	(223),{3.6}	
[8x8x8]	249{4.43}	[253]		
B_6O[2x2x2]	275{2.73}	[273]	246,{3.3}	270{1.8}[21]
[4x4x4]	320{0.711}	[313]	(229),{3.4}	213{4}[21]
				181{6}[136]

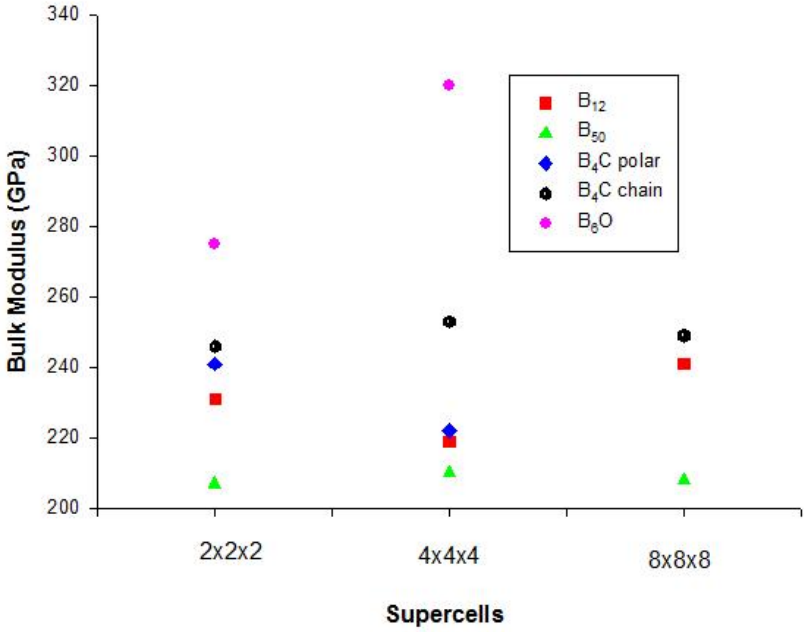


Figure 7.3: Bulk Modulus vs system size

require much computer time and memory and therefore we calculated thermodynamics properties for our systems using 4x4x4 supercell at pressure at zero and high temperatures on DL_POLY.

7.3 Thermodynamic Properties of Borides

The molecular dynamic simulations are employed as being a way to investigate the behavior of large numbers of atoms and thus material behavior at high temperatures. We simulated the above structures from 300K to 3000K with 4x4x4 supercell in order to obtain thermodynamic properties at high temperatures. The radial distribution

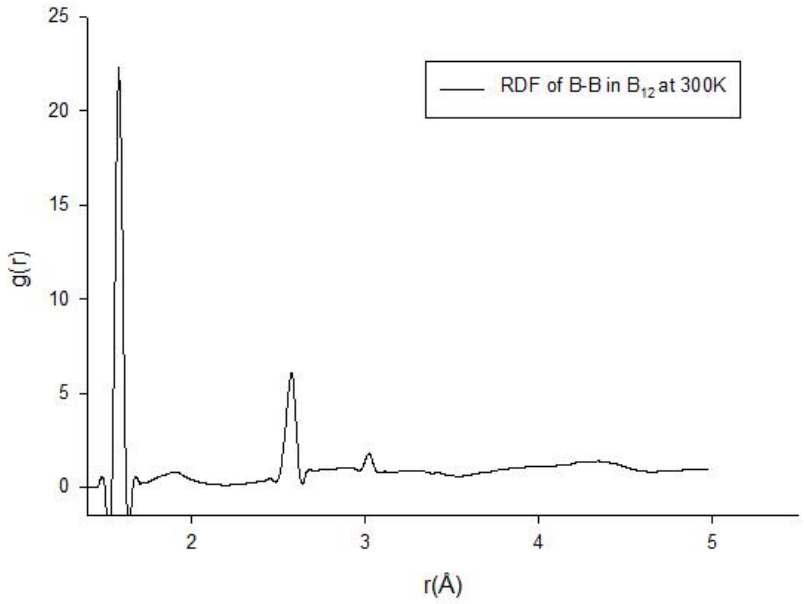


Figure 7.4: RDFs pairs of B-B in B_{12}.

functions (RDFs) for all pairs were calculated and in Figures 7.4-7.8 we display the RDFs at 300K. We have a sharp first peaks starting below 2 Å for all pair except for O-O in B_6O. These peaks shows that the structures are well ordered at room temperature. This is expected for solids because of the collisions between atoms at low temperatures is weak.

Figures 7.9-7.14 show the bulk structures of $\alpha-B_{12}$, B_4C chain and B_6O simulated at temperatures 300K and 3000K. The structures at 300K and 3000K are not the same,. therefore, the crystalline structures disappears at high temperatures and the bulk structures melts. The increase in the temperature increases the kinetic energies of the atoms and therefore the impact between them is higher causing disorders in

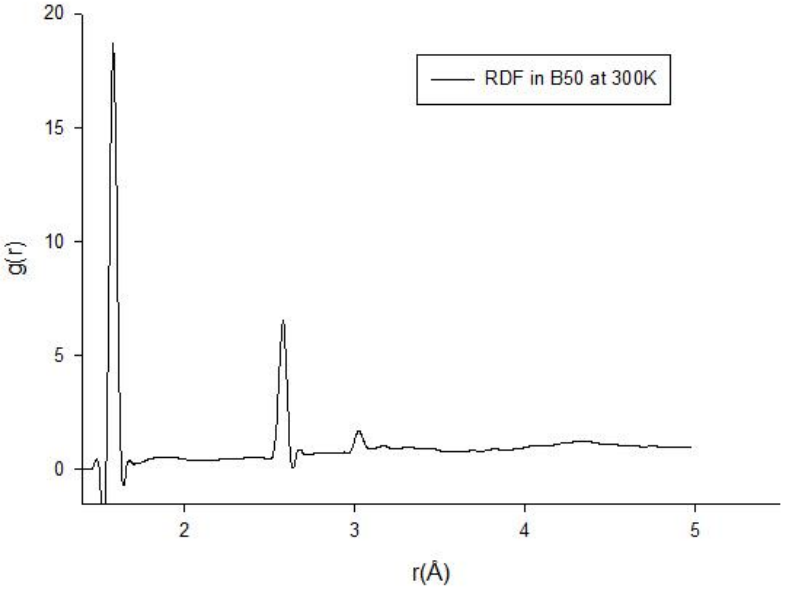


Figure 7.5: RDF pairs of B-B in B_{50}.

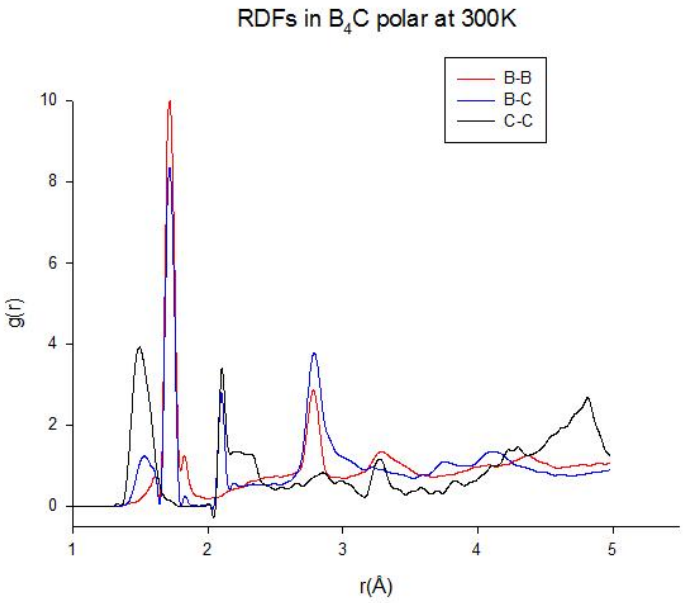


Figure 7.6: RDF pairs B-B, B-C and C-C in B_4C polar.

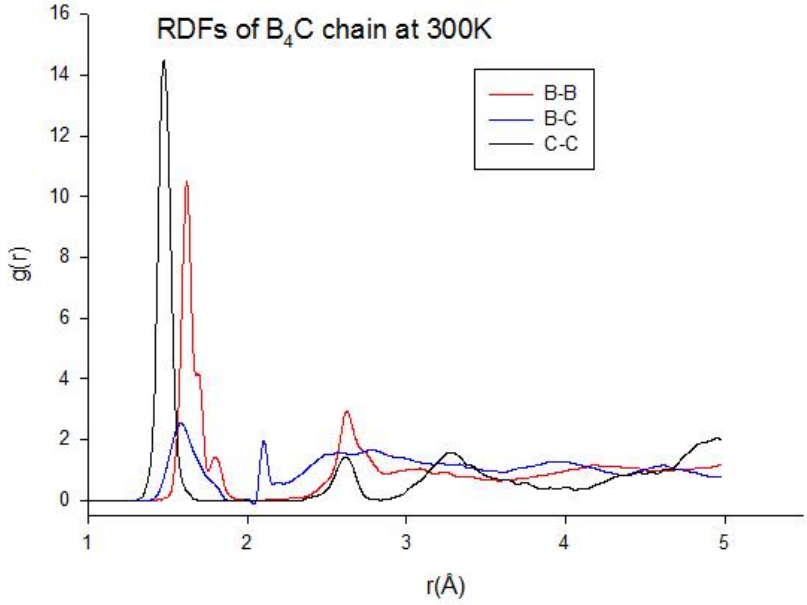


Figure 7.7: RDF pairs B-B, B-C and C-C in B_4C chain.

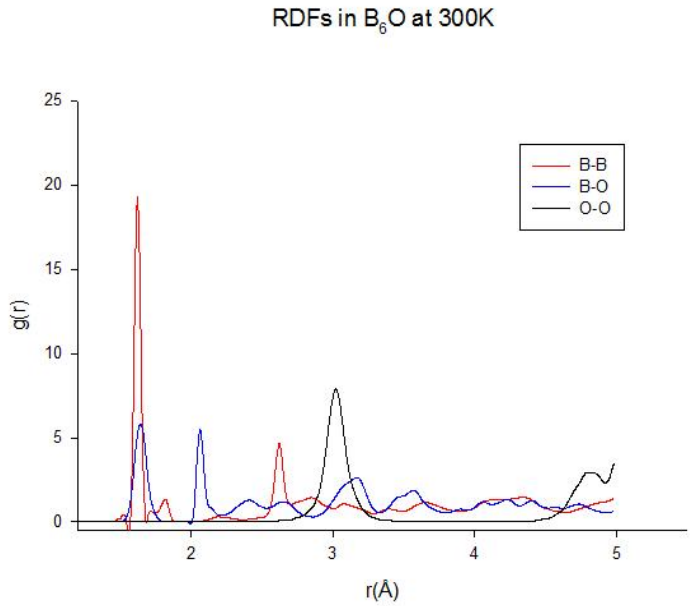


Figure 7.8: RDF pairs B-B, B-O and O-O in B_6O.

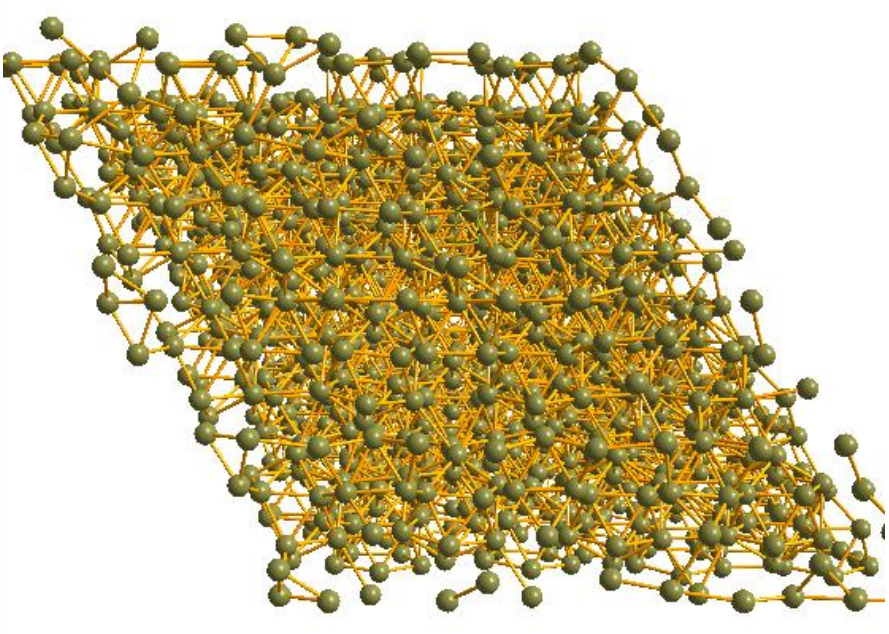


Figure 7.9: Bulk crystal of $\alpha-B_{12}$ at 300K.

the structures.

Figures 7.15 to 7.18 shows the RDFs for borides, boron carbides and boron suboxide respectively at 3000K. The first peaks decreased in size while others broaden away from the first at high temperatures. This means that as the temperature is increased, thermally generated defects are introduced and hence disorder is increased.

The melting of solids is one the most common observations of a phase transition, while the mechanism of melting is still an outstanding problem in condensed matter physics [173]. On the basis of thermodynamics a phase transition is characterized by abrupt change in the slope of the total energy against temperature curve. A similar curve is also expected in the pressure against temperature of a constant volume

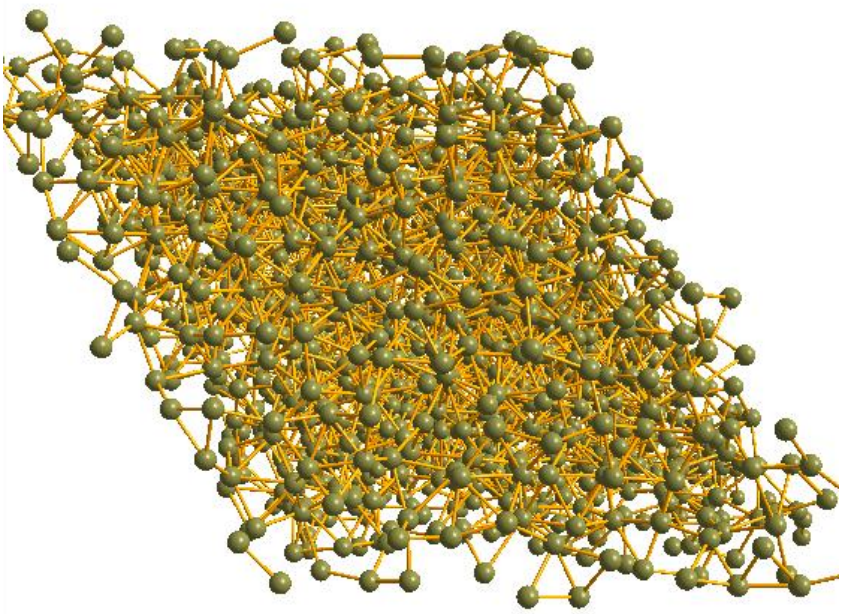


Figure 7.10: Bulk crystal of $\alpha-B_{12}$ at 3000K.

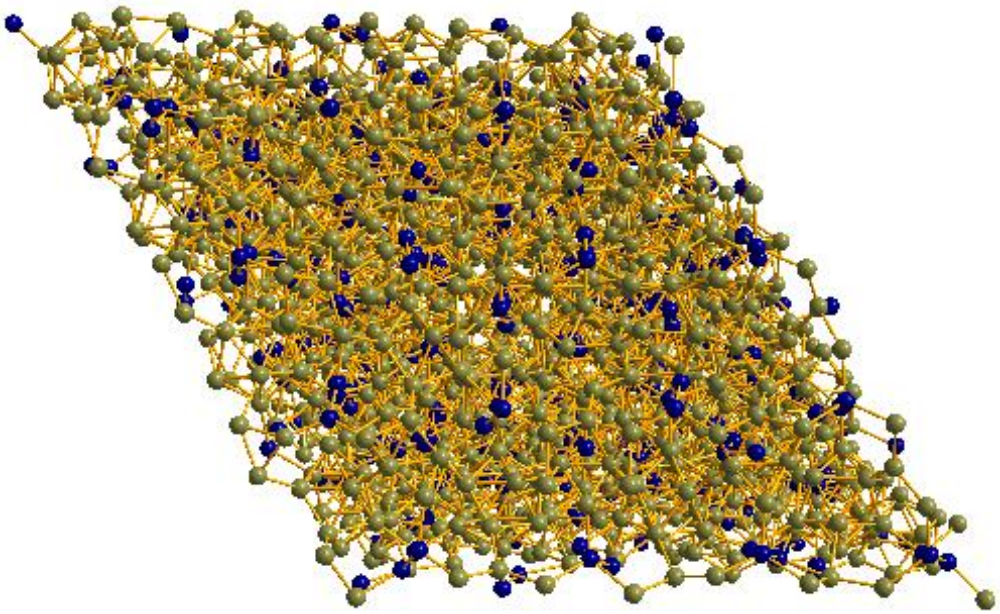


Figure 7.11: Bulk crystal of B_4C chain at 300K.

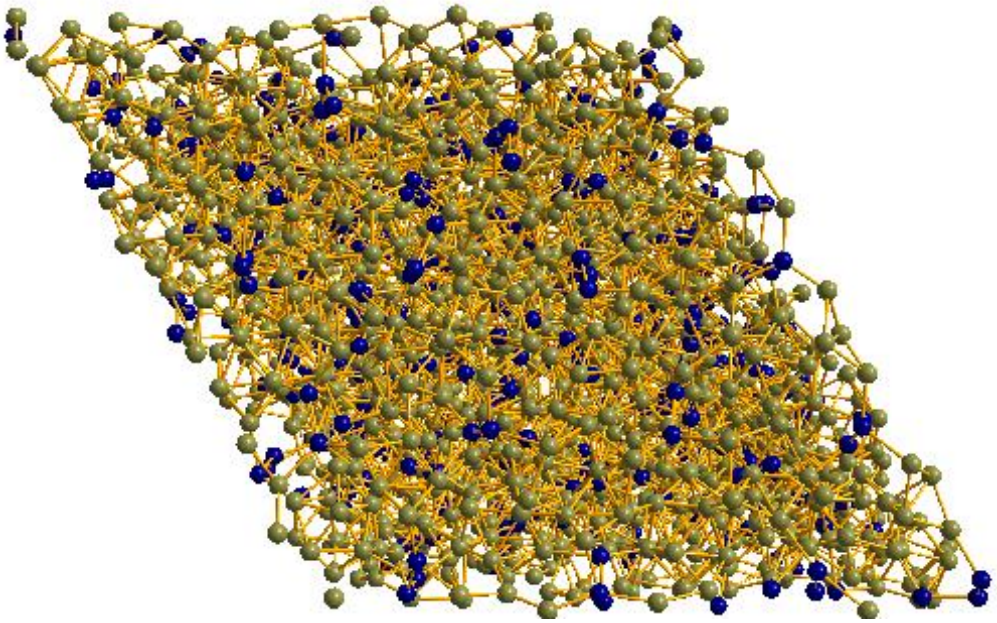


Figure 7.12: Bulk crystal of B_4C chain at 3000K.

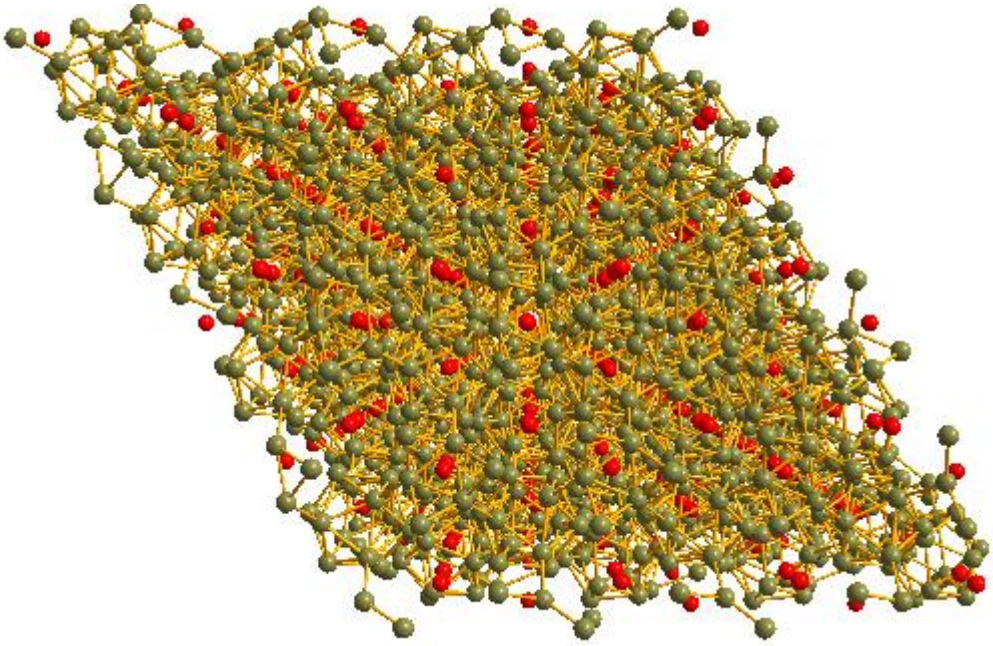


Figure 7.13: Bulk crystal of B_6O at 300K.

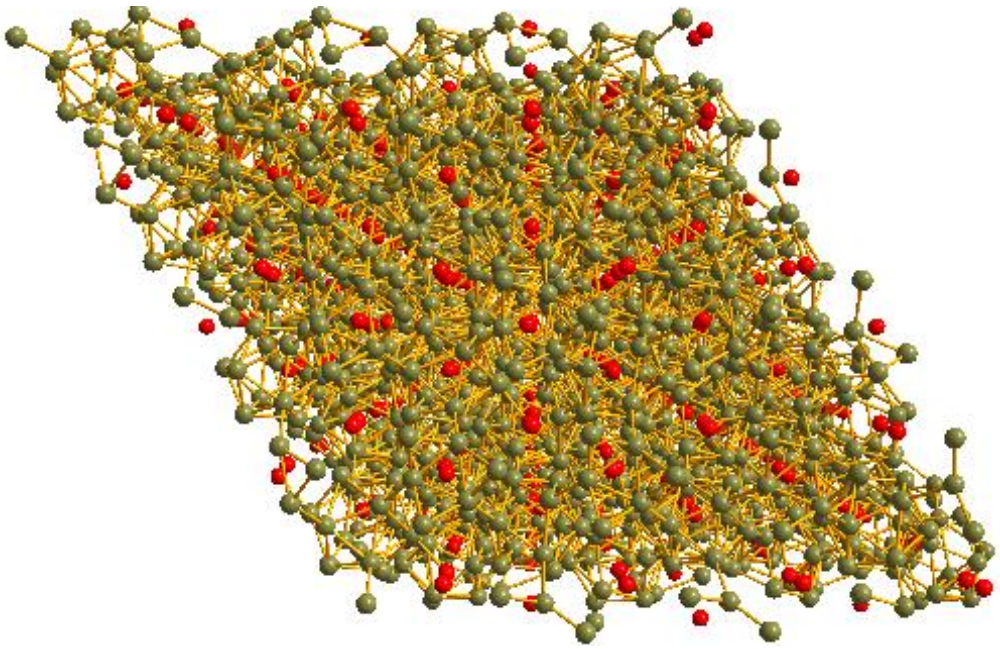


Figure 7.14: Bulk crystal of B_6O at 3000K.

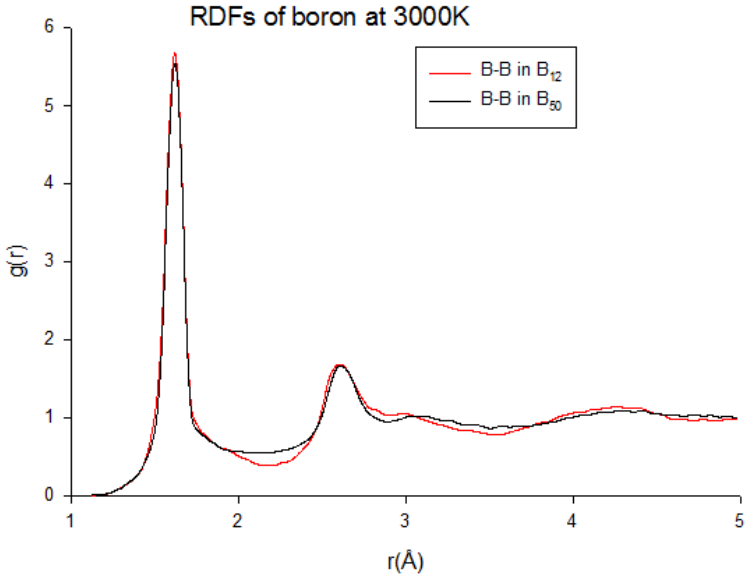


Figure 7.15: RDFs of Boron at 3000K

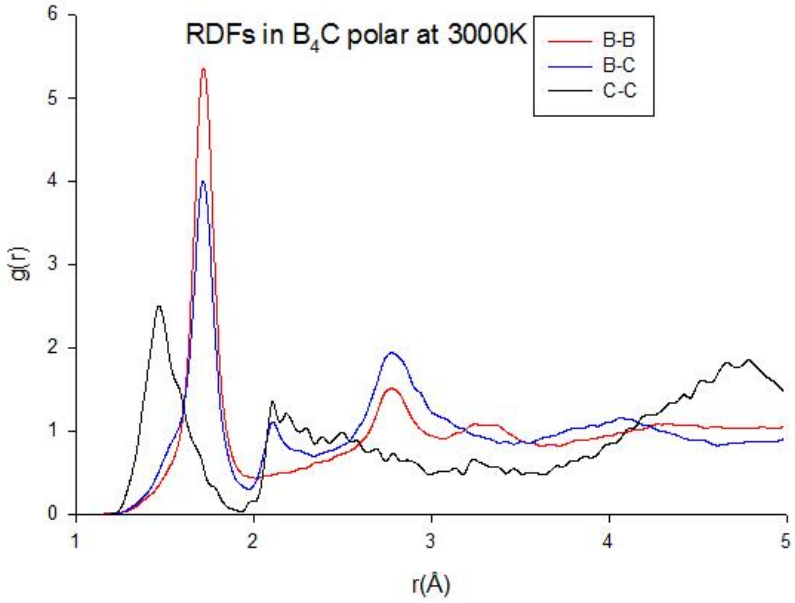


Figure 7.16: RDF pairs B-B, B-C and C-C in B_4C polar.

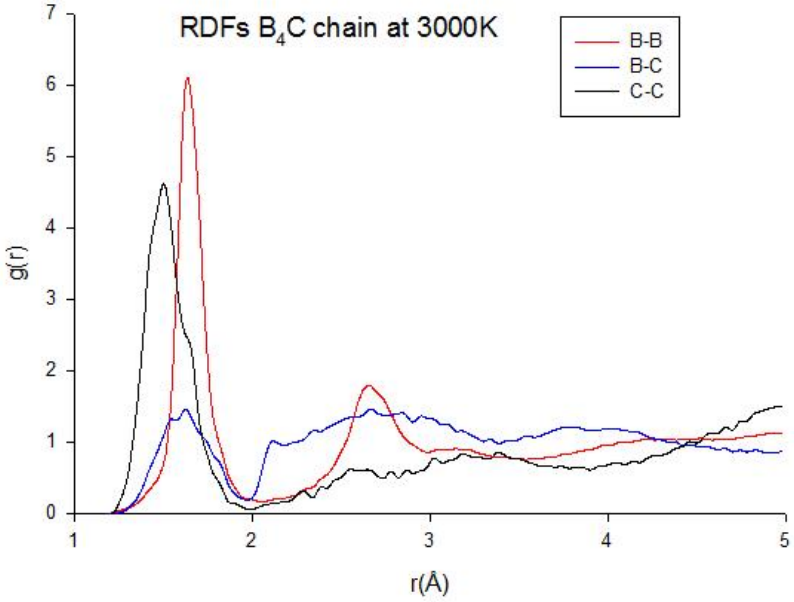


Figure 7.17: RDF pairs for B_4C chain at 3000K.

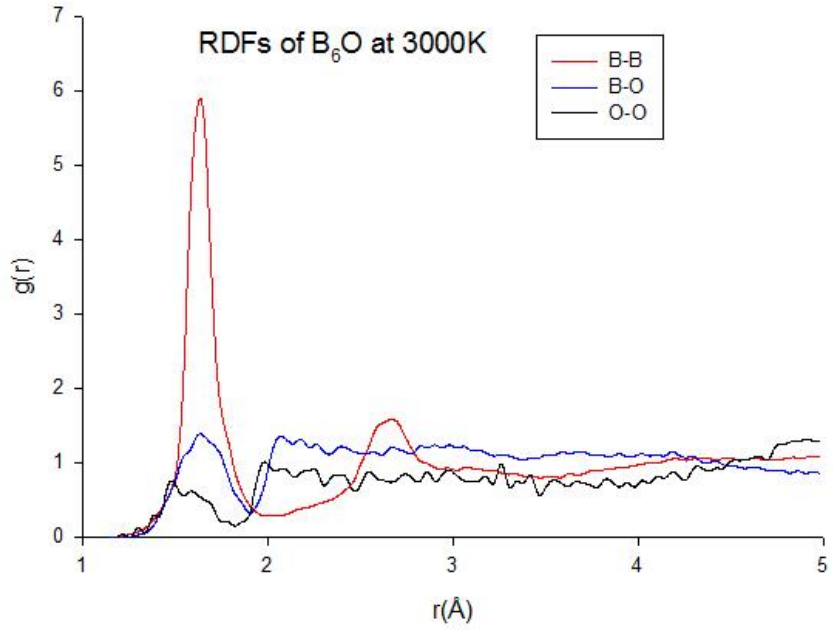


Figure 7.18: RDF pairs for B_6O at 3000K.

experiment [174]. Figure 7.19 shows the variation of pressure against temperature for borides. We notice a change in the slope around 1500K. This means that there is also a change in the specific heat and thermal expansions for these borides around this temperature.

We plotted the diffusion coefficient of boron atoms in different systems in Figure 7.20. The diffusion coefficient decays to a very to a very small value with lower temperature which is a similar trend of pressure temperature variation.

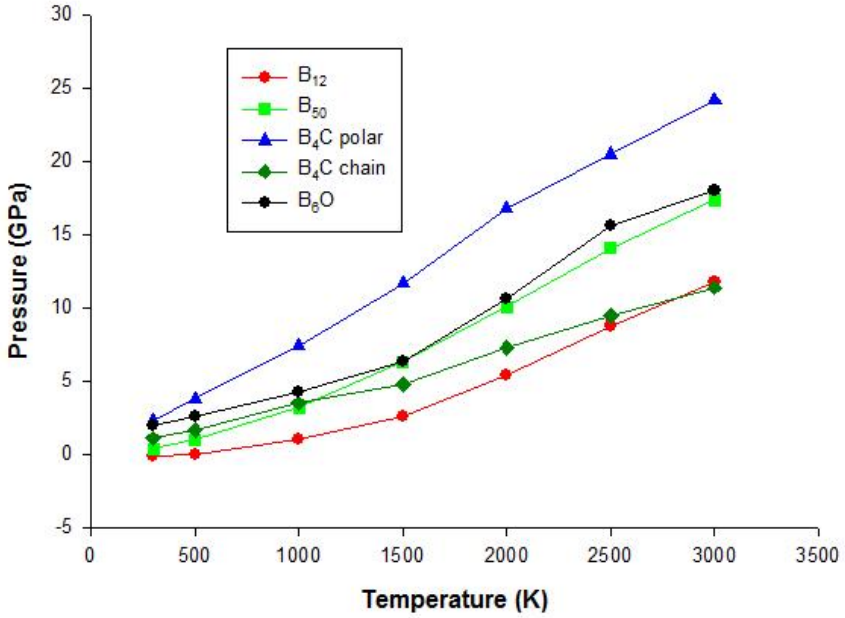


Figure 7.19: Variation of pressure against temperature for the borides.

7.3.1 Specific heat and thermal expansions

From above we notice the factors affecting the properties of material. The effect of temperature is the major one in many systems and therefore, we predict properties such as specific heat and thermal expansions at higher temperatures. Figures 7.21-7.25 are the plots of total energy against temperature for our systems above 1500K, which we estimate it to be the temperature above Debye temperature for boron icosahedral materials [175].

In MD motion of atoms are treated classically and therefore quantum effects are ignored above Debye temperatures. We predict the specific heat C_v for the borides from the derivative of the total energy of the system using the relation

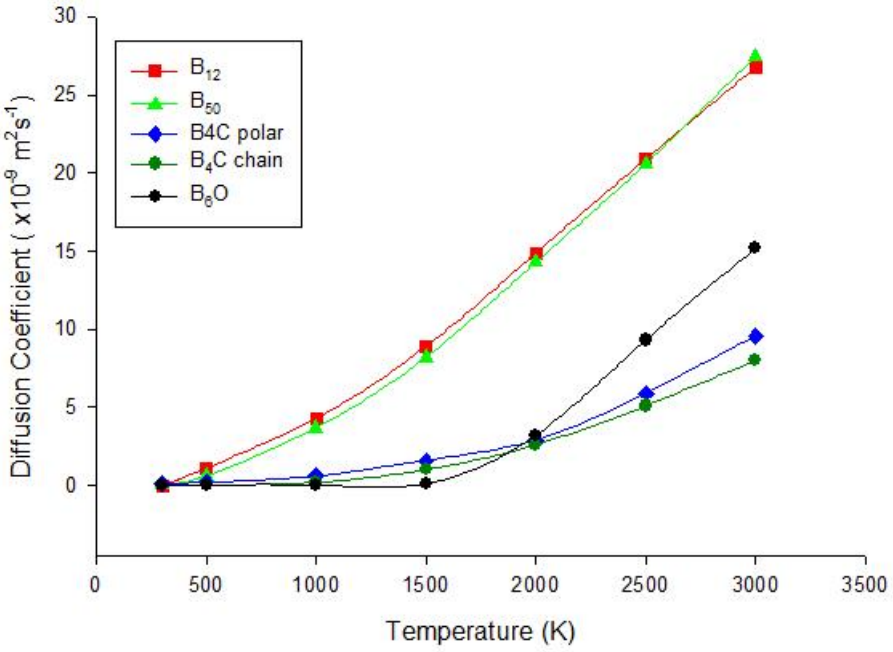


Figure 7.20: Variation between diffusion coefficient and temperature of boron atoms in icosahedral systems.

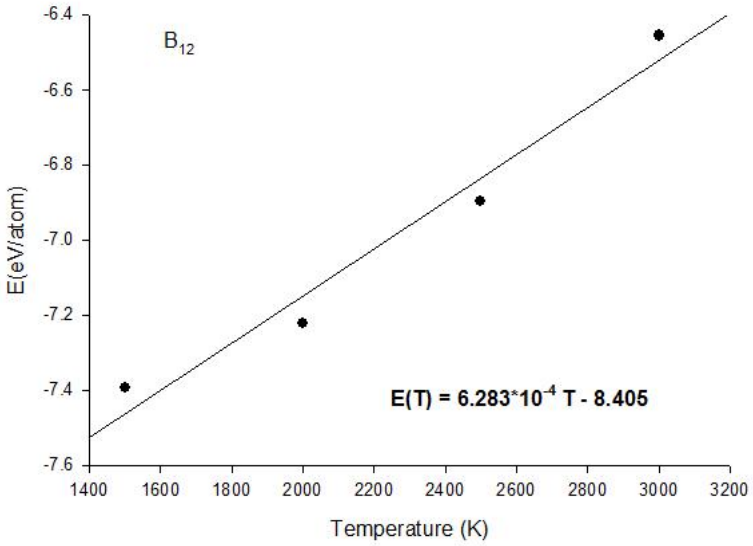


Figure 7.21: Energy as a function of temperature for B_{12}.

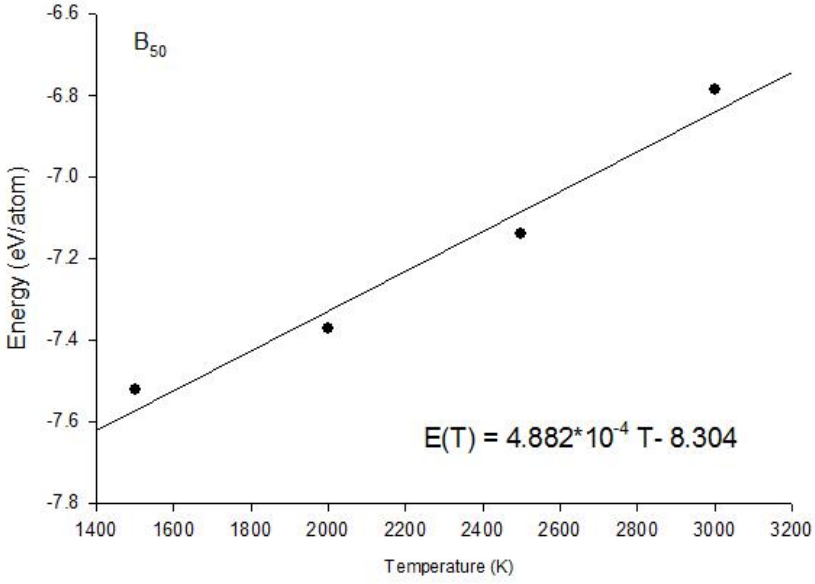


Figure 7.22: E vs T in B_{50}.

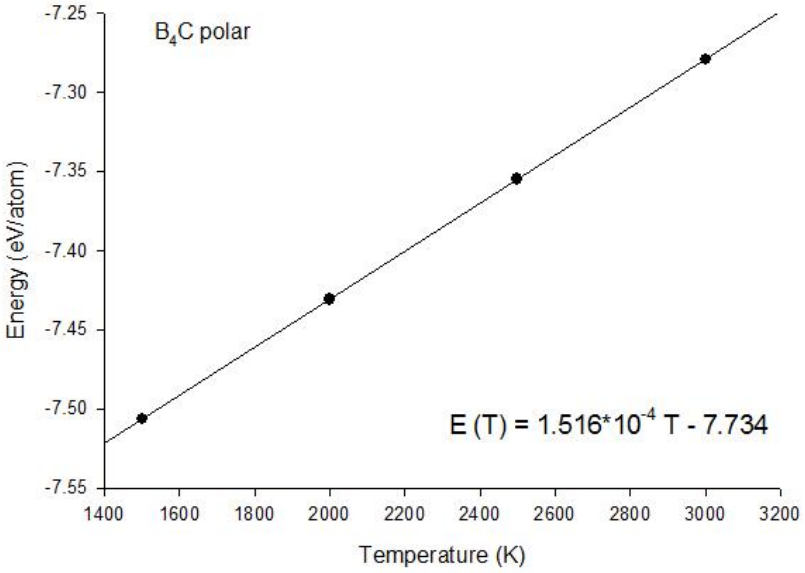


Figure 7.23: E vs T in B_4C polar.

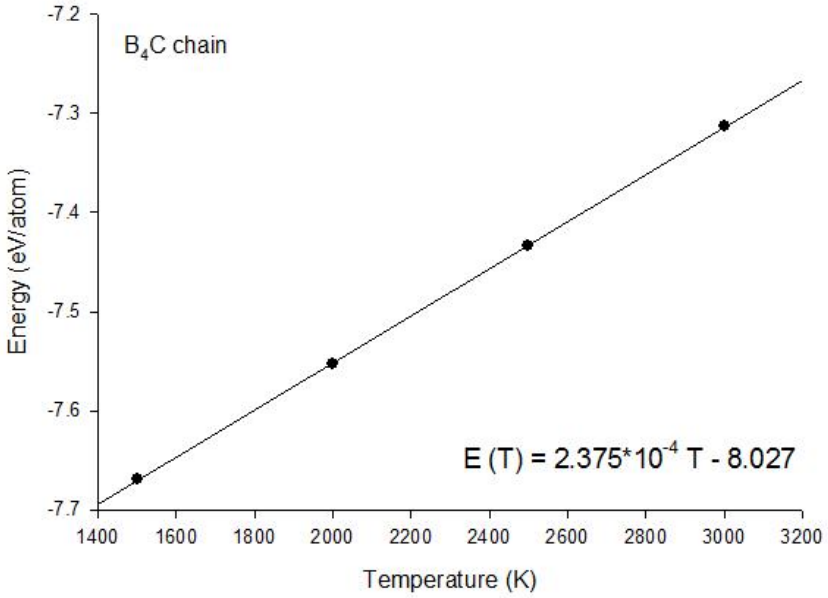


Figure 7.24: E vs T in B_4C chain.

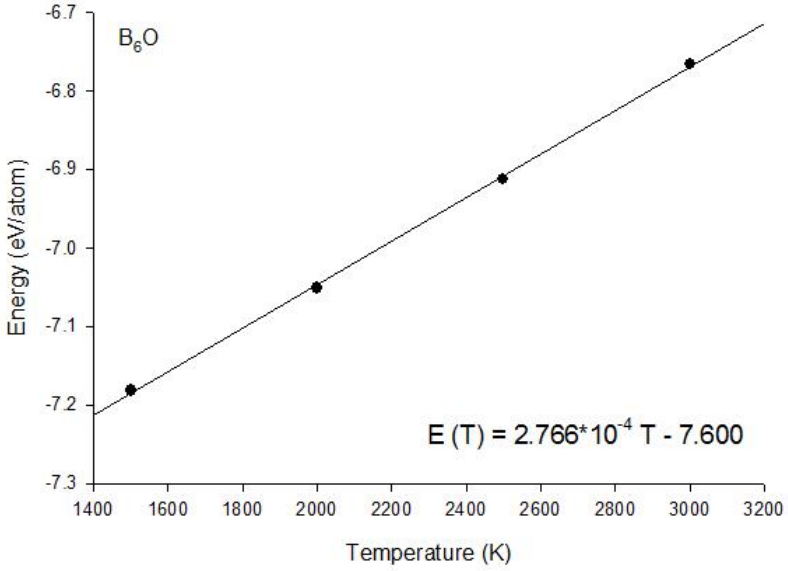


Figure 7.25: E vs T in B_6O.

$$C_v = \left| \left(\frac{\partial E}{\partial T} \right) \right|_v .$$

The computed slopes of energy-temperature curves in Figures 7.21-7.25 gives the specific heats shown in Table 7.4. The calculated specific heats for B_4C and B_6O compare well to the classical Dulong-Petit result ($3k_B$) [176]which is obtained for all solids at high temperatures.

Figures 7.26-7.35 shows the lattice parameters a and c axis against the temperature at zero pressure. The linear thermal expansion coefficients, α_a and α_c along a and c axis in MD simulation can be computed directly from the definition as the temperature derivative of the lattice parameter along that axis.

Table 7.4: Thermodynamic properties of boron, boron carbide and boron suboxide.

	Diamond	BN	B_{12}	B_{50}	B_4C polar	B_4C chain	B_6O
$C_v(k_B)$	2.97[a]	3.02[c] 5.16[e]	7.29[g] 2.78[k]	5.66[g]	2.32[g]	2.76[g]	3.21[g]
$\alpha_{l_{300K}}(10^{-6}K^{-1})$	1.017[b]	1.8[d]	2.216[g]	3.244[g]	1.858[g]	3.116[g]	1.721[g]
$\alpha_{l_{1500K}}(10^{-6}K^{-1})$	5.181[b]	5.47[c], 6-8[f]	1.984[g]	4.841[g]	1.477[g]	4.598[g], 4.5[h]	5.171[g], 5.5[h]
γ	0.9[i]	1.2-1.5[j]	0.08[g] 1.75[k]	0.20[g]	0.67[g]	0.55[g]	0.71[g]

[a]Reference [177]
[b]Reference [178]
[c]Reference [179]
[d]Reference [180]
[e]Reference [181]
[f]Reference [182]
[g]This work
[h]Reference [64]
[i]Reference [183]
[j]Reference [184]
[k]Reference [60]

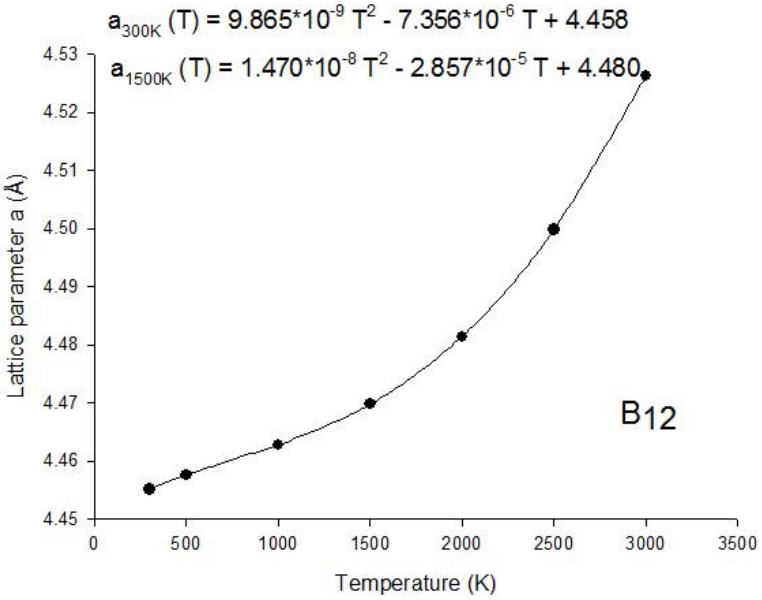


Figure 7.26: Lattice variation along a axis in B_{12}.

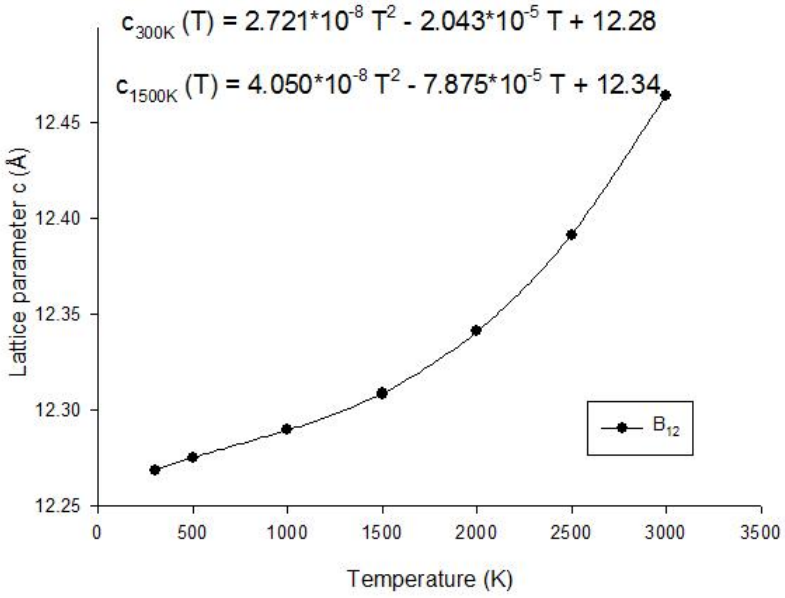


Figure 7.27: Lattice variation along c axis in B_{12}.

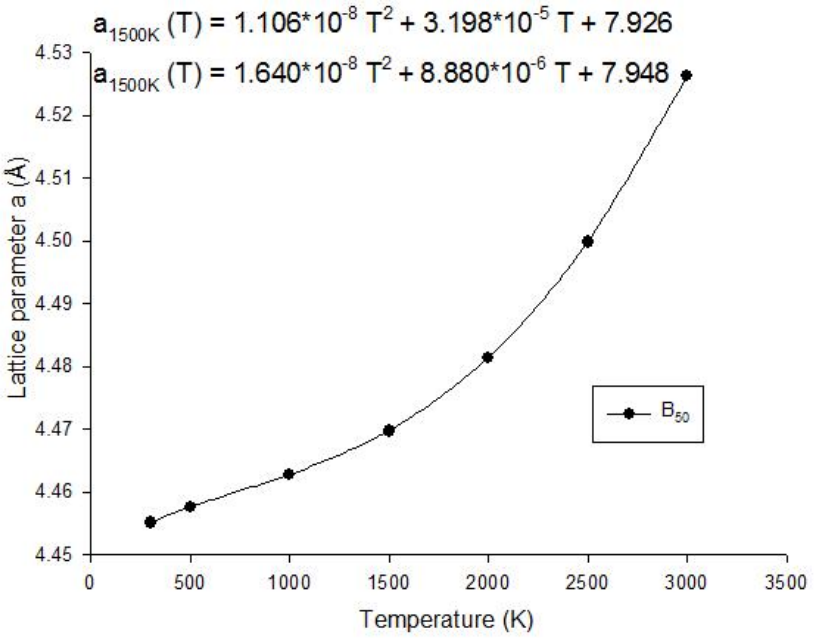


Figure 7.28: Lattice variation along a axis in B_{50}.

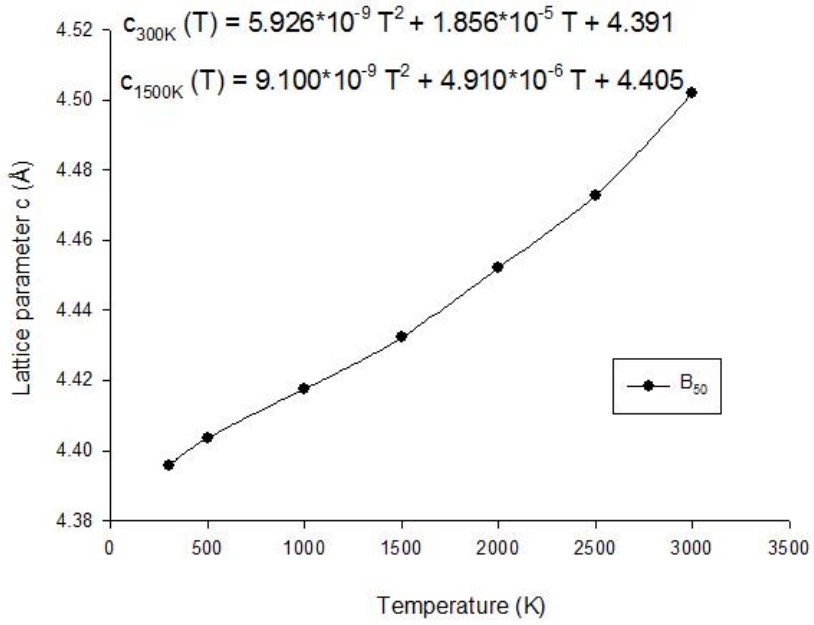


Figure 7.29: Lattice variation along c axis in B_{50}.

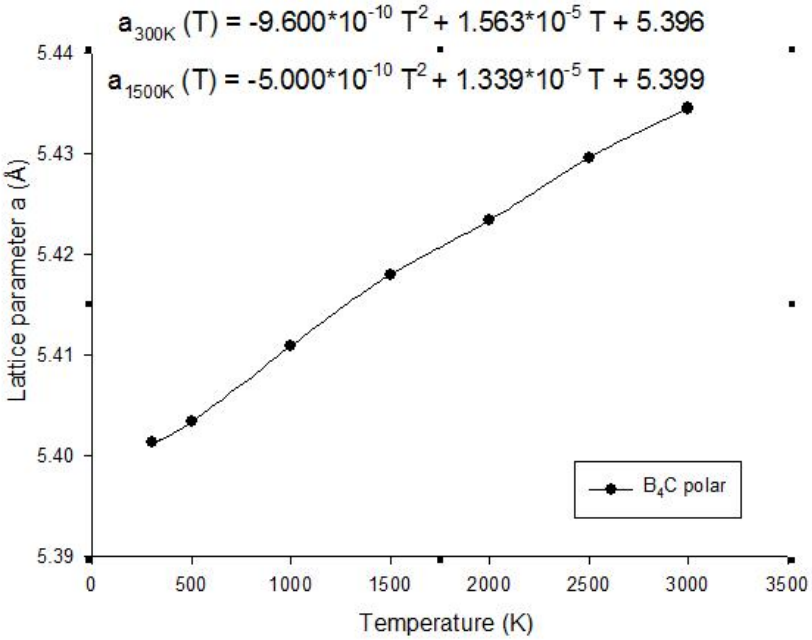


Figure 7.30: Lattice variation along a axis in B_4C polar.

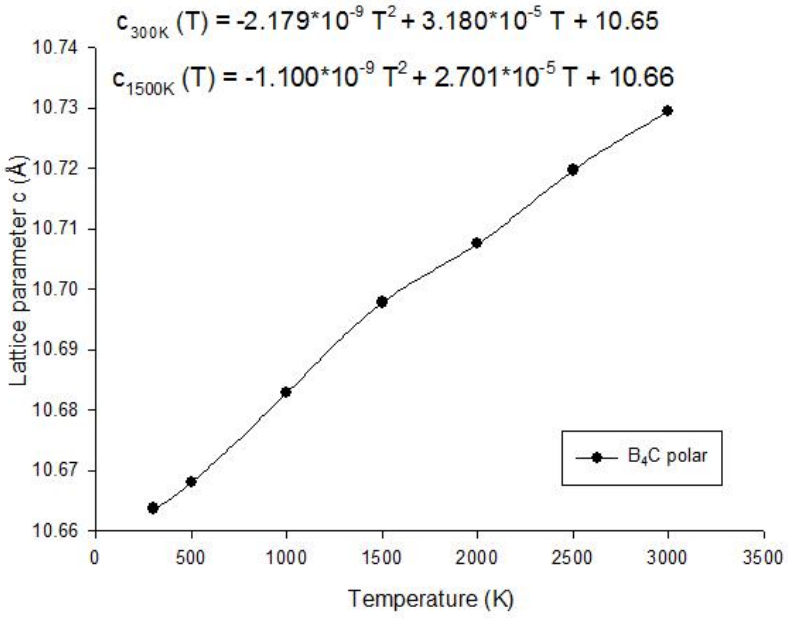


Figure 7.31: Lattice variation along c axis in B_4C polar.

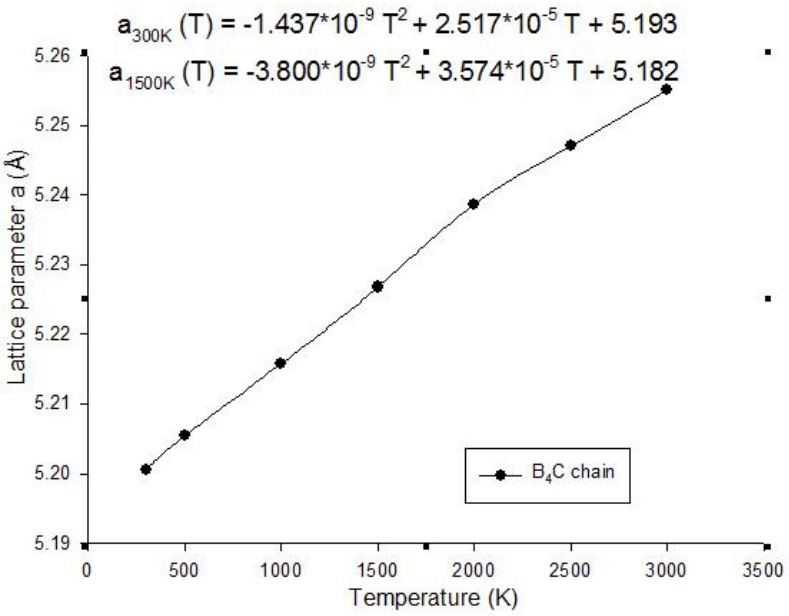


Figure 7.32: Lattice variation along a axis in B_4C chain.

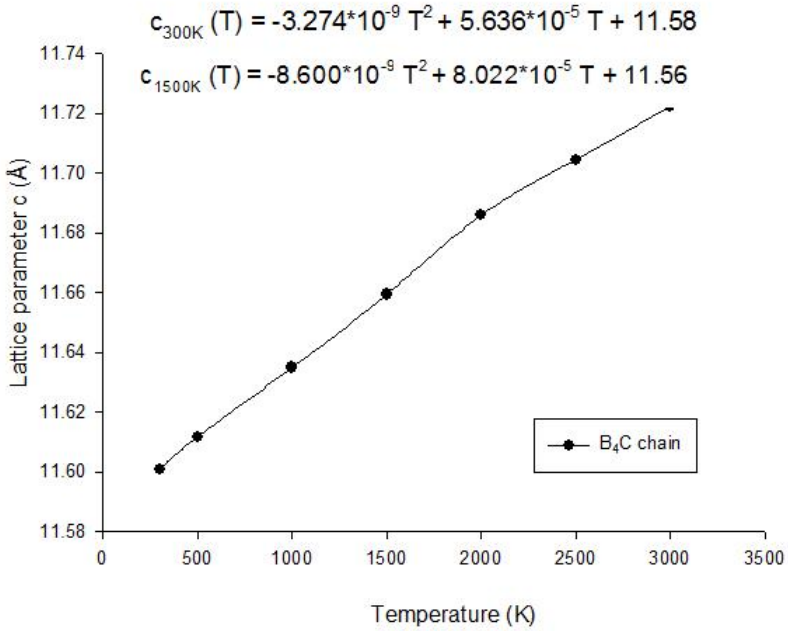


Figure 7.33: Lattice variation along c axis in B_4C chain.

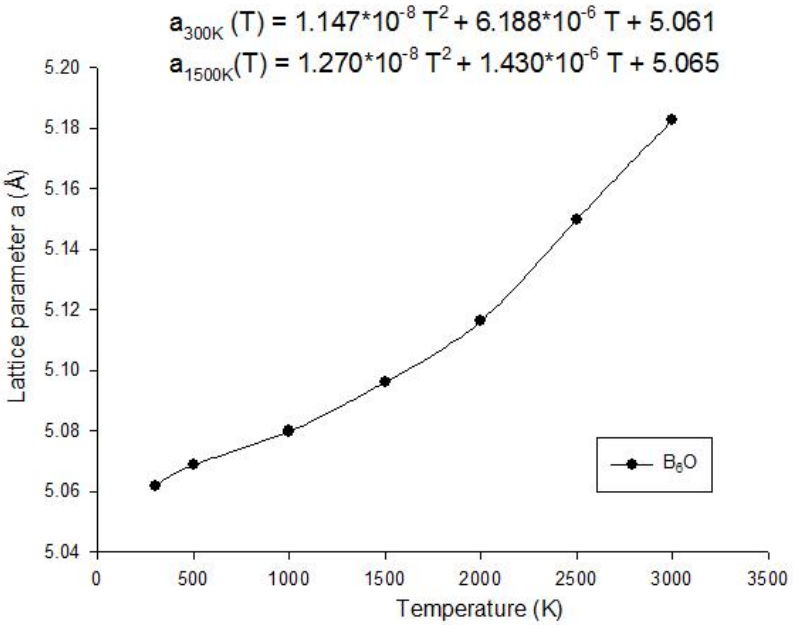


Figure 7.34: Lattice variation along a axis in B_6O.

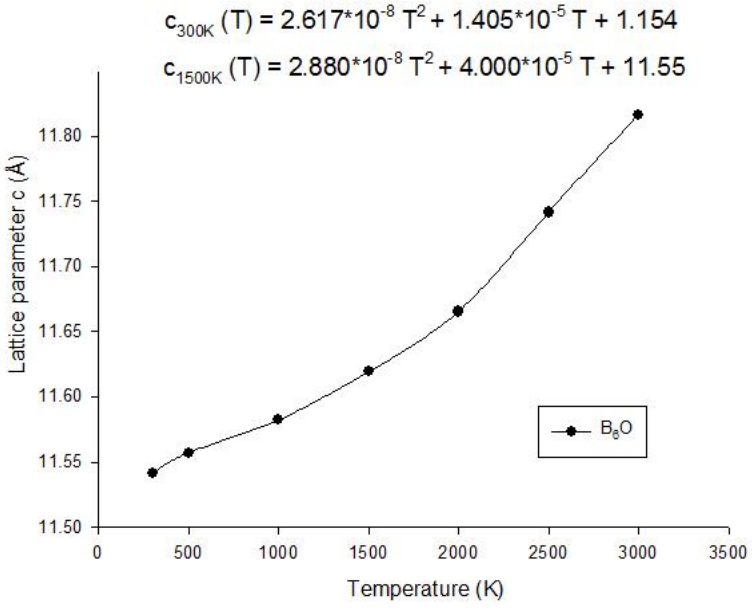


Figure 7.35: Lattice variation along c axis in B_6O.

$$\alpha_{(a,c)} = \frac{1}{(a,c)} \left. \frac{\partial(a,c)}{\partial T} \right|_P \tag{7.1}$$

where a,c is the lattice parameter along a or c axis. The average linear thermal expansion coefficient, α_l, was calculated using the formula

$$\alpha_a = \frac{1}{3}(2\alpha_a + \alpha_c) \tag{7.2}$$

The thermal expansion coefficient increases linearly with temperature and we obtained the slightly larger thermal expansion along c axis than a axis at 300K. The results for the average expansion coefficient of these borides at 300K and 1500K computed using equation (7.2) are listed in Table 7.4. The results are listed with strongest hard materials diamond and boron nitride.

We finally calculated the Grüneisen parameters for the borides (Table 7.4). He observed that for large number of crystalline solids the coefficient thermal expansion, should be proportional to the specific heat, C_v over quite wide ranges of temperatures and even at low temperatures. The Grüneisen rule is expressed in the form

$$\gamma = \frac{3BV\alpha_l}{C_v} \tag{7.3}$$

where V is the volume of the solid, B is the bulk modulus and γ is the dimensionless quantity referred as Grüneisen constant. All parameters are in Table 7.4.

Chapter 8

Elastic Properties and Some Defects in Ultra Hard Boron Suboxide (B_6O)

In this Chapter our focus is on the elastic properties of boron suboxide (B_6O) and the role of some defect types in the structure. The purpose of this work is to examine fundamental properties of B_6O with a purpose to see how various defects (extrinsic or otherwise) could influence its properties. The reason for this choice is that, it is an ultra hard boron rich solid which posses a great combination of physical and chemical properties among the borides presented so far. It has been extensively investigated in search of new candidates for ultra-hard materials. It is a promising candidate for cutting tools and in the applications where abrasive wear resistant is

important. The dramatic interest in B_6O compounds arises from the fact that they have a better oxidation resistant than diamond materials and also that B_6O is as hard as cBN[185]. B_6O materials have always been suspected to be a harder material than boron carbide (B_4C) materials. The hardness in boron rich solids is associated with some kind of bonding which arises from the inter-icosahedra atoms such as O and C in B_6O and B_4C respectively. This contributes significantly to their hardness because of strong covalent bonds linking boron atoms between the icosahedra and since oxygen is more electronegative than carbon then B_6O may be the hardest boron rich solid and therefore the hardest material after diamond and cubic boron nitride. We therefore studied the properties which influences the strength of this material by calculating elastic properties and creating vacancies and substitutional defects in this structure. The lightweight nature of B_6O makes it quite a unique material for superhard applications. To do this we first consider the bulk elastic properties and examine how these compare with experiment. Thereafter properties of B_6O with various defects included are examined.

8.1 Calculation of Elastic Properties

Many scientific-technological advances depend greatly on solid-state elastic properties, especially on their magnitude as well as their responses to their stress and temperature variables. Elastic constants relate to various fundamental solid-state phenomena, such as interatomic potentials or binding forces and equation of state. In thermody-

namics they are related to specific heat, thermal expansion, Debye temperature and Grüneisen's constant. In engineering they are used in calculations for load deflection residual stress, thermoelastic stress, fracture toughness and elastic instabilities[186].

Thus elastic constants are applicable to many disciplines: structural design, material science and solid-state physics. They may be applied to technological structural economics, safety, and may be used to describe various materials phenomena and fundamental interatomic forces.

In general the atomic structural arrangement of a material and the strength of its interatomic bonding forces determine the elastic behavior of a crystal [187]. The elastic properties of a material are of great importance in determining its behavior when subjected to deformation [188]. For example, the modulus of elasticity fixes the levels of stress which are generated if a material is strained by the application of a temperature. this can occur when the material is suddenly heated or cooled. In tis case a low modulus of elasticity is desirable. Since solids resist both volume change and shape change, they have at least two independent elastic constants, the shear modulus and the bulk modulus and they are more computational demanding for low symmetry materials.

Elastic stress tensor σ_{ij} may be expressed in terms of elastic strain tensor ϵ_{ij} according to Hooke's law by the equation:

$$\sigma_{ij} = c_{ijkl}\epsilon_{ij} \tag{8.1}$$

where the c_{ijkl} are the 81 elastic stiffness constants of the crystal and also form the forth-rank tensor [166]. The stress and strain tensors are symmetric with respect to interchange of their indices. The number of independent elastic constants depends on the crystal symmetry and it reduces from 81 to 21 by the index symmetries of stiffness tensor. In the c_{ijkl} the first two indices are abbreviated into single one running from 1 to 6 and the last two are abbreviated in the same way, according to the scheme,

Tensor notation	11	22	33	23, 32	31,13	12,21
Matrix notation	1	2	3	4	5	6

and is called the Voigt contraction and therefore we can rewrite equation (8.1) in the form:

$$\sigma_i = c_{ij}\epsilon_i (i, j = 1, 2, ..., 6) \tag{8.2}$$

The arrays of c_{ij} written out in squares, thus

$$\begin{pmatrix} c_{11} & c_{12} & c_{13} & c_{14} & c_{15} & c_{16} \\ c_{21} & c_{22} & c_{23} & c_{24} & c_{25} & c_{26} \\ c_{31} & c_{32} & c_{33} & c_{34} & c_{35} & c_{36} \\ c_{41} & c_{42} & c_{43} & c_{44} & c_{45} & c_{46} \\ c_{51} & c_{52} & c_{53} & c_{54} & c_{55} & c_{56} \\ c_{61} & c_{62} & c_{63} & c_{64} & c_{65} & c_{66} \end{pmatrix} \tag{8.3}$$

Table 8.1: Independent cij in the crystal structures.

Crystal Structure	c_{ij}
Cubic	c_{11}, c_{12}, c_{44}
Hexagonal	$c_{11}, c_{12}, c_{13}, c_{33}, c_{44}$
Tetragonal	$c_{11}, c_{12}, c_{13}, c_{33}, c_{44}, c_{16}, c_{66}$
Trigonal	$c_{11}, c_{12}, c_{13}, c_{33}, c_{14}, c_{44}, c_{25}$
Orthorhombic	$c_{11}, c_{12}, c_{13}, c_{22}, c_{23}, c_{33}, c_{44}, c_{55}, c_{66}$
Monoclinic	$c_{11}, c_{12}, c_{13}, c_{22}, c_{23}, c_{33}, c_{15}, c_{25}, c_{35}, c_{44}, c_{46}, c_{55}, c_{66}$
Triclinic	$c_{11}, c_{12}, c_{13}, c_{14}, c_{15}, c_{16}, c_{22}, c_{23}, c_{24}, c_{25}, c_{26}, c_{33}, c_{34},$ $c_{35}, c_{36}, c_{44}, c_{45}, c_{46}, c_{55}, c_{56}, c_{66}$

are the matrices c_{ij}. The symmetry in the crystal in reduces the number of independent c_{ij} and are summarized in Table 8.1.

Further restrictions on constants for hexagonal crystal are

$$c_{44} > 0,\ c_{11} > |c_{12}|,\ (c_{11} + c_{12})c_{33} > 2c_{13}^2$$

and for cubic crystal:

$$c_{44} > 0,\ c_{11} > |c_{12}|,\ c_{11} + 2c_{12} > 0$$

Using Voigt [189] (Reuss [190]) method we can calculate the theoretical maximum (minimum) bulk modulus ($B_{V,R}$) and shear modulus ($G_{V,R}$) of polycrystalline materials by equations:

$$\begin{aligned} B_V &= \frac{1}{9}(c_{11} + c_{22} + c_{33} + 2(c_{12} + c_{13} + c_{23}) \\ G_V &= \frac{1}{15}(c_{11} + c_{22} + c_{33} + 3(c_{44} + c_{55} + c_{66}) - c_{12} - c_{13} - c_{23}) \end{aligned} \tag{8.4}$$

and

$$
\begin{aligned}
B_R &= (s_{11} + s_{22} + s_{33} + 2(s_{12} + s_{13} + s_{23})^{-1} \\
G_R &= \frac{15}{4(s_{11} + s_{22} + s_{33} - s_{12} - s_{13} - s_{23}) + 3(s_{44} + s_{55} + s_{66})}
\end{aligned} \tag{8.5}
$$

where s_{ij} are the elastic compliance constants and they are related to c_{ij} by

$$
c = 1/s \tag{8.6}
$$

Knowing either of the tensor is possible to calculate the polycrystalline elastic moduli. Hill [191] method is defined as

$$
\begin{aligned}
B &= (B_V + B_R)/2 \\
G &= (G_R + G_V)/2
\end{aligned} \tag{8.7}
$$

and is taken for an estimation of the elastic properties. The Young's modulus (E) and Poisson ratio can then be calculated as

$$K = \frac{9BG}{3B+G} \tag{8.8}$$

$$\nu = \frac{3B-2G}{2(3B+G)} \tag{8.9}$$

It also useful to calculate the percentage of elastic anisotropy defined as

$$A_B = \frac{B_V - B_R}{B_V + B_R} \tag{8.10}$$

$$A_G = \frac{G_V - G_R}{G_V + G_R} \tag{8.11}$$

for bulk modulus and shear modulus.

Computational implementation using first principles can be obtained from total energy variation with structure distortion. We can therefore apply small strains to the equilibrium lattice, then determine the resulting change in energy and from this information deduce elastic constants. We determine the linear combinations of the elastic constants by straining the lattice vectors R according to the relation $R' = RD$ where R' is the matrix containing the components of the distorted lattice vectors and D is the symmetric distortion matrix which contains the strain components. The internal energy of a crystal under strain δ, can be Taylor expanded in powers of the strain tensor with respect to initial internal energy of the unstrained crystal in the

following way:

$$E(V,\delta) = E(V_0,0) + V_0\left(\sum_i \tau_i\xi_i\delta_i + \frac{1}{2}\sum_{ij} c_{ij}\xi_i\delta_i\xi_j\delta_j\right) + O(\delta)^3 \tag{8.12}$$

The volume of the unstrained system is denoted V_0, $E(V_0)$ being the corresponding total energy. τ_i represents an element in the stress tensor. All crystal structures considered in this chapter are hexagonal and therefore we need five different strains to determine five independent elastic constants. Hooke's law, in hexagonal structure has the form:

$$\begin{pmatrix} \sigma_1 \\ \sigma_2 \\ \sigma_3 \\ \sigma_4 \\ \sigma_5 \\ \sigma_6 \end{pmatrix} = \begin{pmatrix} c_{11} & c_{12} & c_{13} & 0 & 0 & 0 \\ c_{12} & c_{11} & c_{13} & 0 & 0 & 0 \\ c_{13} & c_{13} & c_{33} & 0 & 0 & 0 \\ 0 & 0 & 0 & c_{44} & 0 & 0 \\ 0 & 0 & 0 & 0 & c_{44} & 0 \\ 0 & 0 & 0 & 0 & 0 & c_{66} = \frac{c_{11}-c_{12}}{2} \end{pmatrix} \begin{pmatrix} \epsilon_1 \\ \epsilon_2 \\ \epsilon_3 \\ \epsilon_4 \\ \epsilon_5 \\ \epsilon_6 \end{pmatrix} \tag{8.13}$$

The distortion matrix D are written as:

$$D_1 = \begin{pmatrix} 1+\delta & 0 & 0 \\ 0 & 1+\delta & 0 \\ 0 & 0 & 1 \end{pmatrix} \tag{8.14}$$

$$D_2 = \begin{pmatrix} 1+\delta & 0 & 0 \\ 0 & 1-\delta & 0 \\ 0 & 0 & 1 \end{pmatrix} \tag{8.15}$$

$$D_3 = \begin{pmatrix} 1 & 0 & 0 \\ 0 & 1 & 0 \\ 0 & 0 & 1+\delta \end{pmatrix} \tag{8.16}$$

$$D_4 = \begin{pmatrix} 1 & 0 & \delta \\ 0 & 1 & 0 \\ \delta & 0 & 1 \end{pmatrix} \tag{8.17}$$

$$D_5 = \begin{pmatrix} 1+\delta & 0 & 0 \\ 0 & 1+\delta & 0 \\ 0 & 0 & 1+\delta \end{pmatrix} \tag{8.18}$$

and the corresponding energies are

$$E(V,\delta) = E(V_0,0) + V_0\left[(\tau_1+\tau_2)\delta + (c_{11}+c_{12})\delta^2\right] \tag{8.19}$$

$$E(V,\delta) = E(V_0,0) + V_0\left[(\tau_1-\tau_2)\delta + (c_{11}-c_{12})\delta^2\right] \tag{8.20}$$

$$E(V,\delta) = E(V_0,0) + V_0\left(\tau_3\delta + \frac{c_{33}}{2}\delta^2\right) \tag{8.21}$$

$$E(V,\delta) = E(V_0,0) + V_0\left(\tau_5\delta + 2c_{55}\delta^2\right) \tag{8.22}$$

$$E(V,\delta) = E(V_0,0) + V_0\left(\left(\tau_1+\tau_2+\tau_3\right)\delta + \frac{1}{2}\left(2c_{11}+2c_{12}+4c_{13}+c_{33}\right)\delta^2\right) \tag{8.23}$$

The total energy has been calculated for five different distortions δ =-0.04, -0.02, 0.00, 0.02 and 0.04 for everyone of the five different deformations of the lattice. By means of polynomial fits, we extract the zero-, first-, and second-order coefficients and from these we obtain $E(V_0,0), \tau_j$, and c_{ij} in equation (8.12).

The bulk modulus is defined as

$$\begin{aligned} B &= V_0\frac{d^2E}{dV^2} = \frac{1}{9V_0}\frac{d^2E}{d\delta^2} \\ &= \frac{2(c_{11}+c_{12})+4c_{13}+c_{33}}{9} \end{aligned} \tag{8.24}$$

Then Voigt and Reuss upper and lower bounds in c_{ij} becomes:

$$B_V = \frac{2(c_{11}+c_{12})+4c_{13}+c_{33}}{9} \tag{8.25}$$

$$G_V = \frac{1}{30}\left[12c_{66}+12c_{44}+c_{11}+c_{12}+2c_{33}-4c_{13}\right] \tag{8.26}$$

$$B_R = \frac{(c_{11}+c_{12})c_{33}-2c_{13}^2}{c_{11}+c_{12}+2c_{33}-4c_{13}} \tag{8.27}$$

$$G_R = \frac{5}{2}\frac{c_{44}c_{66}\left[(c_{11}+c_{12})c_{33}-2c_{13}^2\right]}{(c_{44}+c_{66})\left[(c_{11}+c_{12})c_{33}-2c_{13}^2\right]+3B_V c_{44}c_{66}} \tag{8.28}$$

8.2 Defect Structures

The perfect crystal is one of the idealizations commonly found in theoretical physics. There are various types of defects which may drastically modify properties of ultra-hard materials to make them useful in practical applications. They can also provide a useful optical and electronic properties. The fields of metallurgy, corrosion science, catalysis, phosphors, optical fibers and semiconductors are just few examples of areas where defect effects are paramount and can often be put to advantage to achieve effects which do not occur in perfect material. An understanding of defect properties thus allows many desirable materials and devices which would be unobtainable if constrained to be designed and developed in perfect systems [192].

We have intrinsic and extrinsic defects and typical intrinsic examples are vacancies,

interstitial and antisites defects. The vacancies are formed when there are missing atoms in the lattice sites which may developed in crystals as a result of irradiation or crystal growth. Interstitial defects is when the atoms are found occupying non lattice site and antisites defects are found where elements of a compound occur on the wrong location. Extrinsic defects arising from the presence of foreign atoms can take similar roles and may be coupled with intrinsic features.

Here we calculated the elastic and electronic properties of vacancies created in B_6O structure by removing one and two oxygen (O) atoms at lattice sites pointed in Figure 8.1 and the structures are in Appendix A. We also examined the carbon and nitrogen substitutional defects. In the case of substitutional we removed one O atom in the lattice site and then replace it by C atom ($B_6O_{(1C)}$) and also for two O atoms substituted by C atoms ($B_6O_{(2C)}$). We applied a similar method even in the case of nitrogen. Figure 8.1 shows point defects created in B_6O crystal structure. From this we calculated the equilibrium properties for all defect optimized crystal structures considered this Chapter.

8.3 Computational Procedure

All calculations were performed within the local density approximation (LDA) as parameterized by Perdew and Zunger [124] of density functional theory (DFT) [84] using projector augmented wave (PAW) pseudopotentials method [115] implemented through a variable-cell option of the Vienna *Ab-initio* Simulation Package (VASP)

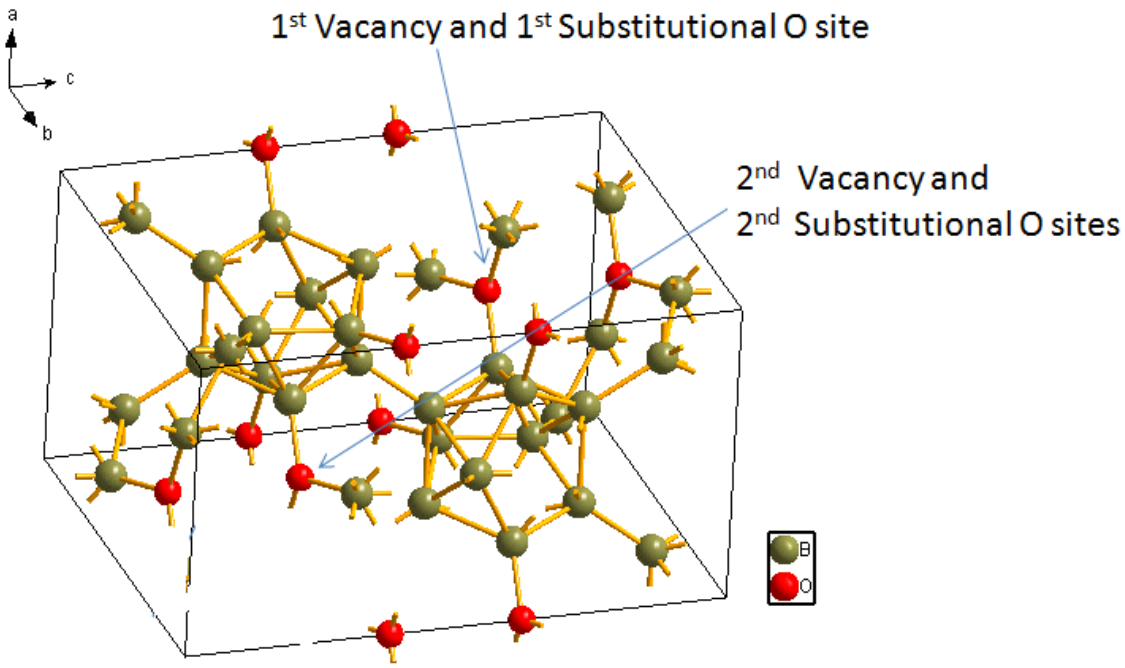


Figure 8.1: Crystal structure of B_6O and point defects created.

electronic structure [116]. and employing a plane waves basis calculated on 6×6×6 **k** points Monkhorst–Pack grid [105]. LDA usually gives a better description of the cohesive properties as well as the elastic constants, we therefore calculated hexagonal elastic constants of all defects considered here. In all cases a full geometry optimization has been performed on each of the systems with a convergence criteria of at least 10^{-6} eV/atom placed on self consistent convergence of the total energy.

8.4 Results and discussion

8.4.1 Structural properties

Firstly we calculated the total energy of ideal B_6O in order to obtain structural properties and then created substitutionals, interstitials and vacancies defect types discussed in previous section. Table 8.2 list zero pressure equilibrium lattice parameters a, c and the ratio c/a results for B_6O. The recent theoretical and experimental values are also shown for the comparison. The calculated equilibrium lattice parameters a and c values are 5.328 and 12.147 respectively for our stable B_6O structure and this corresponds to the ratio c/a of 2.280. These values agree well with both experimental and theoretical values within errors of 0.3% and 0.1% for the ratio c/a respectively.

Total volume V, bulk modulus B and pressure derivative B′at zero pressure are also listed and they are compared with the experimental and theoretical results.

Table 8.2: Theoretically determined lattice parameter of B_6O and the ratio c/a with some experimental values. Equilibrium volume, Bulk modulus and pressure derivative are presented with experimental results using equation of state.

	a ($\AA$)	c ($\AA$)	c/a	$V_{tot}(\AA^3)$	$B(GPa)$	B'
This work	5.328	12.147	2.280	299.6	246.2	3.4
Theoretical results[193]	5.331	12.124	2.274	298.4	232.7	3.5
Expt[136]	5.429	12.328	2.271	314.5	181	6.0
Expt[194]	5.414	12.386	2.288	311.5	270	1.8
				311.5	213	4
				311.5	112	1.2
				311.5	288	4
Expt[195]	5.367	12.325	2.296			
Expt[196]	5.374	12.331	2.294			
Expt[197]	5.386	12.319	2.287			

The calculated total volume is in reasonable agreement between experimental and theoretical results by 14 Å and 1 Å respectively. The bulk modulus and pressure derivatives computed by fitting the energy-volume data to Birch [132] equation of state are also shown in Table 8.2. Our calculated results are larger than the theoretical result and these may be attributed to the factors between functional used which are quite common errors for theories based on LDA and GGA.

The optimized equilibrium lattice parameters of defects considered in this work are presented in Table 8.3. To check our results we need experimental measurements or theoretical calculations. To our best knowledge no experimental and theoretical data has been reported for the defects considered here and therefore future calculations or measurements on these structures are needed to confirm our theoretical predictions. It is interesting to note that the lattice parameters for the substitutional defects

Table 8.3: Number of atoms in the unit cell, equilibrium atomic volume and lattice parameters of various Boron suboxide defects together with total energies. Bulk of the moduli and pressure derivatives were calculated using EOS

Material	N_0 atoms	V_0 (Å^3/atom)	Lattice parameter(Å)	E_{tot} (eV/atom)	$B(B')$ (GPa)
N substitutional					
$B_6O_{(1N)}$: 1N at 1O site	42	7.137	a = 5.338	-7.981	245.8
			c = 12.136		(3.4)
$B_6O_{(2N)}$: 2N at 2O sites	42	7.157	a = 5.347	-7.996	246.0
			c = 12.133		(3.4)
C substitutional					
$B_6O_{(1C)}$: 1C at 1O site	42	7.181	a = 5.356	-7.946	243.1
			c = 12.132		(3.4)
$B_6O_{(2C)}$: 2C at 2O sites	42	7.248	a = 5.384	-7.928	240.1
			c = 12.117		(3.4)
Vacancy					
$B_6O_{(1Vac)}$:	41	7.183	a = 5.281	-7.873	229.7
1 vacancy at O site			c = 12.186		(3.5)
$B_6O_{(2Vac)}$:	40	7.215	a = 5.217	-7.782	216.6
2 vacancies at 2 O sites			c = 12.234		(3.6)

($B_6O_{(1X)} = C, N$) are very close to that of B_6O. The lattice constants a's for the substitutional defects are slightly larger and for c parameters they slightly lesser compared to optimized B_6O crystal structure and also lattice parameter a increases with an additional of substitutional defect in B_6O whereas c decreases. For one vacancy created lattice parameter a decreased and while c increased. This trend is also observed with the second vacancy created. It is obviously connected to a predominant role of interatomic bonds in the defect structures.

Next, the calculated total energies, equilibrium volumes were used for estimation of bulk modulus with its pressure derivatives of the considered phases and they are all presented in Table 8.3. These results show us that the defects affect the properties

of materials by either hardening or softening them and this depends critically at the location and the type of defect. This is evident from the bulk moduli and pressure derivatives obtained in Table 8.3, for example if we replace an atom at a specific position it change the properties with the change in location. It would be very interesting create further substitutional even interstitial to note the defect types which may be responsible for the enhanced hardness. Unfortunately we could not search all the lattice sites where the minimum and maximum stiff points the defect posses because these calculations are computationally difficult given the constraints of computer memory and available execution time. For N substitutional there is no much difference in elastic properties as compared to C substitutional and vacancies. The differences in elastic properties may also be attributed to B-C and B-N interatomic bonds in the defect structures. We also note that our vacancies are having bulk moduli closer to some experimental measurements and therefore this suggest that their samples may be oxygen deficient as observed in many B_6O compounds. The presence of oxygen deficiency in the non-stoichiometry B_6O samples suggests that B_6O has vacancies. Furthermore the bulk modulus decreases with the increase in the oxygen vacancies and carbon substitution whereas in the case of nitrogen there is a slightly increase. Bulk modulus alone is insufficient to give much insight related to mechanical properties, but with the aid of elastic constants we will be able to investigate the role which these defects can display.

Table 8.4: Single crystal elastic constants of B_6O, B_6N, B_6C and some defects at zero pressure c_{ij} are in GPa. T_m is estimated melting temperature.

Compound	c_{11}	c_{12}	c_{13}	c_{33}	c_{44}	$T_m(^\circ C)$
B_6O	615.91	140.03	60.67	474.30	180.06	2640
[a]B_6O	614.99	122.22	46.51	474.12	192.29	-
[b]B_6O	586.88	133.19	47.41	443.87	-	-
B_6N	587.88	185.83	59.52	411.66	143.15	2462
B_6C	582.42	127.94	67.57	391.75	104.45	2416
$B_6O_{(1N)}$	616.72	143.11	57.23	469.83	175.18	2636
$B_6O_{(2N)}$	616.82	143.91	59.39	465.42	169.78	2630
$B_6O_{(1C)}$	609.70	139.68	57.49	469.20	168.57	2614
$B_6O_{(2C)}$	604.94	138.84	54.98	463.23	159.62	2591
$B_6O_{(1Vac)}$	545.24	127.54	61.81	486.15	180.86	2446
$B_6O_{(2Vac)}$	455.95	150.10	61.91	504.60	184.28	2206

[a]Ref[193]
[b]Ref[134]

8.4.2 Single crystal elastic parameters

Single crystal elastic constants for B_6O and defects structures considered in this work are not experimentally available and we have calculated five independent single crystal elastic constants for B_6O together with the defects and these results for the defects may serve as predictions. The single elastic constants are presented in Table 8.4 with some theoretical calculations for comparison purpose in B_6O. In line with available theoretical results we found an excellent agreement for B_6O with some constant such as c_{11} and c_{33} as in ref [193] than constants calculated by Lee [134] whereas other constants are in fair agreement at zero pressure.

Furthermore we investigated the Cauchy relationships, elastic isotropy, Poisson ratios and c_{33}/c_{11} which are essential in providing the characteristic of interatomic

bonding through single crystal elastic constants. The Cauchy relationships between the elastic stiffness constants for hexagonal solids with central forces are[198]:

$$c_{13} = c_{44}, c_{11} = 3c_{12}, or(c_{12} = c_{66}) \tag{8.29}$$

It can be seen from Table 8.4 that the Cauchy relation does not hold true for these compounds and this fact implies that the interatomic forces in boron suboxide and defects created here are non-central. And in our case the interatomic forces are increasingly non-central in the order of C, N, O for B_6X (X = C, N, O); $B_6O_{(2X)}$,$B_6O_{(1X)}$ for substitutional defect (where X = N, C) based on equation (8.29) and Table 8.4 and it may have a substantial influence on the dislocation core structure and mechanical behavior of these materials. Furthermore, Table 8.4 shows that the stiffness constants in most cases differ by a factor of 2 for example $c_{44}/c_{13} = 2.97$ in B_6O, indicating that the interatomic bonding in these systems are highly directional.

The melting temperature are closely related to their elastic constants based on the empirical formula of Fine *et al* [199] and since we are working with hexagonal structures it may be written as:

$$T_m = 354 + \frac{3}{2}(2c11 + c33) \tag{8.30}$$

where T_m is the melting temperature and the units are in Kelvins. From Table

Table 8.5: Elastic anisotropy factors and Poisson ratio of B_6O and some defects B_6O.

Compound	c_{33}/c_{11}	c_{13}/c_{12}	$2c_{44}/(c_{11}-c_{12})$
B_6O	0.77	0.43	0.76
B_6N	0.70	0.32	0.71
B_6C	0.67	0.53	0.46
$B_6O_{(1N)}$	0.76	0.40	0.74
$B_6O_{(2N)}$	0.75	0.41	0.72
$B_6O_{(1C)}$	0.77	0.41	0.72
$B_6O_{(2C)}$	0.77	0.40	0.68
$B_6O_{(1Vac)}$	0.89	0.48	0.87
$B_6O_{(2Vac)}$	1.11	0.41	1.21

8.4, the melting temperature of B_6O at zero pressure is estimated to be $2640°C$, which is higher than most boron rich solids (e.g. B_4C∼2300-2500($°C$)) and also is higher than experimental estimated value of 2436 (40) $°C$ at 5 GPa by Solovenko [200]. The low value obtained by Solovenko is also closer to that of $B_6O_{(1Vac)}$ which also implies that B_6O have vacancies. The predicted melting temperatures for the defects studied are also tabulated in Table 8.4 and their values are well below that of B_6O materials.

Table 8.5 shows the elastic anisotropy factors and this suggests that most of elastic anisotropy factors of B_6O and these defects differ substantially from unity, indicating that these compounds are significantly anisotropic in elasticity. It is generally true for hexagonal systems that a quantitative comparison between c_{11} and c_{33} may provide a qualitative comparison between the bonding strength along $\mathbf{c} = [0001]$ and the basal plane. Table 8.5 also shows that $c_{33}/c_{11} \sim 1$ for most systems implying that the atomic bonds along $\mathbf{c} = [0001]$ direction between the nearest neighbors are about the same as those along any direction in the basal plane for these systems.

Table 8.6: Elastic properties of B_6O and some defects. Hill's average bulk Modulus(B), shear modulus(G), Young modulus(K) and Poisson ratio are derived from single crystal elastic constants.

Compound	B (GPa)	G (GPa)	K (GPa)	ν	B/G
B_6O	243.75	213.05	501.39	0.16	1.14
$^aB_6O_{Theory}$	233.7	223.1	507.8	0.14	1.04
$^bB_6O_{\exp t}$	230	206	470	0.16	1.12
$^cB_6O^*_{\exp t}$	300	227	540	0.20	1.32
B_6N	236.65	178.82	439.18	0.20	1.32
B_6C	225.70	162.24	416.35	0.20	1.39
$B_6O_{(1N)}$	242.40	210.72	497.57	0.16	1.15
$B_6O_{(2N)}$	242.91	207.47	492.71	0.17	1.17
$B_6O_{(1C)}$	240.44	206.55	489.70	0.17	1.16
$B_6O_{(2C)}$	237.29	201.19	479.98	0.17	1.18
$B_6O_{(1Vac)}$	229.76	201.35	470.08	0.16	1.14
$B_6O_{(2Vac)}$	218.13	178.50	424.43	0.18	1.22

^{a}Ref[193]
^{b}Ref[170]
^{c}Ref[201]
*Hot pressed sample at 1900 ^0C

8.4.3 Polycrystalline elastic moduli

Although there are no experimental available values to compare for single elastic constants, the polycrystalline elastic moduli for B_6O have been experimentally measured and can be used to compare our calculations for B_6O. Our data for the polycrystalline elastic moduli of the defect structures may be beneficial to refer for the future investigations. We estimated the true polycrystalline elastic moduli B, G by Hill's method in equation (8.7) from equations (8.25) to (8.28). The Young's moduli and Poisson ratios are also presented from equations (8.8) and (8.9) and they are tabulated in Table 8.6.

The polycrystalline elastic moduli bulk modulus (B), shear modulus (G), and Young's modulus (K) are under zero pressure and are tabulated in Table 8.6 along with some previously published experimental results and theoretical calculations for polycrystalline B_6O materials. Table 8.6 shows that the data from this study is in agreement with available experimental results and previously published theoretical calculations for polycrystalline boron suboxide. In addition, the Poisson and B/G ratio from this study is consistent with the values of 0.16 and 1.12 respectively obtained from elastic moduli using resonant-sphere technique at ambient conditions on hot pressed B_6O specimens [170]. It can be seen from Table 8.6 that the derived elastic moduli from single crystals, B, G, and K of the defects are smaller than that of B_6O. These constants slightly decrease with the presence of defects. Another interesting quantity which is generally associated with bonding directionality and the resistance to shear is the Poisson ratio and is also given in Table 8.6. Common hexagonal solids have Poisson ratio of $\nu \sim 0.33$ and from this data the smaller values obtained in this work again indicates that the interatomic bonding in these solids is highly directional and these materials are more likely to resist shear. The elastic moduli presented in Table 8.6 may be used to classify these materials as strong solids and also suggests that the bonding strength is very high in these materials. Elastic moduli may be indicative to brittle character or ductile feature of the material using Pugh criterion [202]. Based on this criterion, the brittleness (ductility) character of the material is related to B/G ratio, if it has a low (high) value. Boron suboxide and these de-

fects have significantly smaller values than those of most solids ($B/G > 1.40$) which indicates that they may not possess promising mechanical behavior at low temperatures and since these calculations were performed at 0K, it will not be unexpected to synthesize B_6O with these defects under high pressure and temperature conditions.

Finally elastic moduli can be used to determine sound wave velocities, mean sound wave velocity and Debye temperature Θ_D. The relationship between sound wave velocity and the elastic constants are from Navier's equation [203]

$$v_L = \sqrt{\frac{B + \frac{4}{3}G}{\rho}} \tag{8.31}$$

$$v_T = \sqrt{\frac{G}{\rho}} \tag{8.32}$$

where v_L and v_T are longitudinal and transverse sound wave velocity respectively and their average can be expanded as

$$v_M = \left[\frac{1}{3}\left(\frac{2}{v_T^3} + \frac{1}{v_L^3}\right)\right]^{-\frac{1}{3}} \tag{8.33}$$

The Debye temperature Θ_D can be calculated by the following equation [204]:

$$\Theta_D = \frac{h}{k_B}\left(\frac{3N_0}{4\pi V_{tot}}\right)^{\frac{1}{3}} v_M \tag{8.34}$$

where h is Plank's constant, k_B is the Boltzmann's constant, V_{tot} the volume

Table 8.7: Percentage anisotropy of bulk (A_B), shear (A_G) . The longitudinal, transverse , mean sound velocity (v_L, v_T, v_M) and Debye temperature (Θ_D) are also presented.

Compound	A_B (%)	A_G (%)	ρ $(g.cm^{-3})$	v_T $(m.s^{-1})$	v_L $(m.s^{-1})$	v_M $(m.s^{-1})$	Θ_D (K)
B_6O	1.51	1.24	2.70	8887.76	13989.11	9772.91	1514.54
B_6N	3.16	2.32	2.60	8295.10	13520.50	9155.88	1413.17
B_6C	2.54	6.92	2.42	8176.23	13495.61	9036.24	1374.95
$B_6O_{(1N)}$	1.69	1.47	2.68	8870.99	13980.30	9755.86	1510.34
$B_6O_{(2N)}$	1.75	1.68	2.66	8832.88	13977.51	9718.45	1503.14
$B_6O_{(1C)}$	1.57	1.68	2.65	8828.06	13951.06	9711.67	1500.42
$B_6O_{(2C)}$	1.64	2.10	2.60	8789.88	13933.36	9672.99	1489.82
$B_6O_{(1Vac)}$	0.54	0.53	2.65	8722.64	13720.91	9590.69	1481.59
$B_6O_{(2Vac)}$	0.06	1.10	2.61	8272.25	13223.49	9111.80	1405.53

of unit cell and N_0 the number of atoms in unit cell. The calculated percentage anisotropy, bulk (A_B) and shear (A_G) from equations (8.10) and (8.11) are tabulated in Table 8.7. Acoustic velocity anisotropy and Debye temperatures are also estimated and they are presented in Table 8.7.

The low percentage anisotropy found in both bulk and shear modulus assumes that these materials in Table 8.7 are nearly isotropic polycrystalline materials which might be attributed to the essential common icosahedra structure found in these solids. The calculated sound wave velocities in Table 8.7 are plotted as a function of Young's modulus per density. Figure 8.2 show transverse sound wave velocity vs Young's modulus per density and this plot has a linear relation.

Figure 8.3 also indicate a longitudinal sound wave relation similar to that of transverse sound velocity meaning the acoustic wave velocity strongly depend on the Young's modulus as well as the density of material. The wave transmission will

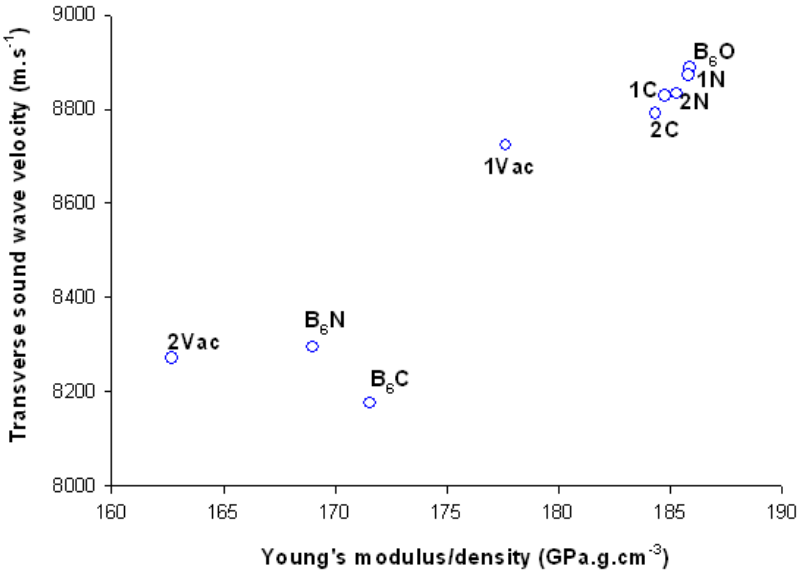


Figure 8.2: Transverse sound wave velocity vs $K\rho^{-1}$.

be slower for materials with high density. From the derived single crystal elastic constants, B_6O has large Young's modulus and its wave velocities approaches that of cBN, less to diamond and posses the highest acoustic wave velocity than most common solids and the defects considered here. We also found a reasonable Debye temperatures (Θ_D) > 1400K for these systems even for the case of vacancies.

8.4.4 Formation energies of point defects

The formation energies of defects in a compound depends on the atomic chemical potentials (μ) in the systems and μ changes depending on the chemical environment of the system. A similar formalism used for calculating surface energies [205] may be

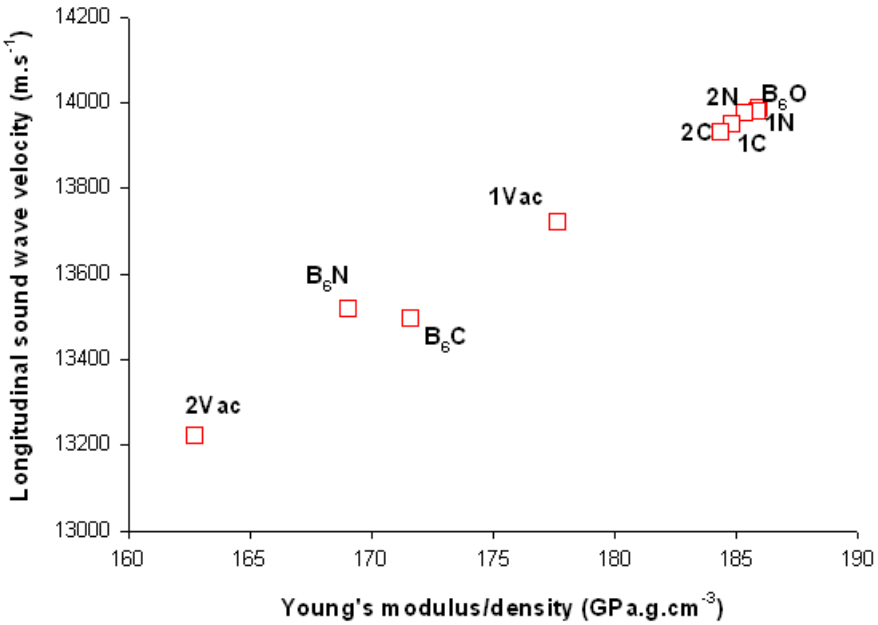


Figure 8.3: Longitudinal sound wave velocity vs $K\rho^{-1}$.

used in calculating the defect formation energies [206] and applying the same restrictions on the chemical potentials to defects in the bulk at equilibrium. In this work the defects studied have been mainly focused on point defects (vacancies, substitutional on oxygen) and in this section we are interested in their formation energies. Now if the defect X in B_6O (X =C, N) system contains excess amount of X, the excess of X may form a bulk X precipitate. Consequently, the chemical potential of X may not exceed the chemical potential of bulk X; $\mu_X \leq \mu_{X(bulk)}$. Similarly the chemical potential of B may not exceed that of bulk B; $\mu_B \leq \mu_{B(bulk)}$. The chemical potentials for the bulk substances were obtained as total energies per unit formula by separate calculation in this study, i.e. $\mu_{(bulk)} = E_{tot}(X)$. The chemical potentials

in substitutional defects in $B_6O_{1-n}X_n$ (X = C or N and $0.17 \leq x \leq 0.33$) should be correlated with each other to satisfy the following equation:

$$\mu_{B_6O_{1-n}X_n(bulk)} = 6\mu_B + (1-n)\mu_O + n\mu_X \tag{8.35}$$

The formation energies of vacancies in B_6O can be presented by

$$E_F(nOvac) = E^V_{tot}(B_6O_{(nvac)}) - E_{tot}(B_6O) + nu_O \tag{8.36}$$

where E_F is the formation energy and E^V_{tot} is the total energy of the unit cell with a defect and in generalizing for all defects it may be written as

$$E_F(X : B_6O) = E_{tot}(B_lO_mX_n) - l\mu_B - m\mu_O - n\mu_X \tag{8.37}$$

The numbers l, m, n are numbers of B, O, X atoms respectively in the unit cell. By defining

$$\Delta\mu = (\mu_B - \mu_O) - (\mu_{B(bulk)} - \mu_{O(bulk)}) \tag{8.38}$$

Then equation (8.37) may be written as

$$E_F(X : B_6O) = E^{'}_{tot}(B_lO_mX_n) - \frac{1}{2}(\mu_B - \mu_O)\Delta\mu \tag{8.39}$$

Table 8.8: Total energies and chemical potentials calculated using B_{12}.

	E_{tot} (eV/atom)	Bulk	E_{tot} (eV/atom)	chemical potentials from α−B_{12}(eV/atom)	E (eV/atom)
B_6O	-7.966	B_{12}(bulk)	-7.468	$\mu_{O(B_6O)}$	-10.953
B_6N	-8.080			1:$\mu_{C(B_4C)(\text{chain})}$	-10.290
B_6C	-7.850			2:$\mu_{C(B_6C)}$	-10.142
B_4C chain	-8.033			3:$\mu_{C(B_4C)(\text{polar})}$	-8.950
B_4C polar	-7.765			1:$\mu_{N(B_4N)(\text{chain})}$	-9.101
B_4N chain	-7.795			2:$\mu_{N(B_6N)}$	-11.747
B_4N polar	-7.610			3:$\mu_{N(B_4N)(\text{polar})}$	-8.175

where $E^{'}_{tot}(B_lO_mX_n)$ is independent of $\Delta\mu$. For perfect a crystal $E^{'}_{tot}(B_lO_mX_n) = 0$, and the formation energy vanishes. The restriction on chemical potentials are

$$-\Delta H \leq \Delta\mu \leq \Delta H \tag{8.40}$$

where $\Delta H = -(\mu_{B_6O} - 6\mu_{B(bulk)} - \mu_{O(bulk)})$ is the heat of formation of B_6O. Most calculations always neglect the temperature dependence of total energies and heat of formations, although the dependence may be important in obtaining accurate defect concentrations for high temperatures[207]. The energetically most favorable form of the neutral defect is the one that gives the lowest formation energy since the probability of finding the defect at temperature T is proportional to exp(-E_F/k_BT).

The total energies and chemical potentials calculated for several defect structures are listed in Table (8.8). The total energies were obtained by optimizing the defect structures. These results were obtained from equation of state fits of energy-volume data which we used to obtain bulk modulus, and pressure derivatives. We used total

Table 8.9: Formation energies from chemical potentials.

	1:E_F (eV)	2:E_F (eV)	3:E_F (eV)
$B_6O_{(1C)}$	0.176	0.029	-1.164
$B_6O_{(2C)}$	0.284	-0.012	-2.397
$B_6O_{(1N)}$	-2.463	0.183	-3.388
$B_6O_{(2N)}$	-4.971	0.320	-6.822
$B_6O_{(1Vac)}$	0.831	-	-
$B_6O_{(2Vac)}$	1.394	-	-

energies obtained in Table (8.8) to calculate chemical potentials for all the defects in order to obtain formation energies. For nitrogen and carbon chemical potentials we have chosen our previous calculated results of nitrides and carbides materials listed in Table (8.8) and therefore we calculated three possible values for chemical potentials ($1\mu, 2\mu$, and 3μ.). The chemical potential of boron $\mu_{B_{12}}$ was obtained from that of $\alpha-$boron phase that has been recently considered to be a stable prototype of boron [208] and therefore this value was used throughout to calculate chemical potentials for carbon, nitrogen and oxygen and also formation energies.

Calculated theoretical formation energies of the point defects considered in this work are tabulated in Table (8.9). The vacancy formation energies on the $B_6O_{(1Vac)}$ vacancy and $B_6O_{(2Vac)}$ vacancies are found to be 0.831 eV and 1.394 eV respectively. These formation energies are higher than the substitutional formation energies of both carbon and nitrogen. The formation energies of substitutional nitrogen to oxygen are smaller than those of carbon substitution to oxygen. The low values of nitrogen substitutional indicate a possible great solubility of nitrogen in B_6O. The negative

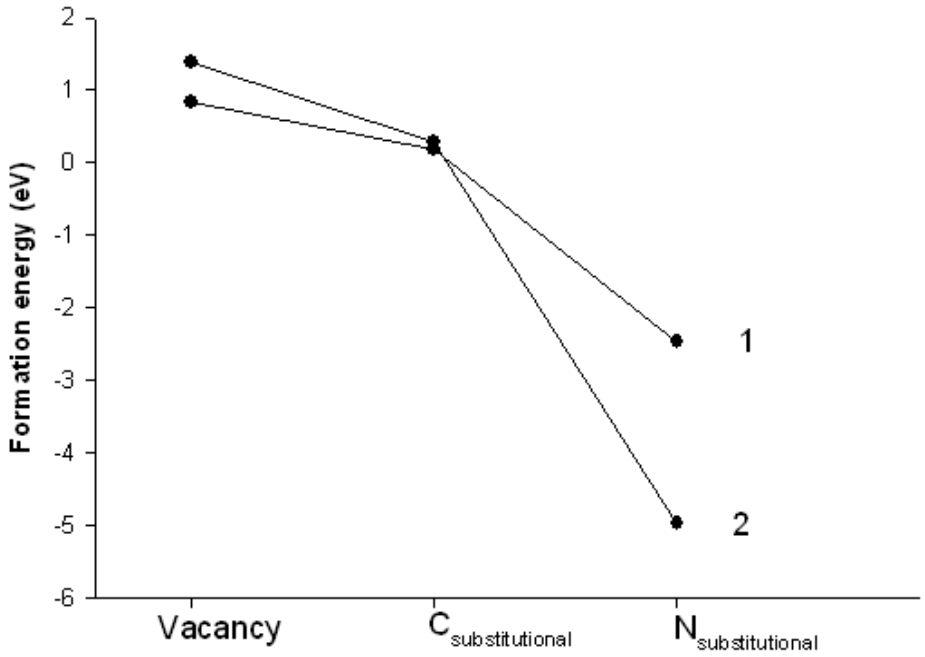


Figure 8.4: Formation energies of vacancies and substitutional carbon and nitrogen

formation energies also indicate that it is energetically favorable to form the stable phase. The obtained formation energies are also plotted in Figure 8.4. Figure 8.4 show vacancies that has the least influence on B_6O than substitutional defects while nitrogen substitutional may be easily generated. It is unfortunate that there are no theoretical or experimental formation energies of these defects available to compare with our data and therefore these calculations may be used as guide in determining defect properties in B_6O. It is stressed that such values are difficult to estimate however the low values especially for O vacancies, do indicate the ease of such defects can be produced in the material.

8.5 Summary

In summary, in this Chapter we presented the elastic properties of boron suboxide and also of the defect structures created in this work using first-principle calculations. These calculations have been performed to understand the structural, elastic properties and formation energies of the defects in B_6O and to provide an insight into the fundamental properties of some defects in ultra hard materials. The equilibrium lattice parameters, volumes, elastic properties using equation of state and single crystal elastic constants and polycrystalline elastic moduli for B_6O and some defects created in this work are accurately calculated within LDA of DFT through *ab initio* approach and they are in good agreement with available theoretical calculations and experimental results. From the calculated single crystal elastic constants at zero pressure, melting temperatures, elastic anisotropy factors, acoustic velocities, Cauchy relations, Poisson ratios and Debye temperatures are estimated. Cauchy relations do not true for these systems and the interatomic forces are non central. The low Poisson ratio value of 0.16 for B_6O is obtained and is consistent with previous theoretical and experimental studies. The Debye temperatures estimated in this work are greater that 1400K. These values are found to be much higher that most common solids.

The formation energies of the defect structures are also predicted. These formation energies are estimated for the first time using chemical potentials obtained from different possible carbide and nitride structures. The results show that nitrogen substitution to oxygen in B_6O is more favorable in comparison to that of carbon. In

addition, taking into account the positive values of vacancy formation energies, the important role of a process to synthesize B_6O with vacancies should be very likely. The understanding of the possible reasons of the formation of some point defects in B_6O and explaining of the influence of some defects on the physical and chemical properties of ultra hard boride materials seems very interesting. O vacancies and substitutional C and N essentially make the B_6O structure less hard and play an important role in weakening the strength of B_6O. We have also suggested that O vacancies play an important role in influencing thermal properties of B_6O such as the Debye and melting temperatures.

Chapter 9

Conclusion

We have used an *ab initio* computational modelling to investigate properties of potentially ultra-hard boride materials. We presented both LDA and GGA calculations, and as usual GGA underestimated the bulk modulus. The boron icosahedra and how it is connected has been shown to play a critical role in the properties of several boride materials. Connectivity in these materials is quite complex involving connection geometries and atomic types that differ from one material to another. The preferred links between icosahedra occur as rigid covalent bonds, directed radially outwards from each vertex. In tetragonal boron additional elements such as nitrogen or carbon can stabilize the unit cell by providing deficit electrons. The rhombohedral structures resemble that of semiconductors from calculated density of states.

This work has also shown that often there is no direct covalent bonding between the chemical atoms and suggests that the additional chemical atoms are influencing

the boron bonding differently in each material. Subtle changes are found that can be quantified by average charge density on differently B-B bonds. Although trends such as volume changes and bulk modulus do exhibit a similar variation to the measured hardness of the materials there is low bulk modulus for the $MgAlB_{14}$. It is found that in this material there is a quite larger changes in B-B bonding. This we suggest that the extend of B-B bonding in the boride structures and how it is affected by additional atoms holding these structures together is guide to the extend of hardness in these important class of novel hard materials.

We also investigated some properties of selected boron rich compounds with the composition of B_6X (X=C, N, O) and they are consistent with other hard materials. The calculated properties compares well with experiment and available data from other calculations. These materials have high bulk modulus with trends established from the effects of the atomic volumes of the additional elements in the icosahedra and bulk modulus. Since hard materials are also associated with bulk modulus and other factors, we conclude that our calculations predict ultra-hard materials for B_6X (X=C, N, O) compounds. Further investigations into these compounds would elucidate electronic, magnetic and mechanical properties with possible applications imposed by technological requirements.

We also calculated the structural and thermodynamic properties of boron icosahedral structures using molecular dynamics simulations. The Tersoff parameters used are reliable to investigate the structural and thermodynamics properties of boron

icosahedral studied here and we suggest that with proper adjustment of the parameters they can be used to give much insight of these complex structures. Lattice parameters, bulk modulus and are in fair agreement with other calculations for some of our structures. We also predicted thermodynamic properties such as specific heat, linear thermal expansion coefficient and B_4C and B_6O structures obey the classical Dulong-Petit result which is obtained at high temperatures for all solids.

Finally we predicted the elastic constants of an ultra hard boride B_6O and some defects in the crystal structure. The calculated single crystal elastic constants to were estimated polycrystalline properties and thermodynamic properties such as the melting and Debye temperatures as well as sound wave velocities in these structures. We also estimated the formation energies of the various structures from chemical potentials.

Bibliography

[1] C. Sung, M. Sung, *Materials Chemistry and Physics* **43**, 1 (1996).

[2] A. Zerr, R. Riedel, *Novel Ultrahard Materials, In Handbook of ceramic hard materials*, vol. 1 (Wiley-VCH Verlag, 2000).

[3] J. Qin, *et al.*, *Advanced Materials* **20**, 4780 (2008).

[4] B. J. Cullen, *United States Patent* **US 6 605 798 B1** (1999).

[5] R. K. Bogdanov, A. A. Shulzhenko, A. P. Zakora, A. M. Isonkin, V. G. Gargin, *Journal of Superhard Materials* **29**, 56 (2007).

[6] V. V. Brazhkin, A. Lyapin, R. Hemley, *Philosophical Magazine A* **82**, 231 (2002).

[7] S. Zhang, H. Li, H. Li, S. Zhou, X. Cao, *J. Phys. Chem. B* **111**, 1304 (2007).

[8] M. L. Cohen, *Physcal Review B* **32**, 7988 (1985).

[9] M. L. Cohen, *Science* **261**, 307 (1993).

[10] A. Kelly, *Strong Solids* (Oxford University Press, 1973).

[11] B. R. Wu, C. M. Sung, S. L. Lee, M. F. Tai, *Chinesse Journal of Physics* **40**, 187 (2002).

[12] F. M. Mmethi, J. E. Lowther, *High Pressure Research* **29**, 212 (2009).

[13] J. E. Lowther, O. U. Okeke, *Patent Cooperation Treaty* **WO 2009/112934 A2** (2009).

[14] M. Mattesini, S. F. Matar, *International Journal of Inorganic Materials* **3**, 943 (2001).

[15] R. Weihrich, S. F. Matar, E. Betranhandy, *Jounal of Physics and Chemistry of Solids* **64**, 1539 (2003).

[16] S. Chen, X. G. Gong, *Physical Review Letters* **98**, 015502 (2007).

[17] B. A. Cook, J. E. Snyder, A. P. Constant, Y. Tian, *US Patent* **US 7 375 343 B1** (2008).

[18] T. L. Aselage, D. R. Tallant, *Physical Review B* **57**, 2675 (1998).

[19] N. Vast, *et al.*, *Physical Review Letters* **78**, 693 (1997).

[20] K. Shirai, *Physical Review B* **55**, 12235 (1997).

[21] J. L. He, E. D. Wu, H. T. Wang, R. Liu, Y. Tian, *Physical Review Letters* **94**, 015504 (2005).

[22] T. Lundstom, Y. G. Andreev, *Materials Science and Engineering A* **209**, 16 (1996).

[23] Y. Tian, *et al.*, *Applied Physics Letters* **83**, 2781 (2003).

[24] B. A. Cook, J. L. Harringa, T. L. Lewis, A. M. Russell, *Scripta Materialia* **42**, 597 (2000).

[25] H. Hubert, *et al.*, *Nature* **391**, 376 (1998).

[26] V. Adasch, K. U.Hess, T. Ludwing, N. Vojteer, H. Hillebrecht, *Chemistry European Journal* **13**, 3450 (2007).

[27] I. J. McColm, *Ceramic Hardness* (Plenum Press, 1990).

[28] A. Zerr, *et al.*, *Advanced Materials* **18**, 2933 (2006).

[29] J. E. Lowther, *Journal of Physics: Condensed Matter* **17**, 3221 (2005).

[30] M. P. Allen, D. J. Tildesley, *Computer Simulation of Liquids* (Oxford University Press, 1987).

[31] D. W. Heermann, *Computer Simulation Methods in Theoretical Physics* (Springer- Verlag, 1990), second edn.

[32] G. Samsonov, *Handbook of the physicochemical properties of the elements* (IFI-Plenum, New York, USA, 1968).

[33] F. Knoop, C. Peters, W. Emerson, *Journal of Research of the National Bureau of Standards* **23**, 39 (1939).

[34] V. L. Solozhenko, O. O. Kurakenvych, D. Andrault, Y. L. Godec, M. Mezouar, *Physcal Review Letters* **102**, 015506 (2009).

[35] D. W. He, *et al.*, *Applied Physics Letters* **81**, 643 (2002).

[36] N. V. Novikov, S. N. Dib, *Journal of hard materials* **2**, 3 (1991).

[37] S. M. Aouadi, *Journal of Applied Physics* **99**, 053507 (2006).

[38] R. L. Smith, G. E. Sandland, *Proceedings of the Institution of Mechanical Engineers* **1**, 623 (1922).

[39] K. Kubmaul, *Lexikon Werstofftechnik* (VDI Dusseldorf, 1991).

[40] D. Teter, R. Hemley, *Science* **271**, 53 (1996).

[41] D. . M. Teter, *MRS Bulletin* **23**, 22 (1998).

[42] D. E. Garrett, *Borates: handbook of deposits, processing, properties, and use* (Academic Press, San Diego, C A, 1998).

[43] P. J. V. der Put, *The Inorganic Chemistry of Materials* (Springer, 1998).

[44] E. Wiberg, A. F. Holleman, *Inorganic Chemistry* (Elsevier, 2001).

[45] T. Lundstrom, *Journal of Solid State Chemistry* **133**, 88 (1997).

[46] M. M. Schwartz, *Encyclopedia of Materials, Parts and Finishes* (CRC Press, 2002).

[47] J. L. Hoard, R. E. Hughes, D. E. Sands, *Journal of the American Chemical Society* **80**, 4507 (1958).

[48] D. W. Bullett, *Journal of Physics C: Solid State Physics* **15**, 415 (1982).

[49] V. Adasch, K. U. Hess, T. Ludwing, N. Vijteer, H. Hillebrecht, *Journal of Solid State Chemistry* **179**, 2150 (2006).

[50] S. Lee, D. M. Bylander, S. W. Kim, Kleinman, *Physical Review B* **45**, 3248 (1992).

[51] R. J. Nelmes, *et al.*, *Physical Review Letters* **74**, 2268 (1995).

[52] F. Gao, *et al.*, *Journal of Physical Chemistry B* **109**, 14892 (2005).

[53] Y. Feng, G. T. Seidler, J. O. Cross, A. T. Macrander, J. J. Rehr, *Physical Review B* **69**, 125402 (2004).

[54] H. Werheit, *et al.*, *Journal of Alloys and Compounds* **202**, 269 (1993).

[55] J. M. Hill, D. C. Johnston, B. A. Cook, J. L. Harringa, A. M. Russell, *Journal of Magnetism and Magnetic Materials* **265**, 23 (2003).

[56] J. E. Lowther, *Physica B* **322**, 173 (2002).

[57] S. Okada, *et al.*, *Journal of the European Ceramic Society* **26**, 631 (2006).

[58] T. Ito, I. Higashi, *Acta Cryst B* **39**, 239 (1983).

[59] S. Okada, *et al.*, *Journal of Alloy and Compounds* **395**, 231 (2005).

[60] A. Masago, K. Shirai, H. Katayama-Yoshida, *Physical Review B* **73**, 104102 (2006).

[61] N. Vast, *et al.*, *Physicah Review Letters* **78**, 693 (1997).

[62] M. Cao, J. Jiang, H. Liu, J. Yuan, *Journal of Electroceramics* **17**, 817 (2006).

[63] H. Hubert, *et al.*, *Chemistry Materials* **10**, 1530 (1998).

[64] I. A. Bairamashvili, *et al.*, *Journal of the Less Common Metals* **67**, 455 (1979).

[65] D. Li, W. Y. Ching, *Physcal Review B* **54**, 1451 (1996).

[66] T. E. Letsoalo, J. E. Lowther, *Physica B* **403**, 2760 (2008).

[67] D. Music, U. Kreissig, V. Chirita, J. M. Scheneider, U. Helmersson, *Journal of Applied Physics* **93**, 940 (2003).

[68] Y. Lee, First principles calculations for x-ray resonant spectra and elastic properties, Ph.D. thesis, Iowa State University (2004).

[69] V. Kulikovsky, *et al.*, *Diamond and Related Materials* **18**, 27 (2009).

[70] K. Ploog, P. Rauh, W. Stoeger, H. Schmidt, *Journal of Crystal Growth* **13**, 350 (1972).

[71] K. Ploog, H. Schmidt, E. Amberger, G. Will, K. H. Kossobutzki, *Journal of the Less Common Metals* **29**, 161 (1972).

[72] H. Saitoh, K. Yoshida, W. A. Yarbrough, *J. Mater. Res.* **8**, 8 (1993).

[73] I. O. Kayhan, O. T. Inal, *Journal of Materials Science* **34**, 4105 (1999).

[74] B. A. Cook, *et al.* **US 2005/0100748 A1** (2005).

[75] R. Cheruhuri, M. Womack, P. Molian, A. Russell, Y. Tian, *Surface and Coatings Technology* **155**, 112 (2002).

[76] M. Born, J. R. Oppenheimer, *Ann. Physik* **84**, 457 (1927).

[77] R. A. Broglia, G. Colo, G. Onida, H. E. Roman, *Solid State Physics of Finte Systems Metal Clusters, Fullerenes, Atomic Wires* (Springer, 2004).

[78] L. Szasz, *The Electronic Structure of Atoms* (John Wiley and Sons, Inc, 1992).

[79] D. R. Hartree, *Proc. Cambridge Phil. Soc* **24**, 89 (1928).

[80] V. Fock, *Z. Phys* **61**, 126 (1930).

[81] R. M. Martin, *Electronic Structure Basic Theory and Practical Methods* (Cambridge University Press, 2004).

[82] C. Møller, M. S. Plesset, *Physical Reveiw* **46**, 618 (1934).

[83] W. Koch, M. Holthausen, *A Chemist's Guide to Density Funtional Theory* (Wiley-VCH, 2001), second edn.

[84] D. Joubert, *Density Functional Theory: Theory and Applications* (Springer, 1998).

[85] R. G. Parr, W. Wang, *Density-Functional Theory of Atoms and Molecules* (Oxford University Press, 1989).

[86] P. Hohenberg, W. Kohn, *Physical Review* **136**, B864 (1964).

[87] W. Kohn, L. J. Sham, *Physical Review* **140**, A1133 (1965).

[88] M. Levy, J. P. Perdew, *Density Functional Methods in Physics* (Plenum New York, 1985).

[89] E. Lieb, *Density Functional Methods in Physics* (Plenum, New York, 1985).

[90] A. Gorling, *Physical Review A* **47**, 2783 (1993).

[91] D. M. Ceperley, B. J. Alder, *Physical Review Letters* **45**, 566 (1980).

[92] J. Hafner, *Acta Material* **48**, 71 (2000).

[93] J. P. Perdew, *et al.*, *Physical Review B* **46**, 6671 (1992).

[94] E. Hult, Y. Andersson, B. I. Lundqvist, *Physical Review Letters* **77**, 2029 (1996).

[95] W. Kohn, Y. Meir, D. E. Makarov, *Physical Review Letters* **80**, 4153 (1998).

[96] J. P. Perdew, K. Burke, M. Ernzerhof, *Physical Review Letters* **77**, 3865 (1996).

[97] J. P. Perdew, K. Burke, M. Ernzerhof, *Physical Review Letters* **78**, 1396(E) (1997).

[98] A. D. Becke, *Physical Review A* **38**, 3098 (1988).

[99] C. Lee, W. Yang, R. G. Parr, *Physical Review B* **37**, 785 (1988).

[100] A. D. Becke, *Journal of Chemical Physics* **84**, 4524 (1986).

[101] W. A. Harris, *Pseudopotentials in the Theory of Metals* (Benjamin, New York, 1966).

[102] N. W. Ashcroft, *Solid State Physics* (Holt, Rinehart and Winston, 1976).

[103] D. Singh, L. Nordstrom, *Planewaves, Pseudopotentials and the LAPW Method* (Springer Science +Business Media, Inc, 2006).

[104] M. Payne, M. P. Teter, D. C. Allan, T. A. Arias, J. D. Joannopoulos, *Reviews of Modern Physics* **64**, 1045 (1992).

[105] H. J. Monkhorst, J. D. Pack, *Physical Review B* **13**, 5188 (1976).

[106] M. L. Cohen, V. Heine, *Solid State Physics* (Academic, New York, 1970).

[107] J. C. Phillips, *Physical Review* **112**, 685 (1958).

[108] M. D. Segall, *et al.*, *Journal of Physics: Condensed Matter* **14**, 2717 (2002).

[109] J. Crain, S. J. Clark, *Calculation of Structure and Dynamic Properties of Liquid Crystal Molecules in Liquid Crystals* (Springer Verlag, Berlin, 1999).

[110] D. G. Pettifor, *Bonding and Structure of Molecules and Solids* (Oxford University Press, 1995).

[111] G. Brocks, *Theoretical Chemistry Accounts* **104**, 116 (1999).

[112] R. Car, M. Parrinello, *Physical Review Letters* **55**, 2471 (1985).

[113] N. A. W. Holzwarth, G. E. Matthews, A. R. Tackett, R. B.Dunning, *Physical Review B* **55**, 2005 (1997).

[114] P. E. Blöchl, *Physical Review B* **50**, 17953 (1994).

[115] G. Kresse, D. Joubert, *Physical Review B* **59**, 1758 (1999).

[116] G. Kresse, J. Hafner, *Physical Review B* **49**, 14251 (1994).

[117] G. Kresse, J. Hafner, *Physical Review B* **47**, 558 (1993).

[118] G. Kresse, J. Furthmuller, *Physical Review B* **54**, 11169 (1996).

[119] G. Kresse, J. Furthmuller, *Computational Materials Science* **6**, 15 (1996).

[120] D. M. Teter, M. C. Payne, D. C. Allan, *Physical Review B* **40**, 12255 (1989).

[121] E. R. Davidson, *Methods in Computational Molecular Physics* (Plenum, New York, 1983).

[122] D. M. Wood, A. Zunger, *Journal of Physics A: Mathematical and General* **18**, 1343 (1985).

[123] K. Laasonen, A. Pasquarello, C. Lee, R. Car, D. Vanderbilt, *Physcal Review B* **47**, 10142 (1993).

[124] J. P. Perdew, A. Zunger, *Physical Review B* **23**, 5048 (1981).

[125] H. K. Clark, J. L. Hoard, *Journal of American Chemical Society* **65**, 2115 (1943).

[126] R. W. G. Wykoff, *The Structure of Crystals* (Interscience, New York, 1948).

[127] M. Olofsson, T. Lundstrom, *Journal of Alloy and Compounds* **257**, 91 (1997).

[128] M. Kobayashi, I. Higashi, C. Brodhag, F. Thevenot, *Journal of Materials Science* **28**, 2129 (1993).

[129] I. Higashi, T. Ito, *Journal of Less Common Metals* **92**, 239 (1983).

[130] P. Vinet, J. H. Rose, J. Ferrante, J. R. Smith, *Journal of Physics: Condensed Matter* **1**, 1941 (1989).

[131] F. D. Murnaghan, *American Journal of Mathematics* **49**, 235 (1937).

[132] F. Birch, *Physical Review* **71**, 809 (1947).

[133] Y. Lee, B. N. Harmon, *Journal of Alloy and Compounds* **338**, 242 (2002).

[134] S. Lee, D. M. Bylander, L. Kleinmann, *Physical Review B* **45**, 3245 (1992).

[135] X. Guo, *et al.*, *Physical Review B* **73**, 104115 (2006).

[136] D. Nieto-Sanz, P. Loubeyre, W. Crichton, M. Mezouar, *Physcal Review B* **70**, 214108 (2004).

[137] *http://britleyspears.ac/physics/dos/dos.htm* .

[138] J. B. Condon, C. E. Holocombe, D. H. Johnson, L. M. Steckel, *Inorganic Chemistry* **15**, 2173 (1976).

[139] L. A. J. Garvie, H. Hubert, W. T. Petuskey, P. F. McMillan, P. Buseck, *Journal of Solid State Chemistry* **133**, 365 (1997).

[140] H. Hubert, L. A. J. Garvie, P. R. Buseck, W. T. Petuskey, P. F. McMillan, *Journal of Solid State Chemistry* **133**, 356 (1997).

[141] H. Gou, J. Zhang, F. Gou, *Jounal of Physics: Condensed Matter* **20**, 505211 (2008).

[142] M. P. Allen, D. J. Tildesley, *Computer Simulation in Chemical Physics* (Kluwer Academic Publishers, 1993).

[143] J. M. Thijssen, *Computational Physics* (Cambridge University Press, 1999), first edn.

[144] J. P. Hansen, I. R. MacDonald, *Theory of Simple Liquids* (Academic Press, 1986).

[145] H. Goldstein, *Classical Mechanics* (Addison Wesley, 1980).

[146] D. Frenkel, B. Smit, *Understanding Molecular Simulation* (Academic Press, 2002).

[147] D. C. Rapaport, *The Art of Molecular Dynamics Simulation* (Cambridge University Press, 2004).

[148] F. J. Vesely, *Computational Physics an Introduction* (Plenum Press, 1994).

[149] A. M. Mehlape, Computer modelling of transition metal sulphide, Master's thesis, University of Limpopo (2007).

[150] J. M. Holender, *Physcal Review B* **41**, 8054 (1990).

[151] D. J. Evans, G. P. Morriss, *Statistical Mechanics of Nonequilibrium Liquids* (Academic Press, 1990).

[152] de Groot, Mazur, *Nonequilibrium Thermodynamics* (Dover, 1984).

[153] W. G. Hoover, *Computational Statistical Mechanics* (Elservier, 1991).

[154] D. W. Brenner, *Physcal Review B* **42**, 9458 (1990).

[155] A. E. Carlsson, *Solid State Physics* **43**, 1 (1990).

[156] J. Tersoff, *Physcal Review B* **37**, 6991 (1988).

[157] J. Tersoff, *Physcal Review B* **38**, 9902 (1988).

[158] J. Tersoff, *Physcal Review Letters* **61**, 2879 (1988).

[159] J. Tersoff, *Physcal Review B* **39**, 5566 (1989).

[160] W. Sekkal, B. Bouhafs, H. Aourag, M. Certier, *Jounal of Physics: Condensed Matter* **10**, 4975 (1998).

[161] K. Matsunaga, C. Fisher, H. Matsubara, *Japanese Journal of Applied Physics* **39**, 48 (2000).

[162] W. Sekkal, A. Zaoui, A. Leref, H. Aourag, M. Certier, *Journal of Physics: Condensed Matter* **11**, 3875 (1999).

[163] S. Munetoh, T. Motooka, K. Moriguchi, A. Shintani, *Computational Materials Science* **39**, 334 (2007).

[164] W. Smith, T. Forester, *Jounal of Molecular Graphics* **14**, 136 (1996).

[165] J. Gale, *Journal of the Chemical Society, Faraday Transactions* **1**, 629 (1997).

[166] J. F. Nye, *Physical Properties of Crystals* (Oxford University Press, 1957).

[167] K. J. McClellan, F. Chu, J. M. Roper, I. Shingo, *Journal of Materials Science* **36**, 3403 (2001).

[168] S. P. Dodd, G. A. Saunders, B. James, *Journal of Materials Science* **37**, 2731 (2002).

[169] Y. P. Lu, D. W. He, *Jounal of Applied Physics* **105**, 083540 (2009).

[170] D. R. Petrak, R. Hu, G. Atkins, *American Ceramic Society Bulletin* **53**, 569 (1974).

[171] B. F. Deker, J. S. Kasper, *Acta Crystallograhy* **12**, 503 (1959).

[172] R. J. Nelmes, *et al.*, *Physcal Review B* **47**, 1993 (1993).

[173] E. T. Chen, R. N. Barnett, U. Landman, *Physcal Review B* **41**, 439 (1990).

[174] D. C. Wallance, *Thermodynamics of Crystals* (John Wiley and Sons, Inc, 1972).

[175] G. A. Slack, D. W. Oliver, F. H. Horn, *Physcal Review B* **4**, 1714 (1971).

[176] A. T. Petit, P. L. Dulong, *Annals of Philosophy* **14**, 189 (1819).

[177] H. O. Pierson, *Handbook of Carbon, Graphite, Diamond and Fullerenes: Properties, Processing and Appilcations* (Noyes Publications, 1993).

[178] R. R. Reeber, K. Wang, *Journal of Electronic Materials* **25**, 63 (1996).

[179] W. H. Moon, H. J. Hwang, *Applied Surface Science* **239**, 376 (2005).

[180] L. I. Berger, *Semiconductor Materials* (CRC Press, 1996).

[181] V. E. Lyusternic, V. L. Solozhenko, *Russian Journal of Physical Chemistry* **66**, 629 (1992).

[182] G. A. Slack, S. F. Bartram, *Jounal of Applied Physics* **46**, 89 (1975).

[183] D. GERLICH, *J. Phys. Chem. Solids* **35**, 1026 (1974).

[184] Y. Guo, X. Song, X. Li, X. Yang, *Solid State Communications* **141**, 577 (2007).

[185] T. C. Shabalala, The preparation and characterization of boron suboxide base composites, Ph.D. thesis, University of the Witwatersrand, Johannesburg (2007).

[186] S. Gravett, Elastic properties of glasses and glass ceramics at high pressure and high temperature, Master's thesis, University of the Witwatersrand, Johannesburg (1989).

[187] H. A. Sidek, G. A. Saunders, R. N. Draper, B. Bridge, *Philosophical Magazine Letters* **57**, 1 (1988).

[188] P. W. McMillan, *Glass Ceramics* (Academic Press, London, 1979).

[189] W. Voigt, *Lehrbush der Kristallphysik* (Taubner, Leipzig, 1928).

[190] A. Reuss, Z. Angew, *Math. Mech* **8**, 55 (1929).

[191] R. Hill, *Proc. Phys. Soc. London* **65**, 350 (1952).

[192] F. Agullo-Lopez, R. C. A. Catlow, P. D. Townsend, *Point Defects in Materials* (Academic Press Limited, 1988).

[193] Y. P. Lu, D. W. He, *Jounal of Applied Physics* **105**, 083540 (2009).

[194] D. He, S. R. Shieh, T. S. Duffy, *Physical Review B* **70**, 184121 (2004).

[195] K. Kodou, S. Okada, K. H. and, *Kanagawa Daigaku Kogaku Kenkyusho Shoho* **19**, 60 (1996).

[196] I. Higashi, M. Kobayashi, J. Bernard, C. Brodhag, F. Thevenot, *AIP Conf. Proc.* **231**, 201 (1991).

[197] H. Bolmgren, T. Lundstom, S. Okada, *AIP Conf. Proc.* **231**, 197 (1991).

[198] F. Chu, M. Lei, S. A. Maloy, J. J. Petrovic, T. E. Mitchell, *Acta Materialia* **44**, 3045 (1996).

[199] M. E. Fine, L. D. Browna, H. L. Marcusa, *Scripta Metallurgica* **18**, 951 (1984).

[200] V. L. Solozhenko, O. O. Kurakevych, V. Z. Turkevich, D. V. Turkevich, *J. Phys. Chem. B* **112**, 6683 (2008).

[201] T. C. Shabalala, D. S. McLachlan, I. Sigalas, H. Herrmann, *Ceramic International* **34**, 1713 (2008).

[202] S. F. Pugh, *Philosophical Magazine* **45**, 822 (1954).

[203] E. Schreiber, O. L. Anderson, N. Soga, *Elastic Constants and their Measurements* (McGraw-Hill, New York, 1973).

[204] O. L. Anderson, *J. Phys. Chem. Solids* **24**, 909 (1963).

[205] G. X. Qian, R. M. Martin, D. J. Chadi, *Physcal Review B* **38**, 7649 (1988).

[206] S. B. Zhang, J. E. Northrup, *Physical Reveiw Letters* **67**, 2339 (1991).

[207] T. E. Mosuang, Defect and defect processes in some ultra-hard nitrides, Ph.D. thesis, University of the Witwatersrand, Johannesburg (2003).

[208] V. I. Ivashchenko, V. I. Schevchenko, P. E. Turchi, *Physical Reveiw* **80**, 235208 (2009).

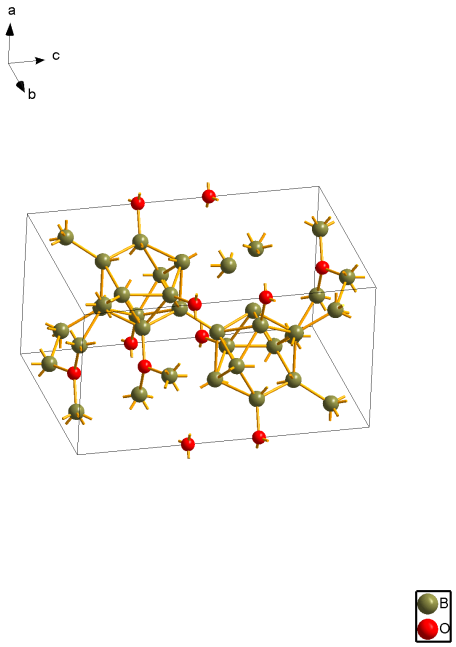


Figure 9.1: Crystal structure of B_6O with one vacancy at O site

Appendix A

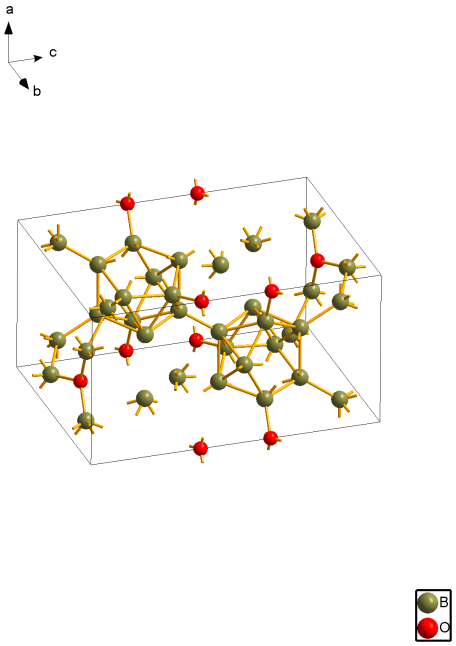


Figure 9.2: Crystal structure of B_6O with two vacancies at O sites.

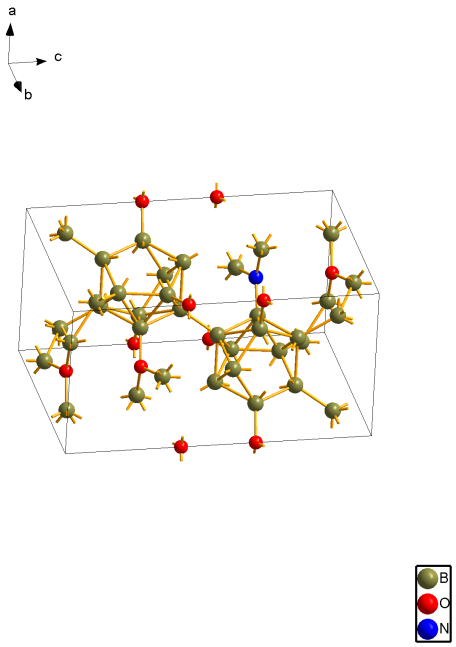


Figure 9.3: Crystal structure of B_6O with one N substituting O atom.

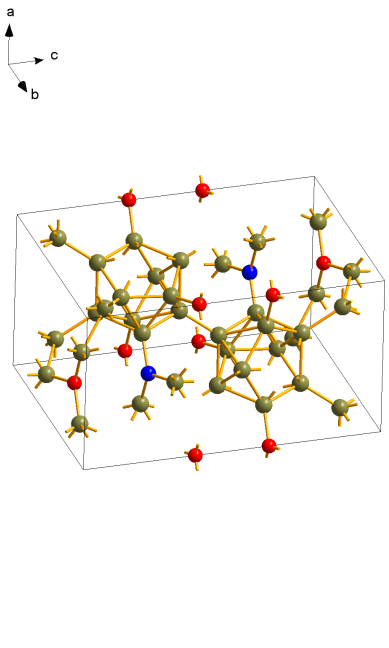


Figure 9.4: Crystal structure of B_6O with substitutional defect of 2 N at 2 O sites.